Extension of Condensate Flow Model for Aerosol Wash-down Simulation

Zur Erlangung des akademischen Grades
Doktor der Ingenieurwissenschaften
von der KIT-Fakultät für Maschinenbau
Karlsruher Institut für Technologie (KIT)

Angenommene
Dissertation
von

M.Sc. Fangnian Wang

Tag der mündlichen Prüfung: 24. November 2020

Hauptreferent: Prof. Dr.-Ing. Xu Cheng

Korreferent: Prof. Dr.-Ing. Andreas Class

Eidesstattliche Erklärung

Hiermit erkläre ich, dass ich die vorliegende Arbeit selbständig angefertigt und keine anderen als die angegebenen Quellen und Hilfsmittel benutzt sowie die wörtlich und inhaltlich übernommenen Stellen als solche kenntlich gemacht und die Satzung des Karlsruher Institutes für Technologie (KIT) zur Sicherung guter wissenschaftlicher Praxis in der jeweils gültigen Fassung beachtet habe.

Karlsruhe, 24. November 2020

Fangnian Wang

Acknowledgements

My special thanks to:

My doctor supervisor Prof. Xu Cheng, who gave me the opportunity to join his research team and supported me to do the research I loved. His guidance and comments benefited me a lot, especially for my PhD work. I really enjoyed the freedom he gave me to develop new ideas. It took time and risk, but he always gave me suitable suggestions. Without his time, insightful criticism, and expert vision in my PhD research, my dissertation would not be possible to complete. I am very grateful for all the help and encouragement he gave me.

My second supervisor Prof. Dr.-Ing. Andreas Class, who is an expert in nuclear thermal-hydraulics, especially fluid dynamics. I was very impressed by his knowledge in my research area. I greatly appreciated his comments.

My PhD project partners Dr. Holger Nowack, Ms. Sara Beck from GRS, Dr. Sanjeev Gupta from Becker Technologies, and other colleges, I appreciated them for many fruitful discussions and experimental data support.

My colleges in IATF, Mrs. Marina Djordjevic, Mrs. Isolde Stamm, Dr. Ivan Otic, Dr. Aurelian Florin Badea, Mr. Denis Klingel, Mr. Moritz Schenk, Mr. Ludwig Köckert, Mr. Hong Xu, Mr. Stelios Michaelides, Mr. Fabian Wiltschko, Mr. Zhongkai Mei, and the graduated doctors Dr. Xi Wang, Dr. Dali Yu, Dr. Florian Feuerstein, etc., I thank you all a lot for your help of my life in Germany and the contributions to my PhD work. I enjoyed the working atmosphere and beers with you.

My financial supports: my PhD project ESSA funded by the German Federal Ministry for Economic Affairs and Energy (BMWi, grant number: 1501537), and my scholarship from China Scholarship Council.

Lastly, I would like to thank my wife Huan Qin and my son Benzhen Wang, thank you for your love and support. I really enjoyed the life with you both in Karlsruhe. I would also like to thank my family in China for standing with me. I wish you good health forever!

Karlsruhe, 24. November 2020

Fangnian Wang

Abstract

Depending on the accident scenario, nuclear aerosol entering into reactor containment may consist of particles with various sizes and species. Aerosol particles deposited on inclined walls in the containment are washed down by condensate flow into lower compartments or water sumps. The transport of aerosol particles in the containment influences the distribution of dose rate and decay heat. Therefore, understanding of aerosol wash-down behavior is important for source term assessment.

The wash-down process of insoluble aerosols depends on the condensate flow and aerosol characteristics. The existing aerosol wash-down model AULA in COCOSYS code is an appropriate modelling approach of insoluble aerosol wash-down. However, the condensate flow significantly affects the aerosol wash-down efficiency. One need is the model development for describing the condensate flow pattern and its coverage on inclined walls, which can be implemented in Lumped-Parameter (LP) containment codes. Furthermore, the current aerosol wash-down model AULA should consider the wall inclination and aerosol cohesion effects in the evaluation of the aerosol erosion process.

A new modelling approach of condensate flow is developed and presented in this dissertation, which considers different condensate flow patterns. Droplet internal flow field, dynamic contact angle and the Marangoni effect are considered to evaluate the droplet velocity. A new criterion is proposed to describe the flow pattern transition from droplet to rivulet. The derived physical model as well as the proposed empirical correlation predict the condensate coverage in terms of the volume flow rate per width, contact angles, wall inclination and fluid properties. Moreover, a correction factor considering the wall inclination and aerosol cohesion is derived by the force analysis of aerosols in condensate flow, so that the critical shear stress model in AULA is improved.

A new experiment of water droplets moving on inclined paint-coated surfaces is performed to provide test data for model validation. The model of the onset of droplet motion is well assessed and validated by the new experiment. The model of the droplet velocity as well as the proposed criterion of the flow pattern transition from droplet to rivulet are also well validated. The model of condensate coverage is extensively validated by experimental data from open literature. Moreover, the extended aerosol wash-down model with the consideration of inclination and cohesion effects is validated by the THAI-AW3-LAB experiment. The aerosol wash-down model AULA coupled with the new condensate coverage model is implemented in the COCOSYS code. A good

agreement between the numerical results using the modified COCOSYS code and the measured data from the integral experiment THAI-AW3 is achieved with respect to the aerosol wash-down efficiency.

The application of the modified COCOSYS code to the ‘Generic Containment’ is carried out. The nodalisation (based on the benchmark from the SARNET2 activity) is refined and modified in order to be consistent with the aerosol wash-down model. The evolution of thermal-hydraulic parameter in the ‘Generic Containment’ during the selected severe accident scenario is presented. It is found that the temporal behavior of the aerosol wash-down efficiency is strongly affected by the condensate flow. The simulation results confirm the necessity of the modification of COCOSYS.

Kurzfassung

Abhängig vom Unfallszenario ist es möglich, dass das nukleare Aerosol, welches in den Reaktorbehälter eintritt, Partikel unterschiedlicher Größe und Art enthält. Aerosol Partikel, welche sich auf geneigten/ vertikalen Wänden im Behälter ablagern, werden von der Kondensatströmung abgewaschen und in den unteren Bereich oder in den Sumpf des Reaktorbehälters transportiert. Der Transport von Aerosol Partikeln im Reaktorbehälter beeinflusst die Verteilung der Strahlungsintensität und der Zerfallswärme. Daher ist das Verständnis des Aerosol-Abwaschverhaltens wichtig für die Bewertung des Quellterms.

Der Abwasch-Prozess unlöslicher Aerosole hängt von der Kondensatströmung und der Aerosol Charakteristik ab. Das bereits bestehende AULA Modell im COCSYS Code ist ein angemessener Modellierungsansatz für den Abwasch-Prozess unlöslicher Aerosole. Allerdings hat die Kondensatströmung einen signifikanten Einfluss auf die Effizienz des Abwasch-Prozesses. Es ist notwendig, jeweils ein Modell zur Beschreibung der Kondensatströmung und für die Benetzung der schrägen Wände zu entwickeln, welche anschließend in COCOSYS implementiert werden können. Weiterhin sollte das aktuelle Aerosol Abwasch-Modell AULA die Neigung der Wand sowie Kohäsionseffekte für die Bewertung des Aerosol Erosionsprozesses berücksichtigen.

In dieser Dissertation wird ein neuer Modellansatz zur Beschreibung der Kondensatströmung vorgestellt, in welchem verschieden Formen der Kondensatströmung berücksichtig werden. Zur Bestimmung der Tropfengeschwindigkeit werden das innere Strömungsfeld im Tropfen, der dynamische Kontaktwinkel, sowie der Marangoni Effekt berücksichtigt. Um den Übergang der Strömungsmuster von Tropfenströmungen zu Rinnsalströmungen zu beschreiben wurde ein neues Kriterium eingeführt. Sowohl das abgeleitete physikalische Modell, als auch die vorgestellte empirische Korrelation, berechnen die Benetzung bezüglich Volumenstrom pro Wandbreite, Kontaktwinkel, Wandneigung und der Fluideigenschaften. Außerdem wird ein Korrekturfaktor für die Wandneigung und die Kohäsion der Partikel aus einer Analyse der Kräfte der Aerosole in einer Kondensatströmung hergeleitet, wodurch das sogenannte kritische Schubspannungsmodell in AULA verbessert wird.

Um Testdaten für die Modellvalidierung zu generieren, wird ein neues Experiment mit Wassertropfen auf einer geneigten lackierten Wand durchgeführt. Das Modell für den Beginn der Tropfenbewegung wird mit Hilfe des neuen Experiments bewertet und validiert. Das Modell für die Tropfengeschwindigkeit sowie das Kriterium für den Übergang von Tropfenströmung zu Rinnsalströmung werden ebenfalls anhand dieses

Experiments validiert. Das Modell für die Benetzung wird ausführlich anhand von frei zugänglicher Literatur validiert. Außerdem wird das erweiterte Aerosol Abwasch-Modell unter Berücksichtigung der Wandneigung und der Kohäsionseffekte anhand des THAI-AW3-LAB Experiments validiert. Das Aerosol Abwasch Modell AULA wird gekoppelt mit dem neuen Modell für die Benetzung im COCOSYS Code implementiert. Der Modifizierte COCOSYS Code wird mit dem THAI-AW3 Experiment verglichen, wobei eine gute Übereinstimmung der numerisch berechneten und der experimentell gemessenen Abwascheffizienz erreicht wird.

Der modifizierte COCOSYS Code wird im sogenannten „Generic Containment“ angewandt. Die Diskreditierung (basierend auf dem SARNET2 Benchmark) wird verfeinert und modifiziert, um Konsistenz mit dem Aerosol Abwasch Modell zu erreichen. Für das ausgewählte schwere Unfallszenario wird die Entwicklung der Thermo-hydraulischen Parameter im „Generic Containment“ präsentiert. Dabei zeigt sich, dass das zeitliche Verhalten der Abwascheffizienz stark von der Kondensatströmung abhängt. Die Ergebnisse der Simulation untermauern die Notwendigkeit den COCOYSY Code zu modifizieren.

Contents

List of Figures

List of Tables

Nomenclature

Symbol	Explanation	Unit
General		
A	contact (wet) area of droplet/rivulet	m^2
A_1/A_2	contact (wet) area of droplet part 1 and 2	m^2
A_H	Hamaker constant, $A_H \cong 10^{-20}$	J
A_w	wall area	m^2
a	initial rivulet half width	m
Bo	Bond number	-
Bo_c	critical Bond number where droplet start moving	-
Bo_t	Bond number where transition happens	-
Ca	Capillary number	-
$C_{i,c}$	correction factor of inclination and cohesion	-
$c_1/c_2/c_3/c_4$	functions of equilibrium contact angle	-
c_{ae}	deposited aerosols load on surface	kg/m^2
$c_{ae,0}$	initial deposited aerosols load on surface	kg/m^2
c_δ	prefactor of empirical rivulet thickness correlation	-
d_h	hydraulic diameter of interface between droplet part 1 and 2	m
d_p	particle diameter	m
d_t	critical droplet diameter where transition happens	m
F_C	cohesive force	N
F_D	drag force of the overlying flow	N
F_F	friction force of the particle in the first layer	N
F_g	gravitational force of droplet	N
$F_{g,1}/F_{g,2}$	gravitational force of droplet part 1 and 2	N
$F_{i,21}/F_{i,12}$	action and reaction forces on interface of droplet	N

F_L	lift force of the overlying flow	N
F_M	equivalent Marangoni force acting on droplet	N
$F_{M,1}/F_{M,2}$	equivalent Marangoni force acting on droplet part 1 and 2	N
F_W	buoyant weight of particle	N
F_σ	surface tension force of droplet	N
$F_{\sigma,1}/F_{\sigma,2}$	surface tension force of droplet part 1 and 2	N
$F_{\sigma,A}/F_{\sigma,R}$	advancing/receding component of surface tension force of droplet	N
F_τ	viscous forces of droplet bulk part	N
$F_{\tau,1}/F_{\tau,2}$	viscous forces of droplet bulk part 1 and 2	N
$F_{\tau,w}$	viscous forces of droplet wedge part	N
g	gravity acceleration, 9.8	m/s^2
g_{iv}/g_v	functions of contact angle	-
h	moving distance (on structure) of droplet/rivulet	m
h_t	critical height where transition happens	m
Δh_{fg}	specific latent heat of vapor condensation	J/kg
Ka	Kapitza number	-
$K(n)$	compaction function of particle	-
k	factor of droplet surface tension force	-
$k_{D,1}/k_{D,2}$	factors of drag force	-
k_e	erosion rate	1/s
$k_{e,0}$	erosion constant	1/s
k_L	factor of lift force	-
k_W	factor of buoyant weight force	-
L_a	apparent (macroscopic) length of droplet	m
L_s	microscopic cut-off length scale of droplet	m
m_{ae}	remaining deposited aerosol mass on water-covered area	kg
n	porosity of particles	-
n_d	droplet initiation density	1/(m^2·s)
n_{min}/n_{max}	minimum/maximum porosity of particles	-
P	droplet contact area perimeter	m
p	Pressure	Bar
q	condensation heat flux	W/m^2

R^*	dimensionless auxiliary parameter	-
Re	Reynolds number	-
Re^*	Reynolds number of particle	-
r	radius of droplet	m
r_1/r_2	radius of droplet part 1 and 2	m
r_t	radius of droplet where transition happens	m
s	density ratio of particle to water	-
T	temperature	℃
t	time	s
u	droplet/rivulet/film (condensate) velocity	m/s
$\bar{u}$	average droplet/rivulet (condensate) velocity	m/s
$\bar{u}_r$	average rivulet velocity	m/s
u^*	shear velocity of condensate flow	m/s
u_c^*	critical shear velocity of particle	m/s
V	droplet/rivulet volume	m^3
V_1/V_2	volume of droplet part 1 and 2	m^3
V_0	droplet onset of motion volume	m^3
ΔV_{cond}	condensation during movement	m^3
V_t	critical volume where transition happens	m^3
$\dot{V}$	volume flow rate per width	$m^3/(m\cdot s)$
$\dot{V}_r$	rivulet volume flow rate per width	$m^3/(m\cdot s)$
We	Weber number	-
x	horizontal direction to the wall (normal to yz-plane)	-
y	normal (perpendicular) direction to the wall	-
Δy	droplet height in y- direction	m
z	droplet/rivulet moving direction	-
Greek symbols		
α	inclination angle	°
α_c	characteristic internal friction angle (critical inclination angle)	°
δ	droplet/rivulet/film thickness	m
$\bar{\delta}$	average droplet/rivulet (condensate) thickness	m

$\bar{\delta}_r$	average rivulet thickness	m
ε	condensate coverage	-
ε_d	droplet coverage in coexisting phase	-
$\varepsilon_{d,t}$	droplet coverage where transition happens	-
ε_r	rivulet coverage in coexisting phase	-
θ_e	equilibrium contact angle	°
$\theta_{d,A}/\theta_{d,R}$	dynamic advancing and receding contact angle	°
θ_s/θ_d	static/dynamic contact angle	°
$\theta_{s,A}/\theta_{s,R}$	static advancing and receding contact angle	°
θ^*	intermediate variable in the Cox, 1998 model	°
μ	dynamic viscosity	Pa·s
μ_c	Coulomb friction coefficient	-
ν	kinematic viscosity	m^2/s
π	dimensionless number, π_1-π_5	-
ρ	water density	kg/m^3
ρ_p	particle density	kg/m^3
σ_{LG}	surface tension between water and air	N/m
$\Delta\sigma_{LG}$	surface tension change caused by temperature gradient	N/m
ϕ	thickness in the arc part of rivulet	m
τ_c	critical shear stress	Pa
τ_c^*	dimensionless critical shear stress	-
$\tau_{c,o}^*$	dimensionless critical shear stress of horizontal bed	-

Abbreviations

ASTEC	Accident Source Term Evaluation Code
AULA	German: “Abwaschen UnLöslicher Aerosole”
AW	Aerosol Wash-down
CFD	Computational Fluid Dynamics
CONRAG	CONdensate coveRAGe model
COCOSYS	COntainment COde SYStem
DBA	Design Basis Accident
DRISE	Drop and Rivulet on Inclined Surface Experiment
ECCS	Emergency Core Cooling Systems

FP	Fission Products
GRS	Gesellschaft für Anlagen- und Reaktorsicherheit
IRSN	Institute for Radiological Protection and Nuclear Safety
IOZ	InOrganic Zinc-rich decontamination paint
LP	Lumped-Parameter
MCCI	Molten Core-Concrete Interactions
MGA	Moving-Grid method
MTE	Minimum Total Energy
NPP	Nuclear Power Plant
NRC	Nuclear Regulatory Commission
PSI	Paul Scherrer Institute
PWR	Pressurized Water Reactor
RPV	Reactor Pressure Vessel
SA	Severe Accident
SARNET	Severe Accident Research NETwork of excellence
SB-LOCA	Small Break Loss-Of-Coolant Accident
SG	Steam Generator
SNL	Sandia National Laboratories
THAI	Experiment of Thermal-hydraulics, Hydrogen, Aerosols, Iodine
WABREC	WAter Behavior in REctangle Channel
WAR	Wall-Gas radiative heat transfer
WWR	Wall-gas-Wall radiative heat transfer

1 INTRODUCTION

1.1 **Motivation**

Nuclear safety is of great importance in Nuclear Power Plants (NPPs), which is the achievement of prevention of accidents or mitigation of accident consequences, resulting in protection of the environment from radiation hazards (IAEA, 2006). In case of an accident in Pressurized Water Reactor (PWR), large amounts of steam, non-condensable gas, and fission products could be generated and released into the containment. The integrity of the containment could be challenged. The containment is the ultimate barrier against the release of fission products to the environment.

During Severe Accidents (SA) of PWR, fission products are released due to core degradation inside Reactor Pressure Vessel (RPV) and Molten Core-Concrete Interactions (MCCI) outside RPV. The aerosols in reactor coolant system and containment is the result of the processes of nuclear aerosol transport, deposition, resuspension, wash-down, etc. The prediction of the nuclear aerosol behavior associated with severe accidents in NPP is an important aspect of reactor safety evaluation (Allelein et al., 2009). The nature and behavior of nuclear aerosols can potentially influence both the course and the consequences of reactor accidents. For example, nuclear aerosols can affect the performance of engineered safety systems (e.g. air cleaning systems), the damages of local components (like electronic devices, seals, etc.), and the radioactive source term leaked to the environment.

Nuclear aerosols are released into the containment with a large amount of steam and non-condensable gases during severe accidents. Together with the steam condensation, aerosols are transferred on cold walls (Weber et al., 2015).

The condensate flow washes down the aerosols, and transports them into lower compartments or water sumps. This aerosol wash-down process influences the distribution of the fission products. The schematic concept of aerosol wash-down process is seen in Fig. 1-1.

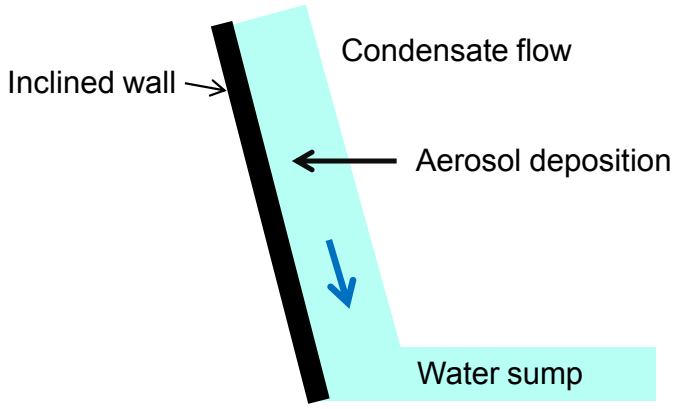

Fig. 1-1 Schematic of aerosol wash-down process

The aerosol wash-down is defined that the deposited aerosols on inclined walls are washed down by the condensate flow. Aerosol deposition on containment walls is due to the gravitational settling, thermal diffusion, condensation, etc., which determines the aerosol load on the surface. The aerosol wash-down takes place after the aerosol deposition, if the condensate flow fulfills a certain condition that shear velocity of condensate flow exceeds the critical one. The aerosol properties and shear velocity of condensate flow determine the aerosol erosion rate. The condensate coverage (water-covered area fraction) on inclined surfaces also quantifies the mass of aerosol wash-down.

Therefore, the aerosol wash-down process interacts with the containment thermal-hydraulics and the aerosol transport process. Under different severe accident scenarios, there are different trends of containment thermal-hydraulics, aerosol properties, aerosol injections, etc. The containment thermal-hydraulics, e.g. condensate flow rate, strongly influence the condensate coverage and the aerosol deposition. The aerosol injection is affected by core damage process and MCCI, which is the source term of the aerosol deposition and the aerosol wash-down on inclined surfaces.

Reliable simulation tools are required in order to describe containment thermal-hydraulic processes, fission product behaviors, and accident mitigation measures, etc. In the Containment Code SYStem COCOSYS developed by Gesellschaft für Anlagen- und Reaktorsicherheit (GRS), the thermal-hydraulics and the aerosol behavior are currently modelled (Klein-Heßling et al., 2015). The code consists of three modules covering thermal-hydraulics, fission products behavior and molten core-concrete interactions. The modules of thermal-hydraulics and fission products behavior are involved in the current work. For instance, the wash-down model for insoluble aerosols **AULA** (German: "**A**bwaschen **u**n**l**öslicher **A**erosole") in COCOSYS simulates the erosion of insoluble aerosols by condensate flow. The erosion takes place if the

flow shear velocity at the wall exceeds the critical threshold.

However, condensate coverage is an important parameter that indicates how much area is wetted, where the aerosol wash-down takes place. The condensate coverage is considered currently as rivulets with a user-defined value in COCOSYS. Investigation indicates the condensate coverage depends on the water flow rate and fluid properties (Weber et al., 2015).

In addition, inclined walls usually exist in nuclear containment. Experiments (e.g. THAI-AW3-LAB) reveal the cohesive force of nuclear aerosols cannot be neglected for the aerosol wash-down on inclined surfaces (Laufenberg et al., 2014a,b). In AULA, the critical shear stress is calculated based on an empirical correlation without the consideration of wall inclination and aerosol cohesion, so that it is necessary to modify the existing correlation.

1.2 **Objectives**

The general aim of the research is to develop new condensate flow models to describe the condensate behavior on inclined/vertical walls in containment. The investigated models will be validated by experimental data and implemented in COCOSYS. Combining with the thermal-hydraulic and other aerosol physical models in COCOSYS, the work is able to improve the simulation capacity of aerosol wash-down process in nuclear containment. The particular objectives are given as follows:

- **Knowledge updating:** Literature review is to update the existing knowledge in the field of aerosol wash-down and to prepare the experimental data for model validation. Attentions are paid to the descriptions of the separate physical effects. Using the existing approaches to model the individual separate phenomena, the basic understanding of the aerosol wash-down process is to be improved.
- **Model development:** new condensate flow models (including the condensate coverage) on inclined walls take into account the flow patterns, i.e. droplet, rivulet and film. The Marangoni effect, the flow field inside the droplet and the dynamic contact angle are considered to evaluate the droplet velocity. A new criterion is proposed for the transition from droplet to rivulet. The critical shear stress is considered with the effects of wall inclination and aerosol cohesion. Those proposed models extend the simulation capability of the existing aerosol wash-down model AULA.
- **Model validation:** New models are validated against the experimental data, which include the new experimental data, the data from open literature, and the data from the laboratory scale experiment THAI-AW3-LAB and from the integral experiment THAI-AW3.

- **Application to ‘Generic Containment’:** The newly developed models are converted into a program module, which is implemented in the LP containment code COCOSYS. The modified COCOSYS is applied to a ‘Generic Containment’ for investigating the aerosol wash-down behavior.

The dissertation consists of six chapters. The first chapter briefly introduces the motivation and objectives. The second chapter presents the literature review. The third chapter introduces the model development in detail. In the fourth chapter, new models are validated against experimental data. In the fifth chapter, the modified COCOSYS is applied to a ‘Generic Containment’ for evaluating the aerosol wash-down process. The sixth chapter draws the conclusions and gives the outlook.

2 LITERATURE REVIEW

Under severe accidents, nuclear aerosols are released into containment together with the steam condensation on cold surfaces. The deposited aerosols on inclined walls can be washed down by the condensate flow if the flow shear stress exceeds the threshold. This aerosol wash-down process has a crucial importance for the fission products distribution in nuclear containment. The aerosol wash-down process is dominated by the particle erosion and transport in condensate flows, which is however strongly affected by the flow characteristics, e.g. the flow shear stress determines the aerosol erosion rate and the condensate coverage on surface quantifies the aerosol wash-down efficiency.

Therefore, in this chapter, the state-of-the-art on nuclear aerosol wash-down and the related condensate flow are presented, respectively. With respect to the aerosol wash-down process, we will look at the experimental studies, e.g. the THAI aerosol wash-down experiments (Gupta and Langer, 2009; Gupta et al., 2012; Freitag et al., 2016) and PHEBUS fission products (FP) experiments (Hanniet-Girault, 1999; Jacquemain, 2000; Sangiorgi, 2015). Then we will introduce the aerosol behavior model in the well-known LP containment codes, and furthermore the existing aerosol wash-down model that have been implemented in containment codes.

The aerosol wash-down model involves the consideration of the condensate flow behavior. Various condensate flow patterns, such as moving droplet, rivulet, and fully covered film, will be reviewed. Based on the literature review, open questions in modelling aerosol wash-down process will be given.

2.1 Aerosol wash-down

A few studies of aerosol wash-down on inclined walls in the nuclear containment safety area are presented in the open literature. Aerosol wash-down phenomenon is so far mainly investigated experimentally in the THAI test facility by Becker Technologies (Gupta and Langer, 2009; Gupta et al., 2012; Freitag et al., 2016) and in the frame of the PHEBUS FP Program conducted by IRSN (Hanniet-Girault, 1999; Jacquemain, 2000; Sangiorgi, 2015). The PHEBUS FP experiments investigated the aerosol behavior in containment under severe accident conditions, including the aerosol generation, transport and distribution in containment. A series of aerosol wash-down experiments was involved in the THAI project. The aerosol behavior and its coupling with the containment thermal-hydraulics can be modeled in some safety and containment analysis codes, such as MELCOR (Gauntt et al., 2005), ASTEC (Van Dorsselaere et al., 2009), CONTAIN (Williams et al., 1997) and COCOSYS (Klein-Heßling et al., 2015). The aerosol wash-down experiments and the related model in the containment codes are introduced and consequently the conclusions are presented in the following sections.

2.1.1 Experimental studies

There are only a few aerosol wash-down experimental investigations. The aerosol wash-down experiment series in the THAI test facility were directly concentrated on the wash-down process including the technical scale tests and laboratory scale tests, while the PHEBUS FP experiments studied the aerosol behavior in containment integrally. All these experiments are presented case by case as follows.

- **THAI aerosol wash-down experiments**

The technical scale test facility THAI (Thermal-hydraulics, Hydrogen, Aerosols, Iodine) has been operated by Becker Technologies at Eschborn, Germany, in close cooperation with AREVA and GRS, in order to provide experimental database for the model development and validation of containment codes. The THAI test facility with standard internals is shown in Fig. 2-1 (Gupta and Langer, 2009). Up to now, at least 6 types of experiments have been performed for evaluating the phenomena in containment, such as helium mixing and distribution, hydrogen deflagration, hydrogen recombiner, passive autocatalytic recombiner poisoning, aerosol wash-down, iodine behavior, etc. The THAI experiments filled the knowledge gaps by delivering data for the evaluation of the thermal-hydraulic performance and fission product behavior, thereby supporting the validation of containment codes.

A series of **A**erosol **W**ash-down experiments (AW) including THAI-AW, AW2,

and AW3 were carried out in the THAI test facility in the years 2009-2016. These integral aerosol wash-down experiments have been performed to investigate the wash-down behavior of insoluble/soluble aerosols deposited on surfaces under pre-defined thermal-hydraulic conditions (Gupta and Langer, 2009; Gupta et al., 2012; Freitag et al., 2016).

The thermal-hydraulic conditions were established in such a way that the aerosol wash-down occurred only by the condensate flow over the vessel walls. The condensate drained out from the plates was analyzed separately for determining the aerosol concentration. Tests were conducted with single component aerosols of different solubility (CsI and Ag), and aerosol mixture (CsI and SnO_2). The following section provides an overview of the THAI aerosol wash-down experiments.

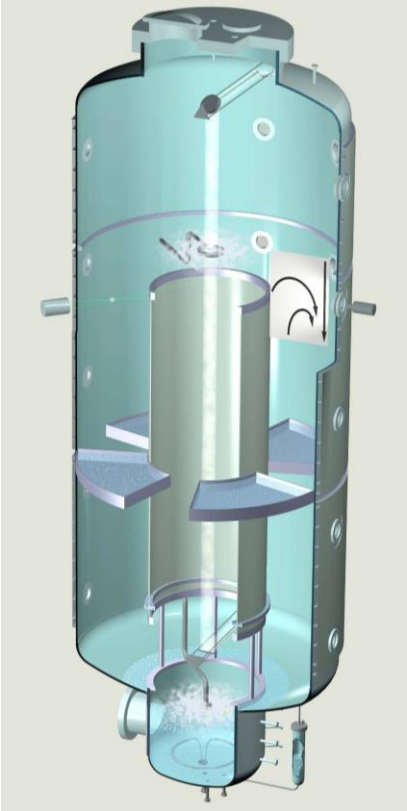

Fig. 2-1 THAI facility with standard internals (inner cylinder and four trays) For aerosol wash-down experiments, the standard internals were removed and quasi-horizontal plates and a small puddle were set up instead (Gupta and Langer, 2009).

a) THAI-AW

As a first step, THAI-AW addressed the main phenomenon related to the wash-down process of soluble aerosol CsI. The test phases were arranged in a way so that the steam condensed on the vertical vessel walls and further contributed to the wash-down of the aerosols deposited on the surfaces. The accumulated condensate was continuously drained into the independent gutters. The general

knowledge of aerosol wash-down behavior over quasi-horizontal surfaces and small puddles in containment was achieved. The THAI-AW experiment concluded that the time range of the aerosol wash-down was from minutes to hours and the completeness of the aerosol wash-down was dependent on the condensate flow, the aerosol surface load and the surface characteristics. Moreover, test results indicated that wash-down from the quasi-horizontal surfaces was complete, but the aerosol concentration in water drained from the puddle decreased much slower and the washing period took one day long. In other words, the puddle water acted as an intermediate storage of dissolved CsI, which led to a considerable delay in the aerosol transport (Gupta and Langer, 2009).

b) THAI-AW2

THAI-AW2 has been performed to investigate the wash-down behavior of soluble CsI and insoluble SnO_2 aerosol mixture. The results on wash-down behavior of soluble CsI aerosol was in agreement with those from THAI-AW and concluded that the wash-down efficiencies of the soluble and insoluble aerosols were independent from each other. However, the wash-down of insoluble aerosols remained far from being complete. Soluble aerosol was injected by two nozzles from the top of the vessel into the air atmosphere while insoluble aerosol produced by a brushing device was released at the same time also from the top of the vessel together with a carrier gas (Gupta et al., 2012).

c) THAI-AW3

THAI-AW3 has been conducted in two parts (insoluble aerosol Ag wash-down and the interaction between Ag and iodine chemical behavior in water sump). The insoluble aerosol Ag wash-down on vertical walls, on quasi-horizontal surfaces and a small puddle by the condensate water flow has been investigated. Test results indicated that about 50% of the total washed-down quantity of silver at all measurement locations (quasi-horizontal/vertical/puddle) has been collected in less than 15 min and thereafter the removal of the Ag particles occurred at a decreasing rate. Furthermore, the erosion process of the silver particles by condensate played a vital role. Condensate flow patterns, such as rivulets observed with long-lasting stability on surface in the presence of insoluble aerosols, were found to have an influence on the aerosol wash-down behavior. The recovered aerosol mass indicated very low wash-down efficiency of deposited Ag aerosol as well as very low condensate coverage. The Ag aerosol wash-down efficiency was 16% for the vertical wall section, 9.5% for the combined wall/horizontal plate section and 10.2% for the combined wall/puddle (Freitag et al., 2016).

d) THAI-AW4

THAI-AW4 presented the reduction of airborne aerosol concentration in THAI facility by a spray system that was typical for reactor containments. The internals of trays in the vessel had been removed to form free unobstructed

environment. Steam condensed and ran down the vertical vessel walls. The evolution of the aerosol concentration and the containment thermal-hydraulic parameters have been investigated. The test results revealed that the reduction of the aerosol concentration was more pronounced for the first spray operation than for the second one. The washout of larger particles was stronger than that of smaller ones. The derived data were of good quality and contributed to the validation and to the refinement of the related analytical models, e.g. the droplet size distribution within the spray model instead of an average droplet diameter in LP containment codes (Freitag et al., 2018).

e) THAI-AW3-LAB

THAI-AW3-LAB experiment was also one of the aerosol wash-down experiments conducted by Becker Technologies (Laufenberg et al., 2014a,b; Gupta et al., 2015). It was a laboratory scale test with the purpose to measure the removal of insoluble silver aerosol deposited on inclined surfaces by water flow.

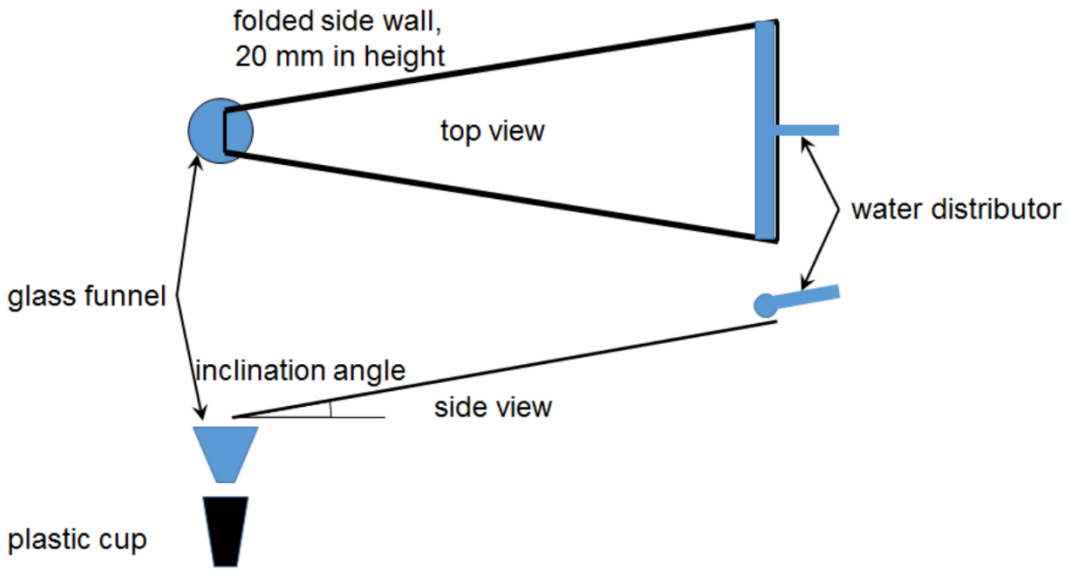

Fig. 2-2 THAI-AW3-LAB test sketch of water distribution and sampling system (Laufenberg et al., 2014a,b)

The experimental setup was used to perform a series of wash-down tests, in which surface inclination, water flow rate, aerosol load as well as particle size were varied. The test sketch of the water distribution and the sampling system are shown in Fig. 2-2. Two different surfaces types (stainless steel and decontamination paint) of interest were representative for containment structures. The test plates were made of stainless steel and some of them were coated by decontamination paint. A total of 15 tests were conducted. Each test consisted of an initial dry aerosol-loading phase and the later wash-down phase. The experimental data exhibited a clear trend of a fast aerosol wash-down in

the beginning, which was followed by a slow removal process. Some tests (such as test 3, test 4, and test 12) can also be used to validate the rivulet behavior and its coverage. The main processes, which were found to have an influence on the observed aerosol wash-down behavior, included rivulet flow pattern. Another major outcome of these tests was the observation of long-lasting stability of rivulets on the surface.

Table 2-1 Summary of THAI aerosol wash-down experiments

Experiment	Type	Aerosol	Results of interest	Validation
THAI-AW	Integral	Soluble, CsI	Completeness of wash-down depends on rivulet coverage	-
THAI-AW2	Integral	Mixture, CsI & SnO_2	Wash-down efficiencies of soluble/ insoluble aerosols are independent	-
THAI-AW3	Integral	Insoluble, Ag	Wash-down of insoluble aerosols coupling with rivulet coverage	Yes
THAI-AW4	Integral	Soluble, CsI	Reduction of aerosol concentration by containment spray	-
THAI-AW3-LAB	laboratory	Insoluble, Ag	Wash-down of insoluble aerosols and rivulet behavior	Yes

Table 2-1 summaries the information of interest of the THAI aerosol wash-down experiments. In conclusion, the THAI-AW3 and THAI-AW3-LAB investigated the wash-down behavior of insoluble aerosols coupling with rivulet coverage, which can validate the aerosol wash-down model that we focus on.

- **PHEBUS fission products experiments**

The PHEBUS FP international research programme was conducted by IRSN in partnership with several international organizations between 1988 and 2010. Its purpose was to improve the understanding of the phenomena occurring during a core meltdown accident in a light water reactor and to validate the computational software used to evaluate these phenomena (Von der Hardt and Tattegrain, 1992). Five PHEBUS FP tests were conducted in the research programme. The schematic view of the PHEBUS FP facility is shown in Fig. 2-3. The first series of three tests (FPT-0, FPT-1 and FPT-2) made it possible to study the influence of the fuel degradation, the release and transport of fission products, and the behavior of the fission products in the reactor containment (Hanniet-Girault, 1999; Jacquemain, 2000; Sangiorgi, 2015). The last two

series (FPT-3 and FPT-4) involving the fission products released from debris bed and the influence of boron carbide rod on fuel degradation, are not the topic we discussed in this dissertation.

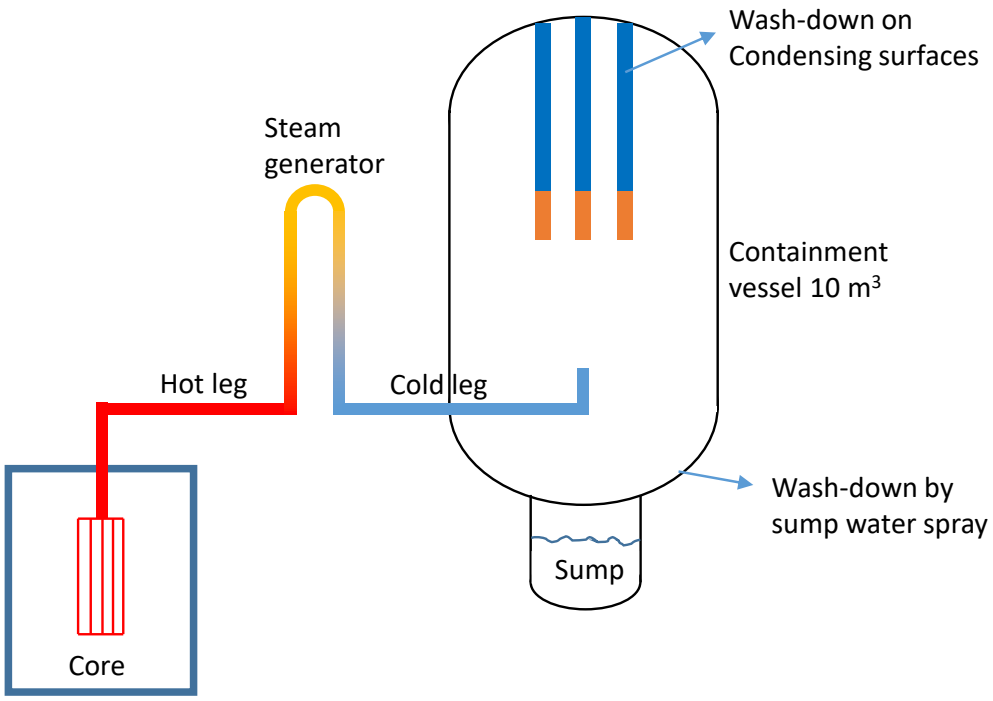

Fig. 2-3 Schematic view of the PHEBUS FP facility

This first test **FPT-0** was conducted under conditions of low primary circuit pressure (0.2 MPa) and an atmosphere rich in steam. The main objective was to study the degradation of non-irradiated fuel and the behavior of the fission products, in the presence of a control rod made of silver, indium and cadmium alloy. **FPT-1** test took place under the same conditions as the test FPT-0, but the degradation of fuel irradiated at 23 GWd/tU (a level equivalent to two cycles of irradiation in PWR). **FPT-2** test supplemented the first two tests (FPT-0 and FPT-1) by studying somewhat reducing (hydrogen-rich) conditions, which the flow rate of steam injected at the test system inlet was much lower.

In these three tests, the fission products released from the bundle were transported by the steam flow, through the experimental line to the containment vessel. A so-called condenser consisting of 3 rods inside the containment vessel was installed, as shown in Fig. 2-3, in order to study the aerosol behavior related to the condensation on surfaces, where a prescribed temperature history was imposed to reach the desired condensation rate. This part of the experimental data can be used to assess the aerosol deposition onto condensing surfaces. Liquid collected sequentially was used to quantify the amount of aerosols wash-down by the condensate flow, which brought aerosols to the sump through the diffusiophoresis deposition mechanism on the condensing surfaces. There was another wash-down process during the experiments, where aerosols on the containment elliptic bottom were washed

down by a sump water spray. The spray water collecting the deposited aerosol, drained into the water sump, in order to initiate the radiolysis process and investigate the aerosol behavior in the water sump, which was, however, not the topic of wash-down by condensate flow we discussed in this dissertation.

In summary, aerosol wash-down by the flow on the condensing surface in PHEBUS FPT-0, FPT-1 and FPT-2 tests was carried out to investigate the diffusiophoresis deposition mechanism. However, the aerosol concentration in condensate or in containment integrated several aerosol behavior mechanisms, not only the wash-down process but also the deposition. The condensate coverage on the surface was not measured. Therefore, the PHEBUS experimental data can be used to validate the integral effect of aerosol behavior in containment but cannot be used to validate the aerosol wash-down model directly.

2.1.2 Model in containment codes

The most commonly used LP containment codes (including integral codes here), like MELCOR, ASTEC, CONTAIN, COCOSYS, etc., systematically analyze the thermal-hydraulics and aerosol behaviors of NPP's containment, which are also applied for the parametric analysis of severe accident scenarios. This section addresses the modelling capabilities of these well-known containment codes used to predict aerosol behavior in NPP's containment and goes further in detail if the one includes aerosol wash-down model.

- **MELCOR**

MELCOR is a systems-level model for the accident prediction in light water nuclear power reactors and other nuclear facilities (Gauntt et al., 2005; Allelein et al., 2009). It was developed initially by the United States Nuclear Regulatory Commission (NRC) and now by Sandia National Laboratories (SNL) as an analysis tool to support the quantitative estimation of risk to the public associated with nuclear facilities and especially nuclear power plants. The treatment of aerosols in MELCOR includes the release of aerosols from heated fuel and core debris, the transport and deposition of aerosols in the reactor coolant system and the reactor containment, and the effects of engineered safety systems on the amount of aerosols that can be released from containment. Each of these aspects of the code is discussed in the following.

MELCOR considers the aerosol release both inside and outside the reactor vessel. The aerosol release in-vessel when the fuel is overheated can be calculated using related models that have empirical relationships to experiments of fission product release from fuel heated. Ex-vessel release of aerosols when reactor fuel has been expelled from the reactor coolant system into the containment is also done with models developed based on experimental data, which considers fission product release by vaporization into

bubbles, bursting of bubbles at the surface of molten core debris, etc.

The modeling of aerosol dynamics, e.g. the agglomeration and deposition of aerosol particles, are done in MELCOR by using the MAEROS model. The MAEROS model was developed originally by Gelbard (1982), which is one of the earliest models to use the sectional method for the prediction of aerosol behavior in a control volume (nuclear containment usually subdivided into control volumes in containment codes). MAEROS is both multi-sectional and multi-component. Each aerosol size class considered in MAEROS can have a different chemical composition. Deposition mechanisms considered in MAEROS are gravitational settling, diffusion, thermophoresis, and diffusiophoresis.

MELCOR considers the effects of engineered safety features on aerosols. The modeled specific features include decontamination by steam suppression pool (pool scrubbing), containment spray, ice bed, filter, and fan cooler. For instance, decontamination by steam suppression pools is done with the SPARC90 model developed by NRC (Owczarski and Burk, 1991). This model calculates the removal of aerosols from gas sparging in suppression pools.

As a fully integrated code, MELCOR is developed to simulate the progression of postulated accidents in NPPs. The current uses of MELCOR include estimation of aerosols release in-vessel and ex-vessel, the transport and deposition, and the effects of engineered safety systems. The implemented models in MELCOR to predict aerosol behavior in the containment do not include the aerosol wash-down on the inclined surface by condensate flow. The capability of MELCOR to model the aerosol wash-down behavior is not done so far.

- **ASTEC**

The integral code ASTEC (Accident Source Term Evaluation Code) (Van Dorsselaere et al., 2009, Chatelard and Reinke, 2009) is developed by IRSN (the Institute for Radiological Protection and Nuclear Safety) in close cooperation with GRS. ASTEC simulates the complete scenario of severe accidents in a light water reactor and estimates the possible fission products released from the reactor. ASTEC models the transport of fission product aerosols in the reactor cooling system through the gas flow to the reactor containment. Using different families of species and states, the mechanistic and semi-empirical approaches model the main aerosol transport phenomena. The effects of engineered safety systems on aerosols, e.g., the steam suppression pool, containment spray, etc., are also modeled in different modules individually.

For the aerosol release, at the beginning, ASTEC computes the thermal-hydraulics in primary and secondary circuits as well as in the reactor vessel. ASTEC treats the phenomena of the core degradation and then the molten core-concrete interactions. ASTEC allows describing the release from fuel, followed by the release from debris beds if any. The aerosol release modelling

is based on a semi-empirical approach and the physical phenomena taken into account are the main limiting phenomena.

For aerosol transport and deposition in control volume, these aerosol dynamics are calculated by the model MAEROS as well as in MELCOR code. The models in ASTEC describe the phenomena such as volume condensation and growth of insoluble and soluble aerosol particles, the behavior of chemically different aerosol components, etc. The models are included to calculate the decay heat of gaseous and particulate fission products and their transport/deposition by the different hosts like water or walls in containment. Furthermore, ASTEC considers the remobilization of the deposits, e.g. the mechanical resuspension including the dry (hydrogen deflagration) and wet resuspension (sump boiling).

For the effects of engineered safety systems on aerosols, several systems are modelled. For example, the aerosol retention through water pools is simulated with the pool-scrubbing model SPARC-B. The behavior and effect of the spray system on aerosol retention is thoroughly modelled.

- **CONTAIN**

Containment code CONTAIN was developed at Sandia National Laboratories under the sponsorship of the United States NRC for analyzing containment phenomena under severe accident and design basis accident conditions. CONTAIN is a modular and integrated analysis tool used for predicting physical conditions, chemical compositions, and distributions of aerosols inside a containment following the release of aerosols in a light water reactor (Williams et al., 1997). Interactions among thermal-hydraulic phenomena and aerosol behavior are taken into account. The code includes atmospheric models for steam/air thermodynamics, condensation/evaporation on structures and aerosols, aerosol behavior, and so on. It also includes models for reactor cavity phenomena such as MCCI and water pool boiling. The aerosol decontamination effects of engineered safety features are also modeled, including pool scrubbing, containment spray, ice condensers, and fan cooler.

CONTAIN is provided with two aerosol injections into the containment: the primary circuit and the MCCI. The former is given through the code input deck, whereas the latter is a result of an internal module of CONTAIN as the same as in MELCOR.

The basic aerosol dynamic modeling in CONTAIN comes from the MAEROS code together with some enhancements. The major generic features are size distribution can be dispersed by 10-20 classes, chemical composition can be detailed by using 8 material components, steam condensation onto particles is tightly coupled with thermal-hydraulics. It is available in CONTAIN to model condensation of vapor/evaporation of water onto/from aerosols.

- **COCOSYS**

COCOSYS code is a part of the GRS code system AC^2, designed for simulating

relevant phenomena, processes, and conditions expected during design basis and severe accidents inside nuclear reactor containment (Klein-Heßling et al., 2015). One key aspect of COCOSYS is the extensive consideration of interactions between various phenomena, such as thermal-hydraulics, hydrogen combustion, aerosol/fission product behavior, and molten core-concrete interactions. The models implemented in COCOSYS are based on a lumped-parameter concept as well as in MELCOR, ASTEC, and CONTAIN. The compartments or rooms of a power plant, a test facility, or any other building are subdivided into control volumes to be analyzed, which are connected by so-called junctions. The temperatures and masses of the specified components (e.g., gases, steam, and water) define the thermodynamic state of a control volume. The mass and energy balances are solved while the momentum balance of the gas flow inside control volumes is not considered. The momentum equations are only for 'junctions' but not associated with control volumes (zones). For walls (structures), an one-dimensional heat conduction equation is solved (Klein-Heßling et al., 2015).

For the purpose of completing sequence calculations and obtaining the aerosol release from fuel, COCOSYS can be coupled to the primary circuit code ATHLET-CD that simulates the core degradation. During the ex-vessel phase, COCOSYS has its own module to model the MCCI.

AFP (Aerosol Fission Products) is one of the main modules in COCOSYS, which describes the dynamic behavior of multi-component poly-disperse aerosols in a multi-compartment containment, which contains the same models as in MAEROS. The aerosol may be composed of different aerosol components and the size distribution is discretized into a number of size classes. All essential agglomeration and deposition processes are treated. The growth of aerosol particles by condensation is also modelled by MGA (Moving-Grid Method). The aerosol retention by engineered systems like filters, water pools (pool scrubbing), and containment sprays is modelled. Furthermore, all essential interactions with other containment processes, like the aerosol transport by gas and water flows, the depletion of aerosols, the condensation/evaporation onto/from aerosol particles, and the decay heat release from airborne and deposited aerosols are treated (Arndt et al., 1998).

In COCOSYS, the aerosol wash-down processes for soluble and insoluble aerosols are quite different. **Soluble aerosols**, like CsI, are quickly dissolved and transported with the condensate flow. The dissolution process is simplified as an instantaneous and complete dissolution of wetted particles. The model in COCOSYS for soluble aerosols was successfully validated by experiments THAI-AW and THAI-AW2 (Hoehne and Weber, 2010). THAI-AW experiment investigated the wash-down behavior of soluble CsI aerosol deposited over surfaces, while THAI-AW2 experiment was performed subsequently to investigate the wash-down behavior of both soluble CsI and insoluble SnO_2 aerosos from vertical walls and quasi-horizontal surfaces by steam condensate

(Gupta and Langer, 2009; Gupta, et al., 2012).

The wash-down of **insoluble aerosols,** like Ag and AgO_x aerosols, are more complex because the wash-down process depends on the particle properties (size and density), particle porosity, surface inclination (wall and floor), thermal-hydraulic conditions (flow patterns, condensate coverage, and fluid properties), etc. (Weber, 2011; Weber et al., 2015). The aerosol wash-down model for insoluble aerosols AULA in COCOSYS simulates the erosion of insoluble aerosols by condensate flow.

Table 2-2 Containment codes capabilities of modelling aerosol behavior

Code	Aerosol phenomena modeled					
	Release	**Dynamic behavior**				Engineered system
		Agglomeration	Deposition	Resuspension	**Wash-down**	
MELCOR	Yes	Yes	Yes	No	No	Yes
ASTEC	Yes	Yes	Yes	Yes	No	Yes
CONTAIN	Partial	Yes	Yes	No	No	Yes
COCOSYS	Partial	Yes	Yes	Yes	Yes	Yes

In summary, the four well-known containment codes (MELCOR, ASTEC, CONTAIN and COCOSYS) described above simulate the aerosol behaviors well. Their capabilities of modelling aerosol behavior are summaries in Table 2-2. Concerning the aerosol release, MELCOR and ASTEC contain the aerosol release from core degradation and MCCI, while CONTAIN and COCOSYS can only treat it partially. CONTAIN and COCOSYS can simulate the aerosol release from MCCI, but have to use an input deck to inject the aerosol released from core degradation into containment or coupling with other codes. The aerosol retention through the engineered systems, like water pools and containment spray is simulated widely. With respect to the simulation of aerosol dynamics, these four codes carry the multi-sectional and multi-component aerosol dynamic model MAEROS, so that they have the similar models of aerosol transport and deposition. COCOSYS and ASTEC model the aerosol resuspension caused by e.g. hydrogen deflagration and water pool boiling. However, except COCOSYS, the aerosol wash-down by condensate flow on the wall surface are not considered in MELCOR, ASTEC and CONTAIN. In the following section, we will introduce in detail the aerosol wash-down model AULA in COCOSYS.

- **AULA model in COCOSYS**

The aerosol wash-down model for insoluble aerosols AULA is based on an approach used in geology to describe the transport of sediments in water flow. The erosion takes place if the flow shear velocity at the wall fulfills the Shields'

criterion in sediment transport theory (Guo, 2002). The adopted Shields criterion (Shields,1936) states that particles erode if the flow shear velocity exceeds the critical shear velocity determined by particles. The AULA model suggests the surface load (surface density) (called 'concentration' in Weber et al., 2015) of deposited aerosols on walls c_{ae}, kg/m^2, decreases as an exponential function:

$$\frac{\mathrm{d}c_{ae}}{\mathrm{d}t} = -k_e \cdot c_{ae} \tag{2-1}$$

where, k_e, 1/s, is the erosion rate, i.e. the characteristic time of the erosion process, which has to be measured for each specific condition. The aerosol mass erosion rate k_e for cohesive particles is introduced by (Ariathurai, 1974):

$$k_e = \begin{cases} k_{e,0}\left(\frac{u^{*2}-u_c^{*2}}{u_c^{*2}}\right), & u^* > u_c^* \\ 0, & u^* \le u_c^* \end{cases} \tag{2-2}$$

where $k_{e,0}$ is an erosion constant that has to be estimated. This constant depends on the aerosol particle and flow properties (Weber et al., 2015; Amend and Klein, 2018). According to the Shields criterion, the erosion of particles takes place if the flow shear velocity u^* is beyond the critical shear velocity u_c^* of particles; otherwise, there is no erosion.

The critical shear velocity of particle is:

$$u_c^* = \sqrt{\tau_c/\rho} \tag{2-3}$$

where τ_c is the critical shear stress and ρ is the water density. τ_c is calculated by the critical Shields parameter, namely the dimensionless critical shear stress, which is defined as:

$$\tau_c^* = \frac{\tau_c}{(s-1)\rho g d_p} \tag{2-4}$$

where d_p is the particle diameter and g is the gravity acceleration. The density ratio s of particle to water is defined as:

$$s = \rho_p/\rho \tag{2-5}$$

In AULA, an empirical correlation of the horizontal non-cohesive particle bed (Guo, 2002) is applied. This empirical correlation is fully validated for a large range of particle size and flow velocity, which is:

$$\tau_{c,o}^* = 0.1(R^*)^{-\frac{2}{3}} + 0.054\left[1 - e^{\left(-0.1(R^*)^{\frac{2}{3}}\right)}\right] \tag{2-6}$$

where the dimensionless auxiliary parameter R^* is:

$$R^* = \frac{d_p\sqrt{0.1(s-1)gd_p}}{\nu} \tag{2-7}$$

where ν is the kinematic viscosity of water.

The deduction of the flow shear velocity u^* depends on the type of flow. Due to the slight roughness of the decontamination paint surface (a typical structure surface in containment), smooth turbulent flows can be expected (Weber et al., 2015). The shear velocity of hydraulically smooth flow is calculated by using a parabolic flow velocity profile (Hillebrand, 2008).

$$u^* = u\frac{0.41}{ln\left(\frac{u^*\delta}{\nu}\right)+5.25} \tag{2-8}$$

where u and δ are the condensate (e.g. rivulet, film) velocity and thickness respectively. The u^* can be solved by the iteration of the implicit Eq. (2-8).

The integral form of the surface load of deposited aerosols c_{ae} can be obtained by Eq. (2-1). The remaining deposited aerosol mass on water-covered area is:

$$m_{ae} = A_w \cdot \varepsilon \cdot c_{ae,0} \cdot e^{(-k_e t)} \tag{2-9}$$

where A_w is the area of the whole wall, and ε is the condensate coverage. $c_{ae,0}$, kg/m^2, is the initial surface load of deposited aerosols. Since the condensate coverage ε in AULA is a user-given value, a condensate coverage model (or a correlation) has to be proposed for the aerosol wash-down mass simulation.

Moreover, inclined walls usually exist in nuclear containment and experiments (e.g. THAI-AW3-LAB) reveal that the cohesive force cannot be neglected for the nuclear aerosols deposited on inclined surfaces (Laufenberg et al., 2014a,b). In AULA, the dimensionless critical shear stress of aerosols, known as the critical Shields parameter, is adopted as an empirical correlation but without the consideration of wall inclination and aerosol cohesion. Therefore, the dimensionless critical shear stress $\tau_{c,o}^*$ used in AULA should be corrected with the consideration of inclination angle and particle cohesion.

2.1.3 Conclusions

Aerosol wash-down is experimentally investigated in THAI and PHEBUS projects. THAI aerosol wash-down experiments cover a wide spectrum of accident scenarios and provide relevant data for the validation and development of the aerosol wash-down model implemented in containment codes. THAI aerosol wash-down experiments show that the completeness and effectiveness of the aerosol wash-down significantly depends on the condensate flow and its coverage. The tests THAI-AW3 and THAI-AW3-LAB investigate the aerosol wash-down coupling with the rivulet behavior, which exactly can be applied to validate the aerosol wash-down model, on which the

present dissertation focuses. PHEBUS FP experiments investigated the aerosol behavior in the containment under severe accident conditions and indicated aerosol wash-down occurring on the condensing surface. However, the data are not suitable for the validation of the aerosol wash-down process due to the lack of the information related to condensate flow and its coverage.

Based on the evidence of the THAI aerosol wash-down experiments, the modelling approach AULA was developed, to simulate the aerosol wash-down process on the surface for insoluble aerosols (Weber, 2011; Weber et al., 2015). The approach is taken from the transport of sediments in water flow, which is implemented in the containment code COCOSYS. The aerosol behavior and the coupling with the containment thermal-hydraulics can be also simulated in other well-known containment codes, such as MELCOR, ASTEC and CONTAIN. However, except COCOSYS, the aerosol wash-down by condensate flow on the wall is not included in these containment codes.

The review of experiments and simulation models reveals that the condensate flow and its coverage are of great importance for the aerosol wash-down efficiency. The shear stress of the condensate flow quantifies the aerosol wash-down rate. The condensate coverage indicates how much area is wetted, where the aerosol wash-down takes place. The condensate coverage should be considered in the calculation of the aerosol wash-down efficiency. However, in AULA the condensate coverage is an input value, which is given by the code user. Therefore, it is highly needed to develop models for describing the condensate flow behavior and the condensate coverage, which can be implemented in the LP containment codes.

2.2 Condensate flow model

As discussed above, the condensate flow and its coverage on the structure surface have to be considered in the aerosol wash-down assessment. Various condensate flow patterns, such as moving droplet, rivulet and fully covered film, were usually observed under different condensation conditions in experimental studies. The study of each flow pattern, e.g. the droplet velocity and geometry, etc. will be reviewed in this section.

2.2.1 Flow patterns

Condensate flow patterns are widely studied under various condensation conditions and on specific wall structures. Here we concentrate on the flow patterns on the wall in nuclear containment. Experiments of scaling nuclear containment resulted that dropwise condensation initiated on a dry surface, and formed stable rivulets (e.g. the LINX experiment, Dupont, 2017).

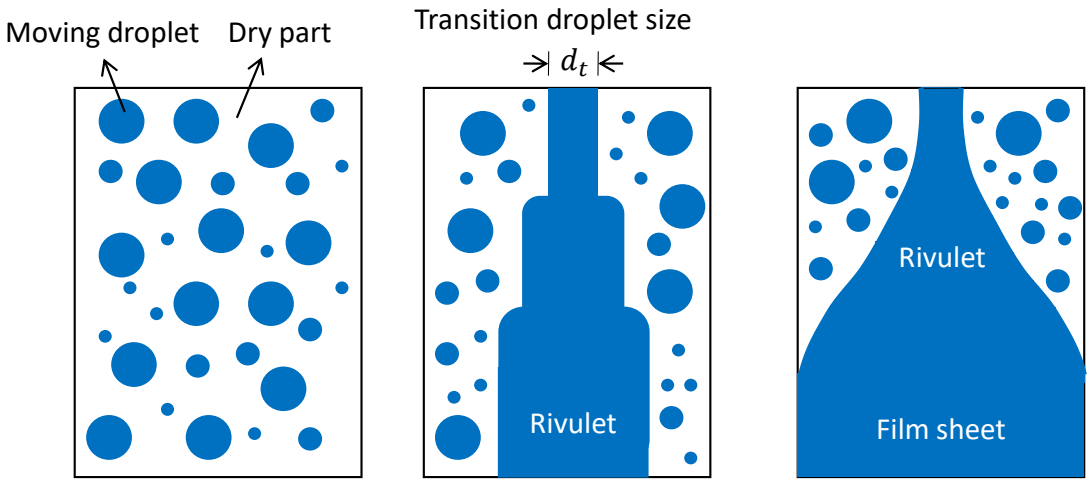

Fig. 2-4 Schematic of condensate flow patterns

One conclusion of the previous studies is that there are three condensate flow patterns on inclined surfaces in nuclear containment, i.e., the moving droplet, rivulet and fully covered film, as shown in Fig. 2-4. At beginning, the droplet generates on the dry cold surface due to the condensation and grows up until its volume reaches the threshold, beyond which the droplet starts to move downward the wall surface. The growth of the droplets is due to the condensation and the merging with other small droplets. The droplet flow is characterized by the growing size. Droplet grows up continuously during its movement until the criterion of the transition from droplet to rivulet is satisfied. That means the droplet is large enough to be out of its shape. The condensation changes from the droplet flow pattern to a transition state followed by the rivulet flow pattern. After the transition from droplet to rivulet, the initial rivulet forms.

The width of the initial rivulet spreads with the condensate flow increasing. The merging of the rivulets into a thin liquid film during the further condensation process. The last phase is about the fully covered film on the structure. The condensate coverage model for the aerosol wash-down should include all the three flow patterns. The models of these separate flow patterns (droplet, rivulet and fully covered film) are reviewed respectively.

2.2.2 Droplet model

The model of condensate droplet motion on inclined surfaces is a common fundamental phenomenon and widely used in engineering applications. A careful study of the droplet motion on solid surfaces is essential to understand and improve the application performance in aerosol wash-down. To describe a moving water droplet, the onset of droplet motion is the first issue to be considered. The models of droplet velocity and shape will also be reviewed for the description of droplet flow.

2.2.2.1 Onset of motion

Depending on the applications of the condensation droplet, it is expected that the droplets to flow downward on the solid surface. The gravity and surface tension are important to identify the conditions whether the droplet will rest on the surface (Furmidge, 1962). As shown in Fig. 2-5, for a given volume of droplet, resulting from a further increase of inclination angle, the droplet starts to move down the surface. The droplet size at the onset of motion (velocity is 0) is determined with the force balance:

$$F_g \sin\alpha = F_{\sigma,R} \cos\theta_{s,R} - F_{\sigma,A} \cos\theta_{s,A} \tag{2-10}$$

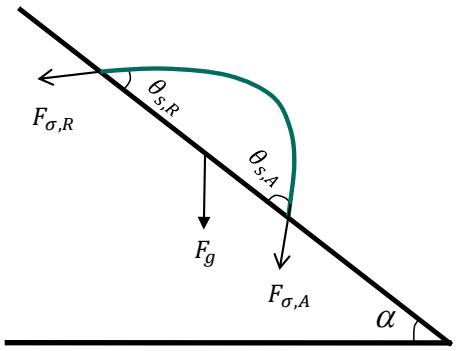

Fig. 2-5 Onset of droplet motion

The component of the gravitation parallel to the surface is:

$$F_g \sin\alpha = V\rho g \sin\alpha \tag{2-11}$$

The surface tension force parallel to the surface, denoted by F_σ, is:

$$F_\sigma = F_{\sigma,R} \cos\theta_{s,R} - F_{\sigma,A} \cos\theta_{s,A} = k \cdot 2r\sigma_{LG}\left(\cos\theta_{s,R} - \cos\theta_{s,A}\right) \tag{2-12}$$

where ρ is the droplet density, g is the acceleration of gravity, V is the droplet volume, α is the surface inclination angle, which is the angle between the surface and the horizontal direction. r is the radius of droplet wetting area, σ_{LG} is the surface tension of the gas-liquid interface (here, air-water interface),$\theta_{s,A}$ and $\theta_{s,R}$ are the apparent static advancing and receding contact angle respectively.

The factor k of the droplet surface tension force depends on the contact line contour of droplet, as shown in Table 2-3. Previous efforts (Brown et al., 1980; Dussan, 1985; Extrand et al., 1995; ElSherbini and Jacobi, 2006) to calculate the factor k resulted in values between 1.0 and 1.57, because of different assumptions and predictions of the droplet contact line contour.

Table 2-3 Factor k of droplet surface tension force

Author	k value	contour assumption
Brown et al., 1980	$\pi/2$	circular
Dussan, 1985	1.0	parallel-sided
Extrand et al., 1995	$4/\pi$	circular
ElSherbini and Jacobi, 2006	$48/\pi^3$	elliptical

The static advancing and receding contact angles are dependent on the physical and chemical properties of the surface. For the ideal chemically homogenous and smooth surface, $\theta_{s,A} = \theta_{s,R}$. On a real surface, e.g. the rough surface, the contact angle is the angle between the tangent to the gas-liquid interface and the local solid surface, which actually exhibits a range between the advancing and receding contact angle. We see in particular that both the apparent advancing/receding contact angle and the contact angle hysteresis can be dramatically affected by the surface roughness. The relationship between roughness and wettability was defined already in reference (Wenzel, 1936), where it stated that adding surface roughness will enhance the wettability.

In order to estimate the stability of rest droplets on inclined surface, the ratio of the gravitation force to the surface tension force, i.e. Bond number, is widely adopted, which is defined as:

$$Bo = \frac{\rho V^{2/3} g \sin\alpha}{\sigma_{LG}} \tag{2-13}$$

For a given surface slope, the onset of droplet motion occurs at a critical droplet volume, so that the surface tension resistance is overcome by the gravitation. The Bond number at the onset of motion, so called the critical Bond number Bo_c depends on the static advancing and receding contact angles. Reliable prediction of the onset volume depends on knowing the geometry of the droplet

and the forces acting on it at the onset condition. Dussan (1985) derived an equation to approximate the onset volume for the case of small droplet with small contact angle hysteresis ($\theta_{s,A} - \theta_{s,R} < 10°$). ElSherbini and Jacobi (2006) proposed another formula without the limitation of the contact angle hysteresis:

$$Bo_c = \frac{24}{\pi^3}\left(\frac{24}{\pi}\right)^{1/3} \frac{(\cos\theta_{s,R} - \cos\theta_{s,A})\sin\frac{\theta_{s,A}+\theta_{s,R}}{2}}{\left(2 - 3\cos\frac{\theta_{s,A}+\theta_{s,R}}{2} + \cos^3\frac{\theta_{s,A}+\theta_{s,R}}{2}\right)^{1/2}} \tag{2-14}$$

So, for given static contact angles, the critical Bond number Bo_c is acquired. For given inclination and fluid properties further, the droplet volume at its onset of motion is obtained.

2.2.2.2 Droplet velocity

When the droplet volume or inclination angle becomes larger than the threshold value of onset of motion, the droplet sliding occurs. The droplet could move at constant velocity in steady state condition. Except the gravitation force and the surface tension force, the viscous force should be also considered to evaluate the droplet moving velocity, as shown in Fig. 2-6.

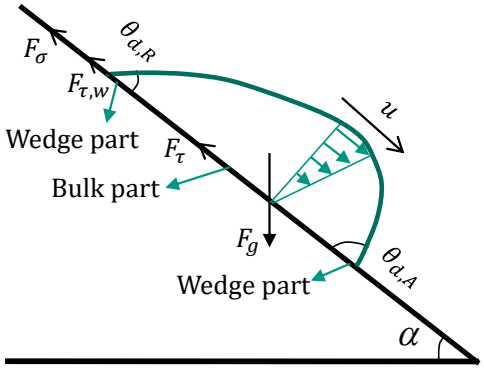

Fig. 2-6 Forces acting on moving droplet on inclined surface

The viscous force at the solid-liquid interface is determined by the liquid viscosity and the velocity gradient there. The viscous force at the gas-liquid interface is neglected here. The viscous force at the solid-liquid interface is determined by the liquid viscosity and the velocity gradient there. This viscous dissipation consists of a flat bulk (central) part mainly governed by gravity and a wedge (edge) part where the capillarity takes effect (Kim et al., 2002).

When the droplet slides at low Reynolds number Re ($Re < 1$), the velocity field in the bulk part can be assumed to obey the lubrication approximation, whereas the velocity field in the wedge part must be described using the Stokes equation. De Gennes (1985) and Kim et al. (2002) think that the viscous forces $F_{\tau,w}$ acting on the wedge part of droplet near the contact line, as shown in Fig. 2-6, dominates viscous dissipation when the droplet diameter is smaller than the capillary length $\sqrt{\sigma_{LG}/\rho g}$. When the droplet diameter is much larger than capillary length, the viscous force F_τ from the shear stress associated with the

bulk part of droplet, dominates the viscous dissipation.

The force balance of the moving droplet in the moving direction is:

$$F_g \sin\alpha = F_\sigma + F_{\tau,w} + F_\tau \tag{2-15}$$

where F_σ is the component of the surface tension force parallel to the surface, expressed as in Eq. (2-12). According to the knowledge of the literature (Kim et al., 2002; Puthenveettil et al., 2013), the viscous forces $F_{\tau,w}$ acts on the wedge part can be expressed as:

$$F_{\tau,w} = 4\mu u P c_1(\theta_e) ln\left(\frac{L_a}{L_s}\right) \tag{2-16}$$

where $P = 2\pi r$ is the droplet contact area perimeter. Sliding droplet shape usually can be approximated as a spherical cap. The apparent (macroscopic) length L_a, is an order of 1 mm while the microscopic cut-off length scale L_s is the slip length of a few molecular lengths with the order of 100 nm. Here $ln\left(\frac{L_a}{L_s}\right)$ is approximated as 9.2. $c_1(\theta_e)$ is a function of equilibrium contact angle, which is derived by Kim et al. (2002) and Varagnolo et al. (2013) based on the Stokes flow velocity field solution.

$$c_1(\theta_e) = \frac{(1-cos^2\theta_e)}{(\theta_e - sin\,\theta_e\, cos\,\theta_e)} \tag{2-17}$$

The viscous force F_τ of the bulk part of droplet depends on droplet internal velocity gradient close to the solid surface:

$$F_\tau \propto \mu A \frac{u}{\Delta y} = \mu u V^{1/3} c_2(\theta_e) \tag{2-18}$$

where $u/\Delta y$ is the internal velocity gradient since the lubrication theory is usually used to scale the velocity gradient. A is the droplet contact area while Δy is the height (thickness) of the droplet. Both of them are dependent on the droplet shape, e.g. the contact angle (Meric and Erbil, 1998). The function of equilibrium contact angle $c_2(\theta_e)$ can be approximated by droplet geometry model as shown in section 2.2.2.3:

$$c_2(\theta_e) = \frac{A}{\Delta y V^{1/3}} = \left(\frac{\pi sin^3\theta_e}{2-3\,cos\,\theta_e + cos^3\theta_e}\right)^{2/3} \left(\frac{3(2+cos\,\theta_e)}{1-cos\,\theta_e}\right)^{1/3} \tag{2-19}$$

Substituting the viscous forces $F_{\tau,w}$ and F_τ into the force balance Eq. (2-15):

$$\rho V g \sin\alpha = 2kr\sigma_{LG}\left(cos\,\theta_{s,R} - cos\,\theta_{s,A}\right) + 4\mu u P c_1(\theta_e) ln\left(\frac{L_a}{L_s}\right) + \mu u V^{1/3} c_2(\theta_e) \tag{2-20}$$

Both sides of the equation divided by $\sigma_{LG} V^{1/3}$ and expressed with Bo number:

$$\frac{\mu u}{\sigma_{LG}}\left(\frac{4P c_1(\theta_e) ln\left(\frac{L_a}{L_s}\right)}{V^{1/3}} + c_2(\theta_e)\right) = Bo - Bo_c \tag{2-21}$$

$$Ca \cdot c_3(\theta_e) = Bo - Bo_c \tag{2-22}$$

The definition of the dimensionless parameter Capillary number is:

$$Ca = \frac{\mu u}{\sigma_{LG}} \tag{2-23}$$

Substituting the expressions of droplet perimeter P, droplet volume V as shown in section 2.2.2.3 and $ln\left(\frac{L_a}{L_s}\right)$ into Eq. (2-21) and comparing with Eq. (2-22), the function of equilibrium contact angle combined the viscous effects of the wedge and bulk parts $c_3(\theta_e)$ is:

$$c_3(\theta_e) = 53.1\pi^{2/3}\left(\frac{sin^3\theta_e}{2-3\,cos\,\theta_e+cos^3\theta_e}\right)^{1/3} c_1(\theta_e) + c_2(\theta_e) \tag{2-24}$$

The contact angle hysteresis is independent of the droplet size at the onset of motion. The advancing/receding contact angle can be assumed not to change much when droplet slides slowly. Therefore, $c_3(\theta_e)$ can be considered as a constant as well as $c_1(\theta_e)$ and $c_2(\theta_e)$.

Eq. (2-22) is a classic linear scaling law of moving droplet velocity in a low-velocity regime (Podgorski et al., 2001; Kim et al., 2002). Capillary number Ca linearly depends on Bond number Bo with its slope determined by the surface properties. Although this result is obtained through the approximate modeling, the linear relationship between Ca and Bo is suggested to estimate the steady sliding velocity of a water droplet on a specific surface in a low velocity regime. This conclusion is validated widely against the experimental data (Mannetje et al., 2014). The slope and intercept of the linear scaling law depend on the static advancing and receding contact angles.

However, there are few investigations in the literature of the droplet velocity model at relatively high Re ($Re \gg 1$) number, which is still of considerable fundamental interest. For instance, there is a boundary layer inside the fast moving droplet above the contact area at the liquid-solid interface, which is assumed in reference (Puthenveettil et al., 2013). However, it does not mention the layer is related to the droplet internal flow field. Puthenveettil et al., also provide the velocity thresholds of water and mercury droplets on glass surface transforming to rivulet respectively, but the criterion of the transition from droplet to rivulet is still not clear so far. In addition, droplet velocity model rarely consider the dynamic contact angles, especially when the droplet is moving at high Re. In order to estimate the velocity of a fast moving droplet, the surface tension force acting on the droplet is necessary to adopt the dynamic contact angle model.

- **Dynamic contact angle**

Lots of studies on the dynamic contact angles indicate they are monotonous with contact line velocity (Dussan, 1976; Voinov, 1976; De Gennes, 1985; Cox, 1986, 1998; Blake, 2006). The droplet velocity model at low Re considers the

static contact angles for the surface tension force, since the minor change of droplet shape is assumed. However, the geometry of the droplet may change dramatically when the droplet moves fast. The dynamic contact angle hysteresis ($\theta_{d,A} - \theta_{d,R}$) is caused by the interplay of the liquid motion with the solid surface. Notably, there is a clear velocity dependence of these dynamic contact angles. The dynamic advancing contact angle increases, but the dynamic receding angle decreases with the growth of droplet velocity. The consistency of the dynamic contact angle models is usually assessed as:

$$f(\theta_d, \theta_s) \propto \pm Ca \tag{2-25}$$

when the droplet slides at a low speed (valid for $Re < 1$). A simplification was often made, e.g., using $\theta_{s,A}$ for the 'advancing' curve, and $\theta_{s,R}$ for the 'receding' curve. It is difficult to give a proper assessment, because most of these models have one or two fitting parameters, which complicates the comparison among these models. Early, the empirical linear model $\theta_d - \theta_s \propto \pm Ca$ is applied. Later, the third order form is a typical model for droplet moving at a moderate speed (Voinov, 1976), which is usually adopted for dynamic contact angle evaluation:

$$\theta_d^3 - \theta_s^3 \propto Ca \tag{2-26}$$

For the prediction of dynamic receding contact angle, the above model can get a good agreement with the experimental data, since the variation of dynamic receding contact angles is not so large.

For dynamic advancing contact angle, Cox (1998) concludes it is determined by the droplet Reynolds number, and emphasizes the inertia should not be ignored. The Cox (1998) model of the dynamic advancing contact angle considers the fluid inertial effect when droplets move at a high speed, namely the dynamic contact angle model includes the Re effect. This model is a theoretical result of advancing contact line moving under the situation of large Re, in which the inertia effect dominates. The Cox model for predicting the advancing contact angle is expressed as:

$$Ca \cdot ln\left(\frac{L_a}{L_s} Re^{-1}\right) = g_v(\theta^*) - g_v\left(\theta_{s,A}\right) \tag{2-27}$$

$$Ca \cdot ln(Re) = g_{iv}\left(\theta_{d,A}\right) - g_{iv}(\theta^*) \tag{2-28}$$

where θ^* is an intermediate variable in the Cox model. The functions of contact angle are:

$$g_{iv}(\theta) = 1{,}53162(\theta - sin\,\theta) \tag{2-29}$$

$$g_v(\theta) = \int_0^\theta \frac{\theta - sin\,\theta\, cos\,\theta}{2\, sin\,\theta} \tag{2-30}$$

The subscript v and iv mean viscous and inviscid respectively. The definition Re number in Cox model is $Re = \frac{\rho u r}{\mu}$.

- **Marangoni effect**

Containment structure plays a role as the heat sink during accidents. Condensation on the structure surface stores and removes the heat released. The temperature gradient between the cold surface and the condensate gas-liquid interface is expected. E.g. there is a large temperature gradient (tens of degrees) usually set up across the condensate on AP600's containment inner shell (Herranz et al., 1998). Therefore, the Marangoni effect on droplet velocity should be also considered, because of the surface tension gradient, caused by the temperature gradient between the cold solid surface and the hot gas bulk, as seen in Fig. 2-7.

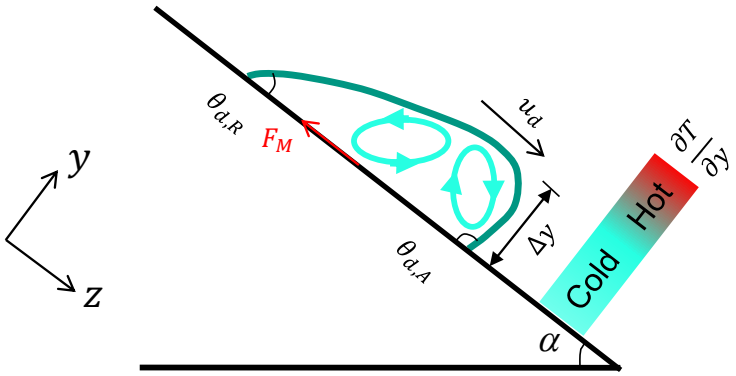

Fig. 2-7 Schematic of Marangoni effect on droplet

The Marangoni effect influences the droplet velocity as an equivalent Marangoni force acting on the droplet. The basic expression structure of the equivalent Marangoni force comes from the references (Gallaire et al., 2014; Won et al., 2017), which is expressed empirically proportionally to the product of the change of surface tension $\Delta\sigma_{LG}$ and the droplet diameter $2r$:

$$F_M \propto \Delta\sigma_{LG} \cdot 2r \tag{2-31}$$

The proportional constant is related to the given droplet shape. The surface tension changes perpendicularly to the droplet moving direction, which is dependent on the temperature gradient:

$$\Delta\sigma_{LG} = \frac{\partial\sigma_{LG}}{\partial T}\frac{\partial T}{\partial y}\Delta y \tag{2-32}$$

where $\frac{\partial\sigma_{LG}}{\partial T}$ is the surface tension gradient with respect to temperature; $\frac{\partial T}{\partial y}$ is the temperature gradient in y- direction; Δy is the droplet height.

Originally, the empirical expression of the equivalent Marangoni force is valid for the case that the surface tension changes at the droplet moving direction. However, it indicates in the literature that two Marangoni convections occur inside the droplet advancing and receding parts respectively (Phadnis and Rykaczewski, 2017), as shown in Fig. 2-7. The attractive effect (in the droplet

moving direction) of the advancing sub-convection and the repulsive effect (in the opposite droplet moving direction) of the receding sub-convection depend on the dynamic advancing and receding contact angle, respectively. Therefore, it needs to consider both the attractive and repulsive force part, in order to express the Marangoni effect on droplet velocity.

2.2.2.3 Droplet geometry

Once the water droplet starts moving, it is clear that the droplet shape, e.g. contact angles, depend on velocity. The shape does not change much with low velocity. When droplet moves fast, the dynamic advancing contact angle $\theta_{d,A}$ increases, but the dynamic receding angle $\theta_{d,R}$ decreases with the growth of droplet velocity. To simplify the real droplet geometry model, droplet shape is approximated as a spherical cap (Meric and Erbil, 1998). The droplet radius can be given:

$$r = \left(\frac{3V}{\pi}\frac{sin^3\theta_e}{2-3\,cos\,\theta_e+cos^3\theta_e}\right)^{1/3} \tag{2-33}$$

with the equilibrium contact angle:

$$\theta_e = \left(\theta_{s,A} + \theta_{s,R}\right)/2 \tag{2-34}$$

Then the droplet wetting area $A = \pi r^2$.

The average droplet height can also be approximated:

$$\Delta y = \left(\frac{3(1-cos\,\theta_e)V}{\pi(2+cos\,\theta_e)}\right)^{1/3} \tag{2-35}$$

2.2.3 Rivulet model

Plenty of theoretical and experimental investigations regarding rivulet formation have been carried out and it revealed that a critical rivulet thickness (height) is dependent on surface tension, contact angle and other physical properties. The critical height of rivulet is investigated by the application of minimum total energy (MTE) principle originated with the work of Hartley and Murgatroyd (1964). It suggests that a stable rivulet structure is reached if the total energy, which consists of kinetic and surface energy, is minimized.

The critical thickness of rivulet, which is denoted by δ, refers to the height of rivulets if the equilibrium, stationary state of the rivulet is fulfilled (Doniec, 1988, 1991). The related studies mainly focus on the critical state of a rivulet by specifying its profile of cross section, e.g. as shown in Fig. 2-8, and calculating the corresponding velocity distribution, which has considered the contact angle. Moreover, when countercurrent air is imposed on the gas-liquid interface of rivulets, the velocity profile could be changed; subsequently the critical state is changed. Regarding the influence of interfacial shear, Hartley and Murgatroyd

(1964) derived the critical state of the fully covered film under the surface shear on the horizontal plate. El- Genk and Saber (2001), Huang and Cheng (2014) derived the critical state of the falling rivulet under countercurrent flow with MTE principle.

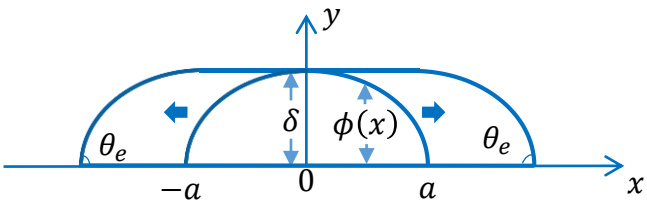

Fig. 2-8 Cross section of rivulet

One conclusion is obtained that the MTE principle is widely examined for determining the rivulet thickness of an isothermal rivulet flowing down a sloped wall. In previous researches (Hartley and Murgatroyd, 1964; Hobler, 1964; Doniec, 1988, 1991; El-Genk and Saber, 2001; Huang and Cheng, 2014), analytical velocity and geometry structure expressions of a stable rivulet are developed. Summaries from the literature review reveal that the derived empirical rivulet thickness correlation is:

$$\delta = c_\delta \cdot (1 - cos\theta_e)^{0.2} \left[\frac{\mu^2 \sigma_{LG}}{(\rho^3 (g sin\alpha)^2)}\right]^{0.2} \tag{2-36}$$

where the equilibrium contact angle θ_e is adopted. c_δ is the prefactor of the empirical rivulet thickness expression, which varies in the range of (1.125 -1.86), as shown in Table 2-4.

Table 2-4 Prefactor of empirical rivulet thickness expression

Reference	Hartley and Murgatroyd,1964	Doniec, 1988, 1991	Hobler,1964
prefactor	1.34	1.45	1.86
	1.72	1.125	

As assumed in many previous studies on the structure of rivulets, when it reaches the critical state, the rivulet structure is regarded as a circular segment in the cross section, as demonstrated in Fig. 2-8. The initial rivulet after the transition consists of two arc parts. Half width (one arc) of the initial rivulet is:

$$a = \frac{sin\theta_e}{1 - cos\theta_e}\delta \tag{2-37}$$

According to the initial rivulet structure, the thickness in the two arc parts is:

$$\phi(x) = \delta - \frac{\delta}{1 - cos\theta_e}\left[1 - \sqrt{1 - x^2\left(\frac{1 - cos\theta_e}{\delta}\right)^2}\right], -a \le x \le a \tag{2-38}$$

The rivulet velocity distribution from the wall to the rivulet interface with gas is assumed as a parabolic profile (El-Genk and Saber, 2001), so that the rivulet velocity distribution is:

$$u = \frac{\rho g sin\alpha}{\mu}\left(y\phi - \frac{y^2}{2}\right) \tag{2-39}$$

Therefore, the average rivulet velocity is:

$$\bar{u} = \frac{1}{\phi}\int_0^{\phi} \frac{\rho g sin\alpha}{\mu}\left(y\phi - \frac{y^2}{2}\right) dy = \frac{\rho g sin\alpha}{3\mu}\phi^2 \tag{2-40}$$

Another question is how the rivulet geometry changes. It is usually assumed that the contact angle stays constant whether the rivulet flow rate increases or decreases. That is because the rivulet edges spread or shrink moderately when the rivulet flow rate varies. Therefore, the equilibrium contact angle adopted is related to the static advancing and receding contact angles instead of the dynamic ones. Doniec proposed that the rivulet width would increase and its thickness would not change in case of increasing the flow rate. This point of view supported by El-Genk and Saber demonstrates the configuration of the rivulet with the flow rate changing. Therefore, the profile of the rivulet cross section is regarded as circular segments at rivulet edges and a rectangular film sheet in the middle, as seen in Fig. 2-8.

2.2.4 Film model

In case of fully covered film on surfaces, the coverage is 100%, which is not the focus in the current discussion. However, the film velocity is still an input parameter of the calculation of the film shear velocity that influences the erosion process of aerosol on the surface.

- **Nusselt film theory**

For the film on inclined walls, Nusselt (1916) provided his theory predicting the relationship between film flow rate and film thickness. In his theory, assumptions have been made that the film flow is free falling, in absence of wave and without shear stress on the gas-liquid interface. For a steady, incompressible, and Newtonian liquid film flowing down a solid surface, the simplified Navier-Stokes equation can be expressed as:

$$\mu\frac{\partial^2 u}{\partial y^2} = -\rho g sin\alpha \tag{2-41}$$

The momentum equation is subject to the boundary conditions: 1, velocity at solid–liquid interface is zero; 2, the velocity gradient at gas-liquid interface is zero. By integrating the simplified Navier-Stokes equation, it yields:

$$u = \frac{\rho g sin\alpha}{\mu}\left(y\delta - \frac{y^2}{2}\right) \tag{2-42}$$

where δ stands for the film thickness. u is the film velocity, which is expressed similarly to rivulet velocity. This expression indicates that the velocity distribution depends on y with being regarded as a one-dimensional parabolic profile. The volume flow rate per unit width can be obtained:

$$\dot{V} = \int_0^{\delta} u(y)dy \tag{2-43}$$

Thus, the film thickness is expressed as:

$$\delta = \left(\frac{3}{4}\right)^{1/3} Re^{1/3} \left(\frac{\mu^2}{\rho^2 g sin\alpha}\right)^{1/3} \tag{2-44}$$

where the definition of Reynolds number of the film is $Re = \frac{4\rho\dot{V}}{\mu}$. Furthermore, based on Nusselt's theory, the above film thickness form has been widely used for empirical correlations in predicting the thickness of the falling film. Nusselt's theory is reliable to predict the falling film thickness with a given volume flow rate. The wall condensation model has been developed for COCOSYS to capture the condensation and evaporation of the liquid film on structure surfaces. The velocity distribution complies with Nusselt's theory and the water film thickness is calculated based on the mass conservation, which is dependent on the incoming water flow and the condensation/evaporation rate on structures.

- **Empirical correlations of film thickness**

Film instability is one of the most significant characteristics of the film flow pattern, which results in the generation of the random surface wave. The small disturbance is produced on the film surface as it flows down and gradually develops into big solitary waves. The wave behavior on film flow has been studied for several decades. Moran, et al. (2002), Yu and Cheng (2014) experimentally investigated the hydrodynamic characteristics of laminar falling films on an inclined plate with a photochromic dye activation technique. The time-averaged film thickness was slightly under-predicted and the velocity profile was in agreement with Nusselt's theory.

Numerous studies have been conducted to investigate the behaviors (e.g. the time-averaged film thickness and velocity) of water film freely falling down a vertical or inclined plate. Many of such studies approximated the results of time-averaged film thickness with empirical correlations, as listed in Table 2-5.

Most of these experimental results indicated that Nusselt's prediction was in good accordance with experimental data for the flow regime with Reynolds number smaller than about 1500, even though waves on the film surface have been generated. Nevertheless, the empirical correlations for time-averaged film thickness is an alternative option in case of the film Re number is relatively large.

Table 2-5 Empirical correlations for time-averaged film thickness δ

Author	Re range	Reported equation of δ
Nusselt, 1916	$0 < Re <$ 1000-2000	$0.909Re^{1/3}(\mu^2/(\rho^2 g sin\alpha))^{1/3}$
Takahama and Kato, 1980	$Re >$ 1472	$0.228Re^{0.526}(\mu^2/(\rho^2 g sin\alpha))^{1/3}$
Karapantsios et al., 1989	$500 < Re <$ 13000	$0.214Re^{0.538}(\mu^2/(\rho^2 g sin\alpha))^{1/3}$
Jiang and Yan, 1996	$400 < Re <$ 5000	$0.295Re^{0.498}(\mu^2/(\rho^2 g sin\alpha))^{1/3}$
Yu et al., 2012	$80 < Re <$ 900	$0.462Re^{0.422}(\mu^2/(\rho^2 g sin\alpha))^{1/3}$

2.2.5 Conclusions

There is no condensate coverage model in the literature, which is feasible to be coupled in LP containment codes for aerosol wash-down simulation. Concerning the condensate flow, three patterns, such as moving droplet, rivulet and fully covered film usually occur under accident conditions.

Many studies on droplet flow are presented in the literature, which include the onset of droplet motion, droplet velocity, droplet shape, etc. With respect to the velocity model of fast moving droplets, few investigations are presented in the literature and there still exist considerable fundamental interest. The droplet velocity model at high Re number needs to be improved with the consideration of the internal flow field effect. In addition, the droplet velocity model should also consider the change of the dynamic contact angle when the droplet moves fast, in order to accurately estimate the resistance caused by surface tension. Furthermore, the Marangoni effect on droplet velocity should not be ignored, due to the surface tension gradient between the cold solid surface and the hot gas bulk.

Few studies of the transition from droplet to rivulet are presented in the literature. Puthenveettil et al. (2013) provides the velocity thresholds of water and mercury droplets on a glass surface, but these thresholds are very different from case to case. It is necessary to investigate a generic transition criterion that can be feasible to estimate the transition from water droplet to rivulet on containment structure surface.

Nevertheless, the rivulet and film models are widely investigated and reliable to be adopted in the description of their corresponding condensate flow patterns.

3 MODEL DEVELOPMENT

According to the conclusions of the literature review, there is still much room for the improvement of the related models for aerosol wash-down simulation. The important parameter condensate coverage should be coupled to calculate the aerosol wash-down process. However, there is no condensate coverage model published which is feasible to be implemented in LP containment codes.

The condensate flow patterns, such as moving droplet, rivulet and fully covered film not only crucially affect the aerosol wash-down erosion rate, but also have to be considered in the prediction of the condensate coverage. Moreover, the model of droplet velocity moving down on inclined surface at high Re is still of interest. It is necessary to investigate a criterion of the transition from water droplet to rivulet on containment structure surface. Furthermore, the dimensionless critical shear stress in the aerosol wash-down model, AULA, is adopted as a correlation without the consideration of wall inclination and aerosol cohesion effects.

The items of the model development in this dissertation are briefly summarized as follows:

- Improve the droplet velocity model
- Propose the criterion of the transition from droplet to rivulet
- Propose the condensate coverage model
- Modify the dimensionless critical shear stress by considering the effects of the inclination and the aerosol cohesion

3.1 **Modelling approach**

The target of this section is to find a modelling approach to describe the condensate flow patterns and the condensate coverage, which should be feasible to be implemented in the nuclear LP containment codes, e.g. COCOSYS. The parameters usually provided by containment codes are the volume flow rate and temperature of condensate, the temperature and pressure of the containment atmosphere, wall temperature, the structure geometry and material, etc. The parameters needed for aerosol wash-down simulation are the velocity profile (shear stress) and the condensate coverage. Therefore, the process of the modelling approach has to connect the input given by the containment codes and the output for simulating aerosol wash-down process, as shown in Fig. 3-1.

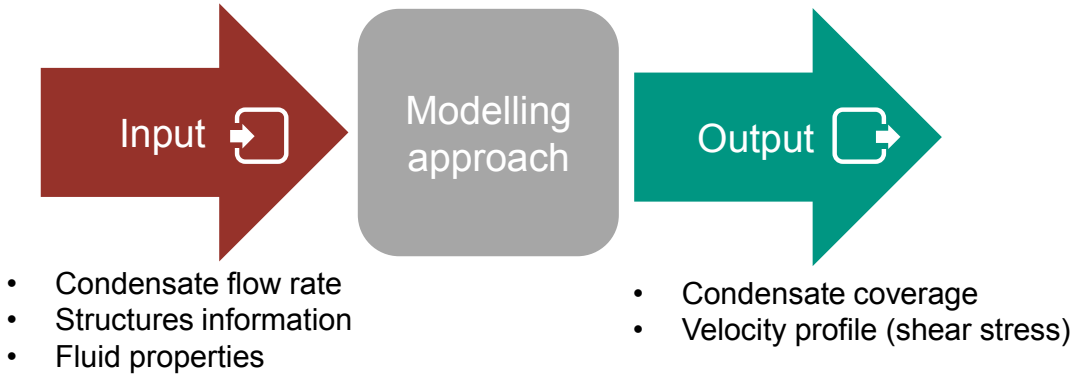

Fig. 3-1 Schematic of the modelling approach

However, the containment codes usually cannot offer a single droplet or rivulet motion trajectory along the wall surface but the total volume flow rate of them. The challenge in the modelling approach is how we consider the condensate flow patterns and their integral effect on coverage. Therefore, the modelling approach is separated into two steps: microscopic and macroscopic treatment. The flow patterns in the condensate moving trace are considered in the microscopic treatment, while the amount of droplets and rivulets are calculated in the macroscopic treatment. The average thickness and velocity of the condensate are expressed as functions of the condensate flow rate offered by the containment codes. Consequently, the condensate coverage can be obtained in terms of the condensate flow rate.

- **Microscopic treatment**

This step considers the movement of droplet and rivulet as an isolated single trace. The aim of this step is to calculate the condensate parameters of moving droplet and rivulet along the moving direction, such as the volume, wetting area, thickness and velocity. The condensate volume can be expressed as:

$$V = V_0 + \Delta V_{cond} = V_0 + \int_0^h \frac{Aq}{\rho \Delta h_{fg}} \cdot \frac{dz}{u} \quad (3\text{-}1)$$

where V_0 is the droplet volume at its onset of motion, beyond which the droplet starts to move downwards. ΔV_{cond} is the volume increase of the moving droplet or rivulet due to condensation during its movement, which is the integral of all condensate along the moving trace, as seen in Fig. 3-2.

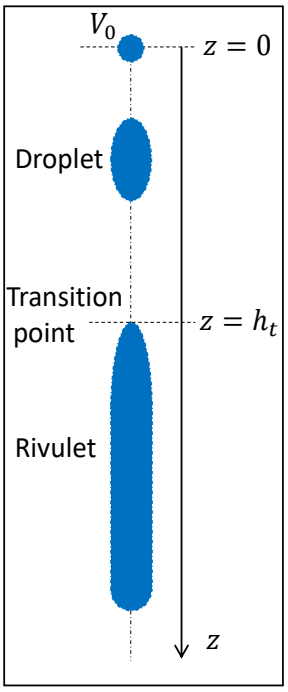

Fig. 3-2 Schematic of microscopic treatment

Since both wetting area A and velocity u of droplet and rivulet depend on their volume V (for given contact angles, wall inclination and fluid properties), the droplet and rivulet volume along the height (moving distance) h can be obtained as a numerical solution for given condensation heat flux q. Once the volume is obtained, the velocity, wetting area and average thickness can also be calculated simultaneously. According to the transition criterion (to be discussed later), the critical height h_t and the critical droplet volume V_t are obtained, at which the transition from moving droplet to rivulet happens.

In order to complete the calculation of the single trace, the following separate models of different flow patterns are requisite: the droplet behavior (onset of motion, velocity and structure), the transition from droplet to rivulet, and the rivulet behavior (velocity and structure).

The droplet size at the onset of motion is determined by the critical Bond number Bo_c, which is in terms of the static advancing and receding contact angle. Thus, for given surface inclination, equilibrium contact angle and fluid properties, the droplet volume at its onset of motion V_0 is obtained. To simplify the real droplet geometry model, droplet shape is approximated as a spherical cap. The droplet radius can be given with the equilibrium contact angle as well

as the droplet wetting area and the average thickness. If the droplet size grows further due to the condensation, the droplet will move fast. However, the velocity model of the fast moving droplet should be improved, e.g. the forces acting on the droplet with the considerations of its internal flow field. In addition, the criterion of the transition from moving droplet to rivulet is still absent.

The initial rivulet velocity and structure after the droplet transition are solved by the rivulet model. The MTE method offers the determination of the thickness of an isothermal rivulet flowing down a sloped wall, including the initial rivulet geometry (e.g. the thickness in the two side arc parts) and the rivulet velocity distribution. When the volume flow rate increases further, the rivulet spreads at both sides continuously, and a rectangular film sheet forms and extends in the middle with a constant thickness.

- **Macroscopic treatment**

Based on the above microscopic treatment, the second step of the modelling approach is the integral of all the isolated single traces of droplet and rivulet, with an assumption that all the initial droplets and rivulets have their identical structures respectively. The schematic of macroscopic treatment is shown in Fig. 3-3.

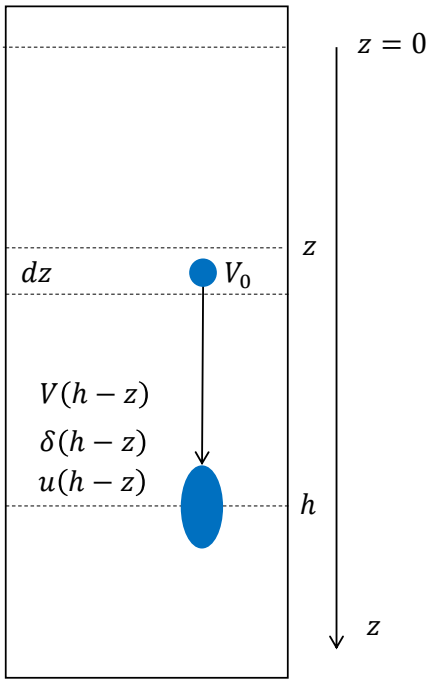

Fig. 3-3 Schematic of macroscopic treatment

In order to figure out the amount of droplets and rivulets generated on the surface, the droplet initiation density n_d (unit: 1/(m^2·s), droplet generation number per area and per time) is introduced. Based on the energy conservation, the droplets initiation density can be expressed as:

$$n_d = \frac{q}{\Delta h_{fg} \cdot \rho \cdot V_0}(1-\varepsilon) \tag{3-2}$$

where Δh_{fg} is the specific latent heat of vapor condensation and ε is the condensate coverage. $(1-\varepsilon)$ is the non-covered area fraction, which means the initiation of moving droplets only occurs in the non-covered area (i.e. non-wetting area). The new initiated moving droplet rate per width (unit: 1/(m·s)) in the interval $\mathrm{d}z$ at each elevation h (as shown in Fig. 3-3) is:

$$n_d \cdot \mathrm{d}z = \frac{q}{\Delta h_{fg} \cdot \rho \cdot V_0}(1-\varepsilon) \cdot \mathrm{d}z \tag{3-3}$$

The volume flow rate per width $\dot{V}$, m^3/(m·s), at each height h is the integration from the top of structure $z=0$ to the height h of interest, which can be calculated by:

$$\dot{V} = \int_0^h V(h-z) \cdot n_d \mathrm{d}z \tag{3-4}$$

It is notable that the volume of condensate (droplet and rivulet) used in the integral equation should consider the moving distance from the droplet initial position to the position of interest. So the volume in the integral equation is $V(h-z)$ rather than $V(z)$. The volume for each specific droplet and rivulet can be obtained in the microscopic treatment as well as the thickness $\delta(h-z)$ and velocity $u(h-z)$. The average thickness $\bar{\delta}$ and average velocity $\bar{u}$ can be also obtained as below:

$$\bar{\delta} = \frac{\int_0^h \delta(h-z) \cdot n_d \mathrm{d}z}{\int_0^h n_d \mathrm{d}z} \tag{3-5}$$

$$\bar{u} = \frac{\int_0^h \rho \cdot V(h-z) \cdot u(h-z) \cdot n_d \mathrm{d}z}{\int_0^h \rho \cdot V(h-z) \cdot n_d \mathrm{d}z} \tag{3-6}$$

where the average thickness is weighted by the total amount of droplets and rivulets, and the average velocity is weighted by the total mass of them. Therefore, the condensate coverage averaged over plate surface can be obtained by:

$$\varepsilon = \frac{\dot{V}}{\bar{u} \cdot \bar{\delta}} \tag{3-7}$$

When the first generation of droplets has already moved to the critical height, h_t, the transition happens. After this position, the droplets and rivulets are coexisting on the surface, as shown in Fig. 3-4.

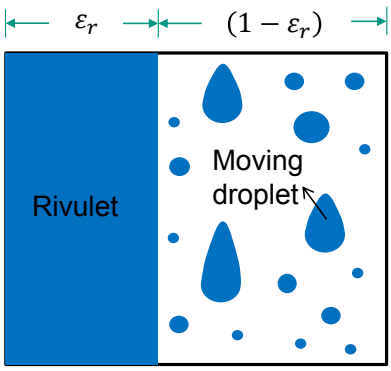

Fig. 3-4 Coexisting phase of droplets and rivulets

During the coexisting phase, the rivulet volume flow rate per width $\dot{V}_r$ at each height h (larger than h_t), can be calculated by:

$$\dot{V}_r = \int_0^{h-h_t} V(h-z)\cdot n_d \mathrm{d}z \tag{3-8}$$

The lower and upper limit of the integration in the above equation are 0 and $h-h_t$, respectively, which means all the droplets generated in the height range $(0, h-h_t)$ are already transformed to rivulets. In a similar way, the average thickness $\bar{\delta}_r$ and velocity $\bar{u}_r$ of rivulet can also be obtained as below:

$$\bar{\delta}_r = \frac{\int_0^{h-h_t} \delta(h-z)\cdot n_d \mathrm{d}z}{\int_0^{h-h_t} n_d dz} \tag{3-9}$$

$$\bar{u}_r = \frac{\int_0^{h-h_t} \rho\cdot V(h-z)\cdot u(h-z)\cdot n_d \mathrm{d}z}{\int_0^{h-h_t} \rho\cdot V(h-z)\cdot n_d \mathrm{d}z} \tag{3-10}$$

Thus, in the coexisting phase, the rivulet coverage averaged over the plate surface can be obtained by:

$$\varepsilon_r = \frac{\dot{V}_r}{\bar{u}_r\cdot\bar{\delta}_r} \tag{3-11}$$

3.2 **Condensate flow**

In order to support the modelling approach, the models of each condensate flow pattern have to be provided. As discussed in the literature review, the partial droplet model, the rivulet and film models are widely investigated, which are the reliable models to be adopted in the description of their corresponding condensate flow patterns. However, the droplet velocity model and the criterion of the transition from droplet to rivulet have to be improved and newly developed respectively.

3.2.1 Droplet velocity model

Two aspects of the velocity model of fast moving droplets should be improved. The viscous force acting on droplet bulk part should be with the consideration of its internal flow field, namely the effect of Re. The Marangoni effect inside the droplet should also be considered due to temperature gradient under condensation condition. The equivalent Marangoni force here acting on moving droplet is valid for the whole velocity regime (both low and high Re). The forces acting on a fast moving droplet are shown in Fig. 3-5. For the force balance at the moving direction, the expression can be written as:

$$F_g \sin\alpha = F_\sigma + F_{\tau,w} + F_\tau + F_M \tag{3-12}$$

where four force items on the right side are the resistance against droplet motion. F_σ is the surface tension force. $F_{\tau,w}$ is the viscous force acting on the droplet wedge part close to the contact line. The viscous force of the droplet bulk part F_τ and the equivalent Marangoni force F_M are going to be improved and proposed respectively in the following sections.

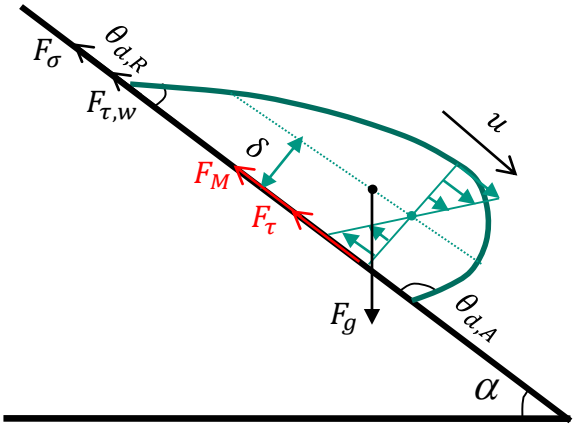

Fig. 3-5 Forces acting on moving droplet at high Re

- **Viscous force of the bulk part F_τ**

The viscous force F_τ is determined by the velocity gradient inside the droplet. The velocity gradient is assumed as a linear distribution, when the droplet moves slowly (Podgorski et al., 2001; Kim et al., 2002). In case of droplet moving fast, the internal flow field of droplet seems to be a rotating flow field, as shown in Fig. 3-5 and zoomed in Fig. 3-6, blue, which is usually observed both in experiments (Sakai et al., 2006; Song, 2008; Suzuki et al., 2008) and Computational Fluid Dynamics (CFD) simulations (Sikarwar et al., 2010). One is expected that the viscous force of the bulk part of the droplet is concentrated on the solid surface. The linear velocity gradient assumption of the moving droplet is no longer valid when the internal rotating flow field is considered. Meanwhile, the whole droplet has an average velocity (Fig. 3-6, yellow) moving downwards.

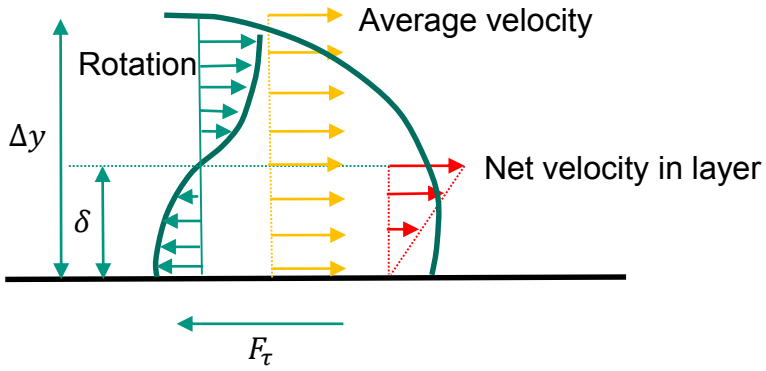

Fig. 3-6 Internal flow field of moving droplet

A layer with thickness δ occurs when a droplet moving fast on a solid surface. This layer starts from the stagnant point in the droplet center, and ends to the solid surface. The real flow field in this layer is the result of the rotating flow field overlapping on the average flow field. These two overlaid flow fields result in the final net flow field in the layer close to the solid surface, as shown in Fig. 3-6, red. The layer thickness δ becomes thin with droplet speed increasing (Sikarwar et al., 2010). In this layer, the inertial force (per unit volume) is on the same order of magnitude of viscous force, namely:

$$\frac{\rho u^2}{\Delta y} \sim \mu \frac{u}{\delta^2} \tag{3-13}$$

Therefore, the layer thickness can be expressed as:

$$\delta \sim \frac{\sqrt{r\Delta y}}{\sqrt{Re}} \tag{3-14}$$

where $\sim$ means 'of the order of'. The droplet Reynolds number is defined as $Re = \frac{\rho u r}{\mu}$. The velocity gradient at the solid-liquid interface is approximated in this dissertation:

$$\frac{\partial u}{\partial y} \approx \frac{u}{\delta} = \frac{u\sqrt{Re}}{\sqrt{r\Delta y}} \tag{3-15}$$

Thus, the updating viscous force of the bulk part of droplet is:

$$F_\tau = \mu A \frac{\partial u}{\partial y} = \mu A \frac{u\sqrt{Re}}{\sqrt{r\Delta y}} = \mu u V^{1/3} \sqrt{Re} c_4(\theta_e) \tag{3-16}$$

Substituting the expressions of droplet geometry, i.e. the volume V, area A, radius r and height Δy into the above viscous force F_τ, the coefficient $c_4(\theta_e)$ can be obtained as a function of equilibrium contact angle:

$$c_4(\theta_e) = \frac{A}{V^{1/3}\sqrt{r\Delta y}} = \pi \left(\frac{3}{\pi}\right)^{1/3} \left(\frac{sin^3\theta_e}{2-3\cos\theta_e+\cos^3\theta_e}\right)^{1/2} \left(\frac{2+\cos\theta_e}{1-\cos\theta_e}\right)^{1/6} \tag{3-17}$$

- **Equivalent Marangoni force F_M**

The equivalent Marangoni force F_M acting on the droplet is due to the surface tension gradient, as seen in Fig. 2-7. The basic expression structure of the equivalent Marangoni force is empirically proportional to the product of the change of surface tension $\Delta\sigma_{LG}$ and the force acting distance $k \cdot 2r$. Besides, it indicates in the literature that two Marangoni convections occur inside the droplet advancing and receding part respectively due to the surface tension gradient (Phadnis and Rykaczewski, 2017). The attractive effect (in the droplet moving direction) of advancing sub-convection and the repulsive effect (in the opposite droplet moving direction) of receding sub-convection depend on the dynamic advancing and receding contact angle, respectively. Both of these two effects have the same surface tension change $\Delta\sigma_{LG}$. With respect to the force acting distance, we couple the receding contact angle in the repulsive part as $k \cdot 2r \cdot cos\,\theta_{d,R}$, and the advancing contact angle in the attractive part as $k \cdot 2r \cdot cos\,\theta_{d,A}$. In this dissertation, we combine both the repulsive and the attractive part; therefore, the proposed Marangoni force expression is obtained as follows:

$$F_M = \Delta\sigma_{LG} \cdot \left[k \cdot 2r\left(cos\,\theta_{d,R} - cos\,\theta_{d,A}\right)\right] \tag{3-18}$$

Updating the knowledge of the viscous force F_τ and the equivalent Marangoni force F_M in Eq. (2-20), the droplet velocity depending on droplet size can be derived by the following force balance:

$$\rho V g\,sin\,\alpha = 2kr(\sigma_{LG} + \Delta\sigma_{LG})\left(cos\,\theta_{d,R} - cos\,\theta_{d,A}\right)$$

$$+4\mu u P c_1(\theta_e) ln\left(\frac{L_a}{L_s}\right) + \mu u V^{1/3}\sqrt{Re}\,c_4(\theta_e) \tag{3-19}$$

Compared with the previous model Eq. (2-20), the considered equivalent Marangoni force can be combined with surface tension force, which seems the Marangoni effect modifies the surface tension consequently. If the droplet geometry is not so sensitive to droplet velocity that the dynamic advancing and receding contact angle can be replaced by static advancing and receding contact angle; otherwise the dynamic contact angle model should be adopted. The viscous force F_τ is determined by the velocity gradient with the Re effect.

3.2.2 Transition criterion

The transition from droplet to rivulet is a very complicated process. The surface tension, which makes the droplet acquiring the least surface area, shapes the droplet structure. The moving droplet here is artificially separated into two parts. It is reasonable to assume that there is a pair of action $F_{i,21}$ and reaction $F_{i,12}$ forces acting on the interface between these two parts, as shown in Fig. 3-7. The interface action force can be calculated by, e.g. for droplet part 1,

$$F_{i,21} = F_{g,1}\,sin\,\alpha - F_{\tau,1} - F_{\sigma,1} - F_{M,1} \tag{3-20}$$

$$F_{i,21} = \rho V_1 g\,sin\,\alpha - A_1\mu\frac{\partial u}{\partial y} + 2kr_1(\sigma_{LG} + \Delta\sigma_{LG})\,cos\,\theta_{d,A} \tag{3-21}$$

where the subscript 1 stands for the droplet part 1.

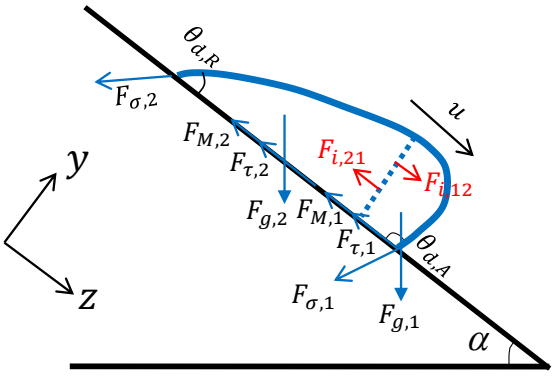

Fig. 3-7 Forces acting on moving droplet at transition point

When the surface tension force at the interface is less than the required action force on the interface, namely, $F_{\sigma,21} < F_{i,21}$, the droplet structure will be stretched, which means the transition from droplet to rivulet starts. The surface tension force is:

$$F_{\sigma,21} = \sigma_{LG} \cdot d_h \tag{3-22}$$

where d_h is the hydraulic diameter of the interface:

$$d_h = 2r\frac{\left(\frac{\theta_e}{sin\,\theta_e} - cos\,\theta_e\right)}{\theta_e + sin\,\theta_e} \tag{3-23}$$

Therefore, the transition droplet size can be obtained by solving the criterion by iteration. For understanding of the transition process, the transition criterion is simplified with assuming the droplet roughly separating into two equal-volume parts and with a circular droplet contour ($k = 1$):

$$\rho\frac{V_t}{2}g\,sin\,\alpha - 2r_t\mu\frac{\partial u}{\partial y} - r_t(\sigma_{LG} + \Delta\sigma_{LG})\,cos\,\theta_e = 2r_t\sigma_{LG}\frac{\left(\frac{\theta_e}{sin\,\theta_e} - cos\,\theta_e\right)}{\theta_e + sin\,\theta_e} \tag{3-24}$$

If the viscous force is neglected further (namely, if surface tension force is much larger than viscous force, $F_{\sigma,1} \gg F_{\tau,1}$), both sides of the equation divided by $\sigma_{LG}{V_t}^{1/3}$ and substituting the droplet structure model in, yields:

$$Bo_t = \frac{\rho {V_t}^{2/3} g\,sin\,\alpha}{\sigma_{LG}} = \frac{4\frac{\left(\frac{\theta_e}{sin\,\theta_e} - cos\,\theta_e\right)}{\theta_e + sin\,\theta_e} + 2\,cos\,\theta_e\left(1 + \frac{\Delta\sigma_{LG}}{\sigma_{LG}}\right)}{\left(\frac{\pi(2 - 3\,cos\,\theta_e + cos^3\theta_e)}{3sin^3\theta_e}\right)^{1/3}} \tag{3-25}$$

Actually the Bond number at the transition point, Bo_t, is under-estimated due to the neglect of the droplet viscous force. The transition size V_t or r_t can be obtained easily by knowing Bo_t. Obviously, the transition point is dependent on the equilibrium contact angle and fluid properties. There is no fixed, constant

value for all kinds of surfaces.

3.3 Condensate coverage

Based on the modelling approach discussed in section 3.1, the total coverage of rivulet and droplet is:

$$\varepsilon = \varepsilon_r + \varepsilon_d \tag{3-26}$$

In the beginning of condensation, there are only droplets on the cold surface. The rivulet coverage is zero. In the droplet and rivulet coexisting phase, the droplet coverage is:

$$\varepsilon_d = (1 - \varepsilon_r) \cdot \varepsilon_{d,t} \tag{3-27}$$

$\varepsilon_{d,t}$ is the droplet coverage at the transition point, which can be obtained by Eq. (3-5), Eq. (3-6), and Eq. (3-7) when the upper limit in the equations is h_t exactly. In steady state, it is acceptable to assume that the droplet coverage in the surface area excluding rivulets, i.e. in the $(1 - \varepsilon_r)$ part in Fig. 3-4, $\varepsilon_{d,t}$ is constant.

Actually, the height h plays a role as an intermediate variable in current modelling approach. Each output parameters (such as condensate volume flow rate per width, condensate coverage, average thickness and average velocity) has a one-to-one relationship with the intermediate variable h. It is clear that after eliminating the intermediate variable the condensate coverage is dependent on condensate volume flow rate per width $\dot{V}$, so that the current modelling approach is feasible to be applied in the containment LP codes.

The modelling approach is programmed (we will continue to discuss it in section 3.4), and the calculation test indicates the consuming time is a few tens of second per boundary condition. It is not acceptable for LP containment codes, especially when the code is calculating a transient problem. In addition, the robustness of the containment code coupling the condensate flow model should also be considered. Therefore, a simplified model of condensate coverage is necessary for the implementation in the LP containment codes.

- **Dimensionless parameters**

For the dimensional analysis, the Buckingham π theorem is applied to reduce the physical problem to the simplest (most economical) form (Bridgman, 1931; Buckingham, 1914). The first and most important step in the dimensional analysis is to identify a complete set of independent quantities. One known is that the condensate coverage ε on the inclined wall depends on the independent quantities, such as volume flow rate per width $\dot{V}$, equilibrium contact angle θ_e, inclination angle α, gravitation g, fluid density ρ, fluid dynamic viscosity μ and surface tension σ_{LG}, namely,

$$\varepsilon = f\left(\dot{V}, \theta_e, \alpha, g, \rho, \mu, \sigma_{LG}\right) \tag{3-28}$$

This expression can be rewritten as a dimensionless form. The number of dimensionless parameters is equal to the total number of variables minus the number of the physical dimensions involved. For the interested physical quantities of condensate coverage, three involved basic dimensions, which are length [m], time [s], and mass [kg], are usually taken into account. All physical quantities have dimensions, which can be expressed as products of powers of these three basic dimensions. We now can define the dimensionless form with 5 (i.e. 8 – 3 = 5, 5 π terms) dimensionless numbers accordingly:

$$f(\pi_1, \pi_2, \pi_3, \pi_4, \pi_5) = 0 \tag{3-29}$$

Since the coverage ε, the equilibrium contact angle θ_e, and the inclination angle α are already dimensionless numbers, the remaining 5 quantities ($\dot{V}$, g, ρ, μ and σ_{LG}) can yield the other two dimensionless numbers. These 5 quantities are combined and arranged, in sequence, to find the last two π terms in the simplest dimensionless forms:

$$\pi_1 = \frac{\rho \dot{V}}{\mu} \tag{3-30}$$

$$\pi_2 = \sigma_{LG} \left(\frac{\rho}{g\mu^4}\right)^{\frac{1}{3}} \tag{3-31}$$

π_1 times a factor 4 is the Reynolds number $Re = \frac{4\rho\dot{V}}{\mu}$, and π_2 is exactly the Kapitza number $Ka = \sigma_{LG}\left(\frac{\rho}{g\mu^4}\right)^{1/3}$. The equilibrium contact angle θ_e and inclination α physically influence the surface tension force and gravitation in the forms of $(1 - cos\theta_e)$ and $sin\alpha$ respectively. Therefore, the coverage ε can be expressed ultimately as a relationship among all of the π terms:

$$\varepsilon = f(Re, Ka, 1 - cos\theta_e, sin\alpha) \tag{3-32}$$

- **Empirical correlation**

According to the modelling approach discussed in section 3.1, the condensate coverage definition can be expressed as the ratio of volume flow rate per width to the average velocity and thickness of condensate. It is no doubt that the flow patterns of condensate have three phases as discussed before, i.e., the moving droplets, rivulets and fully covered film. For the fully covered film, the coverage $\varepsilon = 1$ and the film velocity and thickness can be obtained by the film model (see the literature review section 2.2.4). In case of moving droplets, the velocity distribution depends on droplet size, so that only a part of droplets is effective for aerosol wash-down. The rivulet velocity is much higher than the velocity of moving droplets. Therefore, the rivulet flow pattern is supposed here to dominate the coverage when the wall is not fully covered by film.

The minimum total energy (MTE) method is widely examined for determining the thickness of a rivulet flowing down a sloped wall. In previous researches (Hartley and Murgatroyd, 1964; Hobler, 1964; Doniec, 1988, 1991; El-Genk and Saber, 2001; Huang and Cheng, 2014), analytical expressions of velocity and structure of a stable rivulet are developed. These are summarized in the literature review section 2.2.3. The empirical rivulet thickness correlation is derived with prefactor c_δ in the range of (1.125-1.86). The average rivulet velocity is obtained with the parabolic distribution from the wall to the rivulet interface with gas (El-Genk and Saber, 2001). The previous research (Huang and Cheng, 2014) reveals that the main part of rivulet is a rectangular film sheet with a constant thickness. The rivulet average thickness and velocity change slightly while the rivulet width varies with the condensate flow rate. Compared with the main part of the rivulet, the proportion of the arc parts of rivulet edges are very small. Substituting the rivulet average thickness and velocity into the coverage definition in order to approximate the condensate coverage, one can be derived as follows:

$$\varepsilon = \frac{\dot{V}}{\bar{u}\cdot\bar{\delta}} = \frac{\dot{V}}{\frac{\rho g sin\alpha}{3\mu}\bar{\delta}^3} = \frac{\dot{V}}{\frac{\rho g sin\alpha}{3\mu}\left(c_\delta\cdot(1-cos\theta_e)^{0.2}\left(\frac{\mu^2\sigma_{LG}}{\rho^3(gsin\alpha)^2}\right)^{0.2}\right)^3}$$

$$= \frac{0.75}{c_\delta^3}\cdot\frac{4\rho\dot{V}}{\mu}\left(\sigma_{LG}\left(\frac{\rho}{g\mu^4}\right)^{\frac{1}{3}}\right)^{-0.6}(1-cos\theta_e)^{-0.6}(sin\alpha)^{0.2} \quad (3\text{-}33)$$

Substituting all the dimensionless numbers (as presented in Eq. (3-32)) into above equation:

$$\varepsilon = \frac{0.75}{c_\delta^3}\cdot Re^1 Ka^{-0.6}(1-cos\theta_e)^{-0.6}(sin\alpha)^{0.2} \quad (3\text{-}34)$$

Due to $c_\delta \in (1.125,1.86)$, the prefactor $\frac{0.75}{c_\delta^3} \in (0.12,0.52)$ accordingly, which should be determined further. The valid parameter ranges of the condensate coverage correlation are as follows: the Kapitza number $Ka \in (2500,22500)$, which depends on the condensate temperature and pressure inside the containment. The equilibrium contact angle $\theta_e \in (0°, 90°)$, excluding the cases of $0°$ and $90°$. The wall inclination $\alpha \in (0°, 90°]$, excluding the horizontal surface but including the vertical. The Reynolds number is from zero to the maximum value (when the coverage equals one).

3.4 **Analysis of condensation process**

In this section, the developed modelling approach is applied to analyze the condensate flow behavior under typical containment conditions. The static

advancing and receding contact angles are 71.8° and 18.4° respectively, which are the measured experimental data of water on a dry containment paint (Inorganic zinc coating) coated stainless steel. The inclination angle $\alpha = 90°$ for a vertical wall. The condensation heat flux is given as 50 kW/m^2 (actually the condensation heat flux range in containment is about 1-100 kW/m^2 during accidents (de la Rosa et al., 2009)). The atmosphere pressure and condensate temperature are assumed to be 4 bar and 90℃ respectively, in order to obtain the fluid properties. The temperature difference between bulk and solid cold surface is in range 10-60℃ (Herranz et al., 1998). The average temperature difference 35℃ is adopted to calculate the equivalent Marangoni effect on surface tension. These above contact angles, wall inclination, condensation heat flux and fluid properties, are only given for model testing.

The numerical solution of the droplet and rivulet volume, wetting area, velocity and thickness along the wall height are shown in Fig. 3-8. The condensate (droplet and rivulet) volume increases monotonously with the moving distance. It is continuous no matter before or after the transition occurs. However, the slope of this curve changes with the flow patterns due to the alteration of wetting area and velocity.

During the droplet moving phase, the velocity, wetting area and thickness increase with droplet volume, as well as these quantities in the rivulet phase. However, the velocity, wetting area and thickness have a step change at the transition point, due to the difference of geometry and velocity between droplet and rivulet. The droplet wetting area and velocity are much smaller than those of rivulet, but the thickness is on the contrary. In addition, the velocity and thickness of the rivulet in the beginning increase slightly and later both of them are stable. Since the rivulet width spreads with the increase of condensate volume continuously, and a rectangular film sheet forms in the middle with a fixed thickness calculated by MTE method. That means the impact of the two arc parts of the rivulet becomes less when the rectangular film sheet becomes wider.

Based on the above microscopic treatment results, and according to our macroscopic treatment, the volume flow rate per width, average thickness, average velocity, and condensate coverage are all obtained as a function of height h, as shown in Fig. 3-9 respectively. The volume flow rate per width increases over the moving distance, since the total number (integral along height) of droplets and rivulets increase, as long as the initiation density $n_d \geq 0$ (which is true according to non-zero condensation heat flux).

The average thickness and velocity change much when the transition happens, since the thickness, velocity models vary dramatically after transition. Before transition, all the condensate are droplets, after the transition the condensate consists of droplets and rivulets. Therefore, the coverage curve is continuous at the transition point but the slope changes. During the coexisting phase, more and more droplets transform to rivulets with the condensate increasing.

Meanwhile, the proportion of droplet coverage to the whole coverage becomes less and less, and then the rivulet pattern dominates the condensate flow in the late coexisting phase.

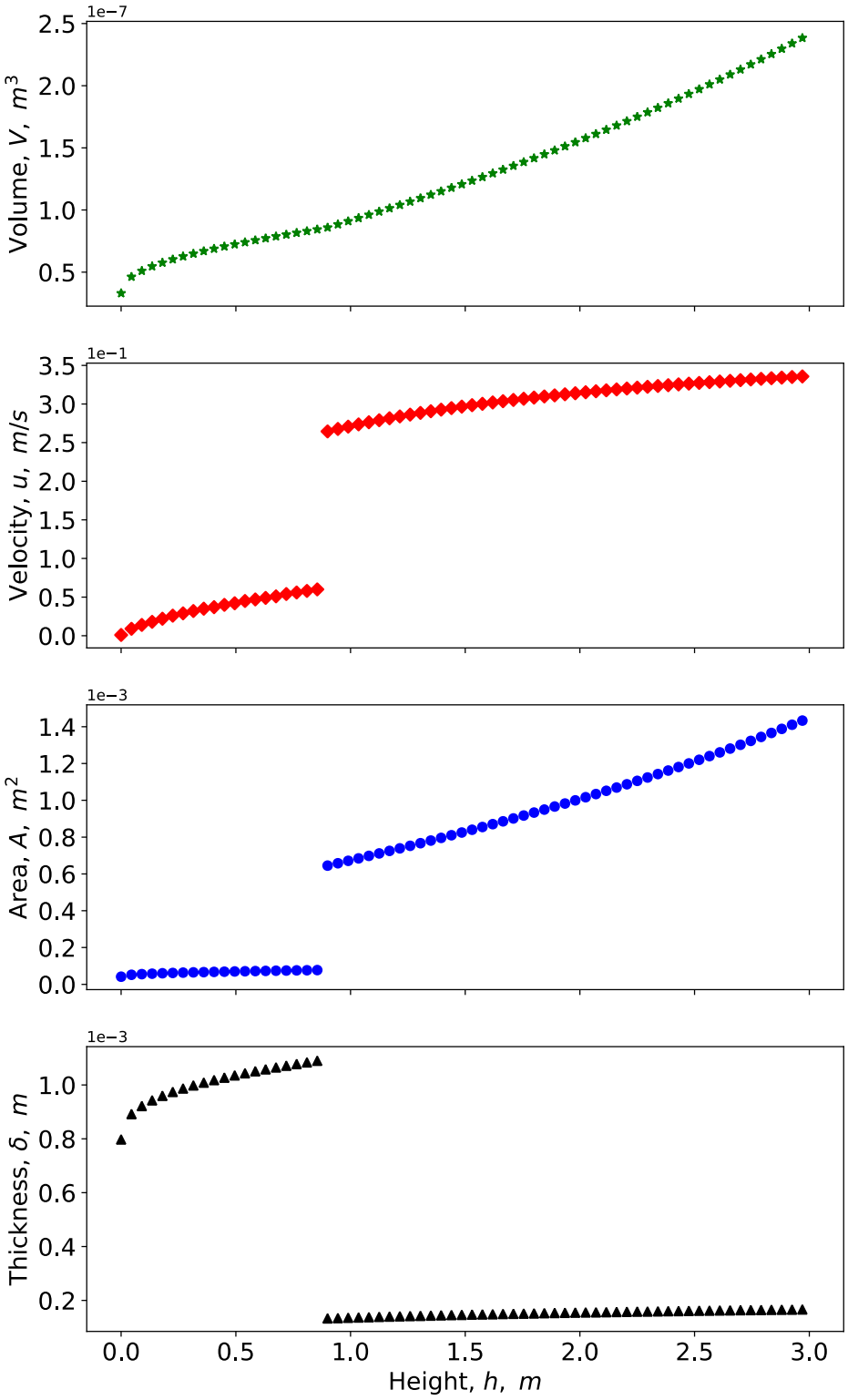

Fig. 3-8 Microscopic treatment results for one single trace

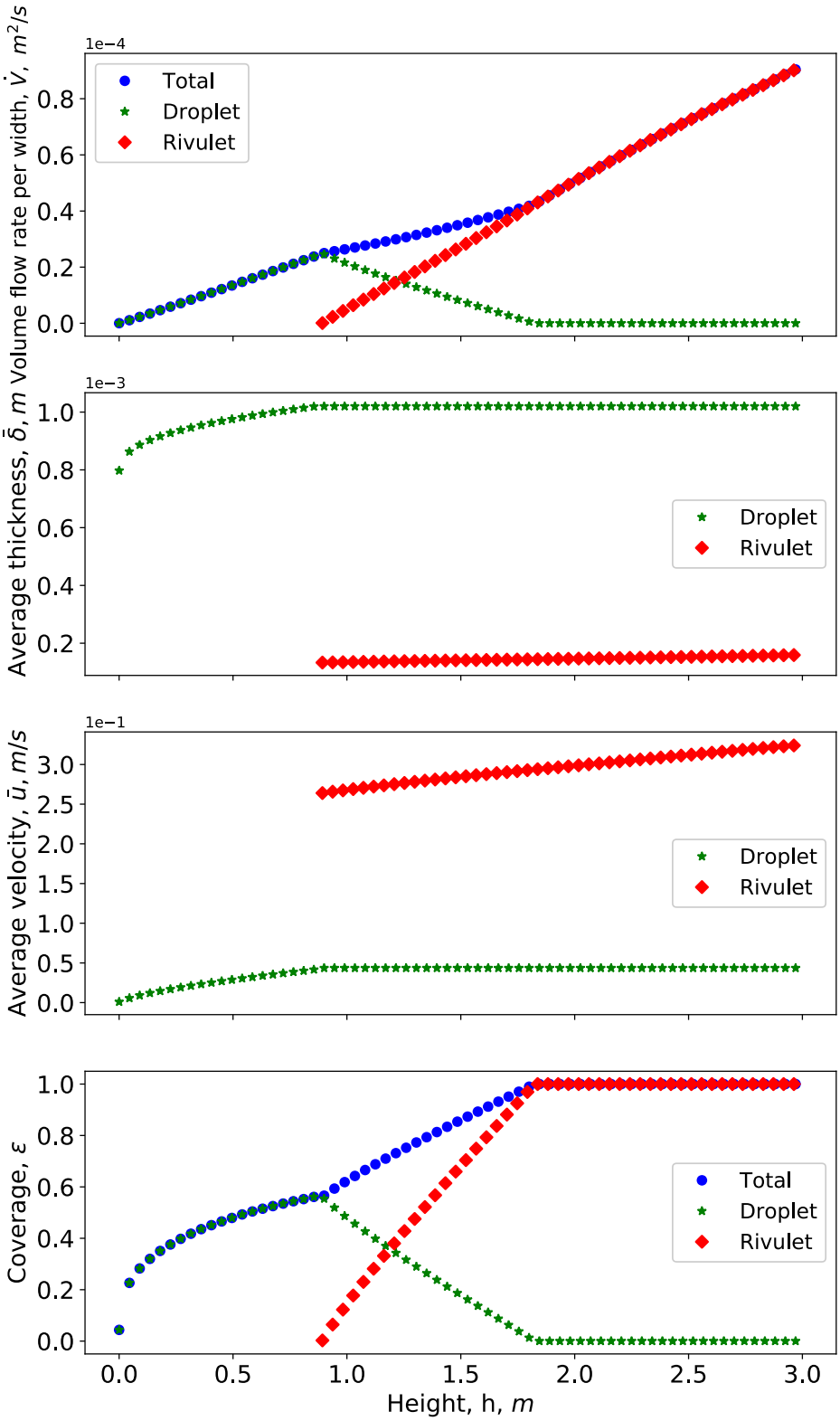

Fig. 3-9 Macroscopic treatment results for the integral effect

Calculation B.C. of Fig. 3-8 and Fig. 3-9: $\theta_{s,A}/\theta_{s,R} = 71.8°/18.4°$, inclination angle $\alpha = 90°$, condensation heat flux $q = 50\ \mathrm{kW/m^2}$, pressure $p = 4\ \mathrm{bar}$, temperature $T = 90℃$, temperature difference $\Delta T = 35℃$

Concerning the model implementation in containment codes, probably the volume flow rate per width, contact angles, wall inclination and fluid properties are known as input parameters for condensate coverage calculation. From the macroscopic results, both the volume flow rate per width and the coverage have one-to-one relationship with height h. If the intermediate variable h is eliminated, the function between coverage (dependent variable) and volume flow rate per width (independent variable) is obtained as shown in Fig. 3-10 (the blue dot is the total coverage). In the same way, the average thickness and velocity, which are in terms of volume flow rate per width, contact angles, wall inclination and fluid properties, can be also obtained by the current modelling approach.

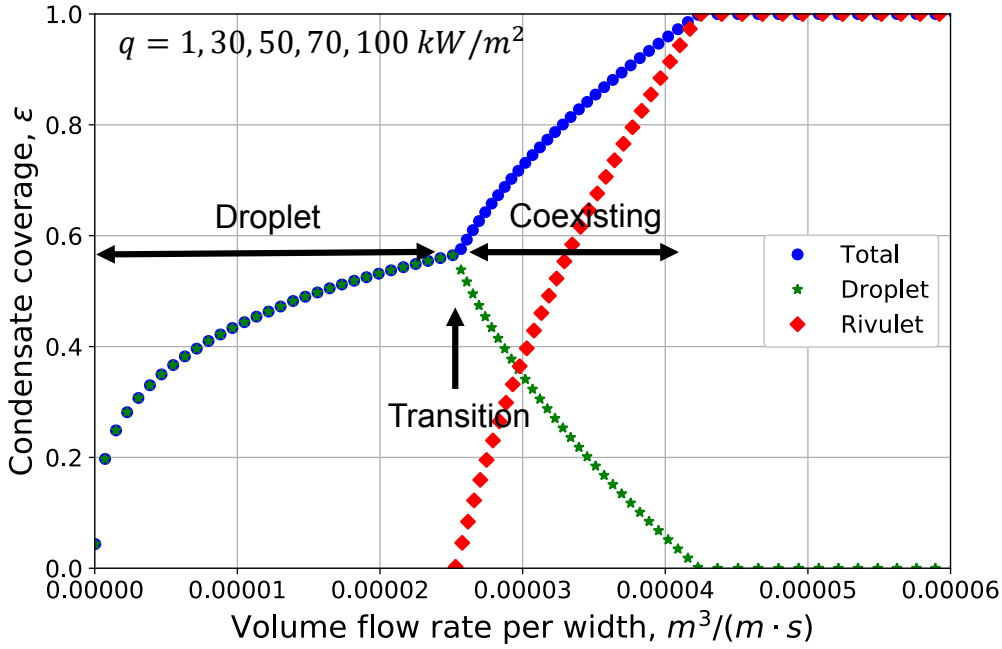

Fig. 3-10 Condensate coverage versus volume flow rate per width

The condensate coverage alters much when the transition occurs, as seen in Fig. 3-10. The coverage rises moderately during the droplet phase, then increasing gradient changes much after transition. Later the coverage climbs continuously during the coexisting phase. From the transition criterion, the size of droplet V_t and r_t are known for given contact angles, wall inclination and fluid properties. Moreover, based on the microscopic treatment, the critical height h_t are known by Eq. (3-1). Therefore, the critical volume flow rate per width is:

$$\dot{V}_t = \int_0^{h_t} V(h - z) n_d \mathrm{d}z \tag{3-35}$$

The condensate coverage does not change under different condensation heat fluxes, as shown in Fig. 3-10. It is obvious that the coverage, as well as the

volume flow rate per width, will increase at a certain height with the condensation heat flux increasing. However, the condensation heat flux seems to have no effect on the relationship between the coverage and volume flow rate per width. That is because the volume flow rate per width is the integral of the condensation heat flux along height, as expressed in Eq. (3-4). In other words, the volume flow rate per width has already included the effect of condensation heat flux.

3.5 Extension of aerosol wash-down model

In this section, the aerosol wash-down model will be extended with the consideration of inclination angle and particle cohesion effects based on the forces acting on the particle.

Let us consider a particle located at the water-particle interface as presented in Fig. 3-11. The water-particle interface is assumed to be sloped with an inclination angle α. Its stability is characterized by the balance between the following forces: (1) the buoyant weight (i.e. the gravitation minus the buoyance) of the particle F_W, which is perpendicular to the ground without inclination, (2) the drag force of the overlying flow F_D, which is caused by the flow shear stress, and parallel to the inclined surface or the flow direction, (3) the effective cohesive force F_C, which is perpendicular to the wall surface, (4) the lift force of the overlying flow F_L, and (5) the friction force F_F of the particle in the first layer.

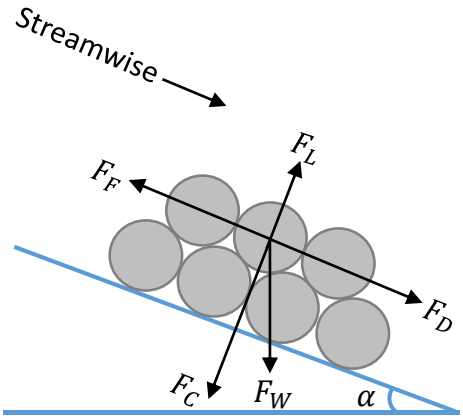

Fig. 3-11 Forces acting on a particle located at the water-particle interface

The buoyant weight component $F_W cos\alpha$, F_C and F_L are perpendicular to the surface, so that the friction force paralleled to surface is:

$$F_F = \mu_c(F_W cos\alpha + F_C - F_L) \tag{3-36}$$

where μ_c is the Coulomb friction coefficient. The erosion criterion comes from the particle movement initiation, which fulfill the balance of all external forces in the flow direction:

$$F_D + F_W sin\alpha = \mu_c(F_W cos\alpha + F_C - F_L) \quad (3\text{-}37)$$

Arranging and combining the like terms:

$$F_D + \mu_c F_L = \mu_c F_W \left(cos\alpha - \frac{sin\alpha}{\mu_c} + \frac{F_C}{F_W}\right) \quad (3\text{-}38)$$

All the forces' expressions are (Ternat, 2008):

$$F_W = k_W g(s-1)\rho d_p^3 \quad (3\text{-}39)$$

$$F_D = k_{D,1}\rho u^2 Re^{*2}\left(1 + k_{D,2}Re^{*2}\right) \quad (3\text{-}40)$$

$$F_L = k_L \rho u^2 Re^{*3} \quad (3\text{-}41)$$

$$F_C = \frac{A_H(1-cos\alpha_c)}{48K(n)^2 d_p} \quad (3\text{-}42)$$

where k_W, $k_{D,1}$, $k_{D,2}$, k_L all are the constant factors of forces' expressions and the particle Reynolds number $Re^* = \frac{u_c^* d_p}{\nu}$. For a spherical particle $k_W = \frac{\pi}{6}$. $k_{D,1}$ and $k_{D,2}$ are the drag force factor related to particle shape and the factor characterizing the burying of the particle with respect to the mean height of sediment bed respectively. k_L is the factor coupling the lift force coefficient.

The cohesive force between particles F_C is assumed as the interaction between particles without the influence of the size distribution (Ternat, 2008). $A_H \cong 10^{-20}$ Joule is the Hamaker constant. α_c is the critical inclination angle, whose tangent is the coefficient of sliding friction. The compaction function $K(n)$ is defined by:

$$K(n) = \left(\frac{n_{max} - n_{min}}{n_{max} - n}\right)^{\frac{1}{3}} - 1 \quad (3\text{-}43)$$

where n is the local porosity of particles. In practice the maximum porosity $n_{max} = 1$. The minimum porosity n_{min} depends on the compact structure (namely the packing arrangement as cubic, hexagonal, etc.). In current case, the cubic compact structure is preferred due to the low compactness of nuclear aerosols (Freitag et al., 2016), which presents $n_{min} = 1 - \frac{\pi}{6}$.

Substituting the forces' expressions into the force balance Eq. (3-37), yields:

$$k_{D,1}\rho u^2 Re^{*2}\left(1 + k_{D,2}Re^{*2}\right) + \mu_c k_L \rho u^2 Re^{*3}$$

$$= \mu_c k_W g(s-1)\rho d_p^3 \left(cos\alpha - \frac{sin\alpha}{\mu_c} + \frac{F_C}{F_W}\right) \quad (3\text{-}44)$$

Rearranging the above equation:

$$\frac{u^2 Re^{*2}}{g(s-1)d_p^3} = \frac{\mu_c k_W}{k_{D,1}\left(1 + k_{D,2}Re^{*2}\right) + \mu_c k_L Re^*}\left(cos\alpha - \frac{sin\alpha}{\mu_c} + \frac{F_C}{F_W}\right) \quad (3\text{-}45)$$

Substituting the critical shear stress $\tau_c = \rho u_c^{*2}$ and the particle Reynolds number $Re^* = \frac{u_c^* d_p}{\nu}$ into the definition of critical Shields parameter:

$$\tau_c^* = \frac{\tau_c}{g\rho(s-1)d_p} = \frac{u^2 Re^{*2}}{g(s-1)d_p^3} \tag{3-46}$$

Hence, comparing with the rearranged force balance Eq. (3-44), the critical Shields parameter Eq. (3-45):

$$\tau_c^* = \frac{\mu_c k_W}{k_{D,1}\left(1+k_{D,2}Re^{*2}\right)+\mu_c k_L Re^*}\left(cos\alpha - \frac{sin\alpha}{\mu_c} + \frac{F_C}{F_W}\right) \tag{3-47}$$

For the horizontal surface and non-cohesive particles, namely $\left(cos\alpha - \frac{sin\alpha}{\mu_c} + \frac{F_C}{F_W}\right) = 1$, the dimensionless critical shear stress for horizontal non-cohesive particle bed is:

$$\tau_{c,o}^* = \frac{\mu_c k_W}{k_{D,1}\left(1+k_{D,2}Re^{*2}\right)+\mu_c k_L Re^*} \tag{3-48}$$

which is exactly the same expression resulted in reference (Ternat, 2008). However, the empirical expression (Guo, 2002) of $\tau_{c,o}^*$ is adopted in AULA as well as quoted in (Weber et al., 2015). In order to avoid determining the related constants, the derived $\tau_{c,o}^*$ Eq. (3-48) is not used directly. On the contrary, it is preferred to apply the empirical correlation of $\tau_{c,o}^*$ Eq. (2-6), since the empirical expression of $\tau_{c,o}^*$ is validated widely against experimental data (Guo, 2002). Therefore, the modified dimensionless critical shear stress is proposed in a short form as:

$$\tau_c^* = C_{i,c} \cdot \tau_{c,o}^* \tag{3-49}$$

where the combined correction factor of inclination and cohesion effects is:

$$C_{i,c} = \left(cos\alpha - \frac{sin\alpha}{\mu_c} + \frac{F_c}{F_w}\right) \tag{3-50}$$

3.5.1 Surface inclination effect

In the case of non-cohesive particles (or the particle size is very large, the cohesive force can be neglected comparing with the buoyant weight), the modification of dimensionless critical shear stress with the consideration of inclination but without cohesion is:

$$\tau_c^* = \tau_{c,o}^* \left(cos\alpha - \frac{sin\alpha}{\mu_c}\right) \tag{3-51}$$

which is consistent with the result in the literature (Dey and Papanicolaou, 2008). Since the cohesive force is ignored, which means that all particles are

balanced by the gravitational force, the friction, the lift force and the drag force. When it comes to a critical case, namely the inclination angle is larger than the threshold angle α_c, the particle will slide downwards automatically even without the driving of drag force. The Coulomb friction coefficient of natural sediments is recommended as $\mu_c = 0.58 - 0.84$. The mean value $\mu_c = 0.7$ and the friction coefficient is known as $\mu_c = tan\alpha_c$, hence the estimated critical inclination angle of natural sediments $\alpha_c = 35°$.

The result of inclination correction factor $\left(cos\alpha - \frac{sin\alpha}{\mu_c}\right)$ versus wall inclination is shown in Fig. 3-12. The inclination correction factor decreases with the inclination angle increasing. When $\left(cos\alpha - \frac{sin\alpha}{\mu_c}\right) = 0$, the inclination reaches its threshold. That means the particle will move downwards even without the drag force of the flow. If the inclination increases further, the quantity decreases from positive to negative value, which means the driving force is always beyond the resistance. The particles slide downwards automatically if there is no cohesion to compensate.

If the inclination already exceeds its critical inclination angle α_c, but the force ratio $\frac{F_C}{F_W} \geq \frac{sin\alpha}{\mu_c} - cos\alpha$, then the particles can also be still on the surface. In this case, the requirements of particle properties (such as minimum particle size and porosity) can be determined based on the known inclination angle.

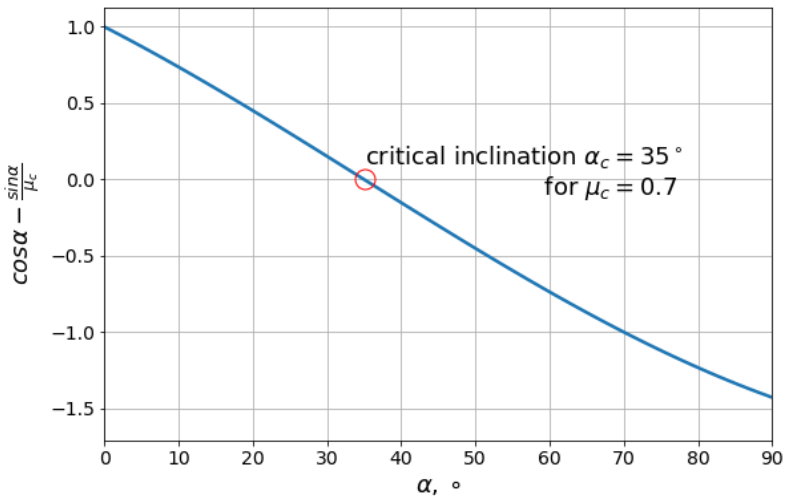

Fig. 3-12 Effect of inclination angle

The inclination effect on the aerosol wash-down model under typical severe accident conditions is of interest. The typical thermal-hydraulic conditions in containment are similar to the case applied in the section 3.4: the atmosphere pressure and water temperature are assumed 4 bar and 90℃ respectively in order to obtain the fluid properties. The experimental measured equilibrium contact angle $\theta_e = 62.5°$. Based on the knowledge of the THAI-AW3-LAB experiment, some other parameters' ranges can be defined, such as, the

particle diameter $d_p \in [0.25, 2.5]$ μm, the effective particle density $\rho_p = 1550$ kg/m^3, and the inclination angle $\alpha \in [2°,\ 90°]$. The erosion constant $k_{e,0} = 0.03$ 1/s, the aerosol porosity $n = 0.9$, and the aerosol surface load $c_{ae,0} = 0.027$ kg/m^2. The mass flow rate 0.03 kg/s (should make sure it is a rivulet case, not a fully covered film case). The surface geometry is: wide x high = 1 m x 1 m.

The inclination impact not only on the critical shear velocity u_c^* determined by particles, but also on the rivulet shear velocity u^*. Fig. 3-13 shows the variation of both u_c^* and u^* with the inclination increasing under the typical SA conditions. The rivulet shear velocity increases with inclination, since the rivulet model tells the rivulet velocity is proportional to $sin\alpha^{0.2}$, and the rivulet shear velocity has the same monotonicity of rivulet velocity. However, the critical shear velocity u_c^* decreases with the inclination increasing, because of the negative inclination effect. Accordingly, it is possible to find the cross point between the two curves for a specific particle diameter, for instance as shown in Fig. 3-13, the intersection between the blue dot curve and the green star one. That means there is no aerosol wash-down when the inclination is less than the cross point (~20° for the current case). Consequently, the erosion rate equals zero, as shown in Fig. 3-14.

Moreover, we can also define the boundary of the particle diameter. As shown in Fig. 3-13, no matter how large the inclination is, if the particle diameter is less than 0.21 μm, there is no wash-down anymore, while if the particle diameter is larger than 0.36 μm there is always wash-down under the current conditions. Fig. 3-14 also indicates the rivulet coverage and the erosion rate increase with the surface inclination, as a result, the aerosol wash-down efficiency increases with inclination angle.

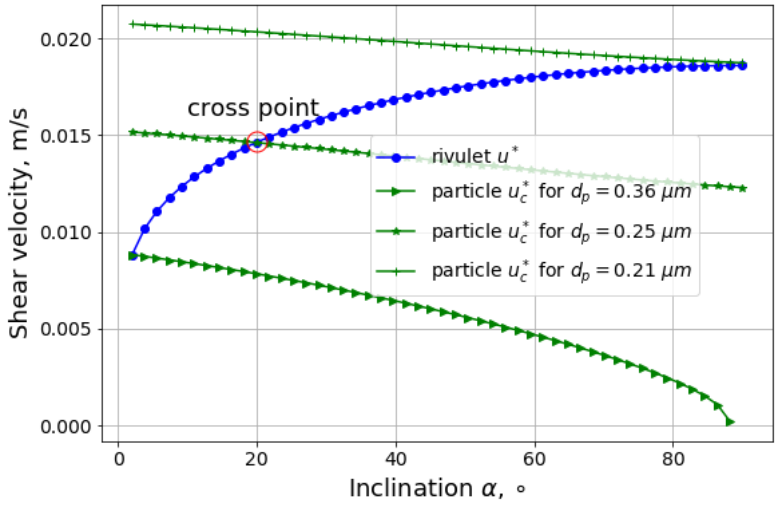

Fig. 3-13 Shear velocity versus surface inclination

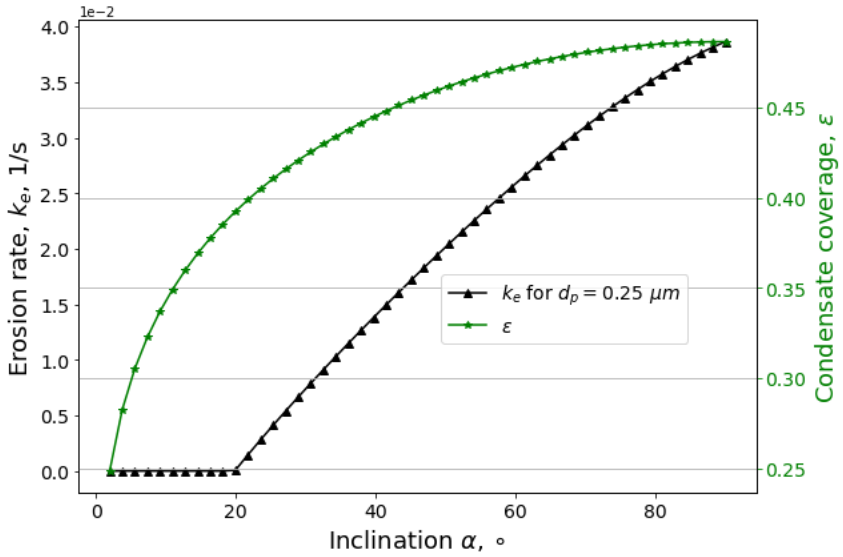

Fig. 3-14 Erosion rate and condensate coverage versus inclination

3.5.2 Particle cohesion effect

The nuclear aerosols deposited on walls are with very various and complicated components, size distribution, porosity, etc. In the THAI aerosol wash-down experiments, the aerosols can be loaded on vertical walls. Accordingly, the cohesive force acting on particles cannot be ignored. Otherwise, when the gravitational force overcomes the friction, the particles would slide downwards naturally. The consequence of the cohesion effect increases the velocity needed for initiation of particle movement. An additional friction comes out when cohesive effect is considered in the force balance.

THAI-AW3-LAB experiment reports that the bulk density of silver aerosol is 1100 kg/m^3. The bulk density of silver powder is the ratio of the weight of silver powder to the volume of both silver particles and the void space between the silver particles. The silver material density is 10490 kg/m^3. The silver material density is not mentioned in THAI-AW3-LAB report actually, but presented in the report of the companion experiment THAI-AW3 (part 1) (Freitag et al., 2016). Therefore, the silver porosity n can be approximated as:

$$n = 1 - \frac{bulk\ density}{material\ density} \tag{3-52}$$

So $n = 1 - \frac{1100}{10490} \cong 0.9$. The particle porosity is high, namely the particle compactness is low. According to the opinion of (Ternat, 2008), the cohesive force of particles with high porosity can be assumed as the interaction between the same size particles, without the influence of the size distribution. Based on the expressions of cohesive force Eq. (3-42) and buoyant weight Eq. (3-39), the

curves of the force ratio $\frac{F_C}{F_W}$, as shown in Fig. 3-15, are plotted against particle size with different porosity n. The boundary condition is in Table 3-1.

Table 3-1 Parameters for the cohesive force model

ρ_p kg/m^3	ρ kg/m^3	g m/s^2	n_{max}	n_{min}	A_H Joule	α_c °	k_W
1550	1000	9.8	1	$1-\frac{\pi}{6}$	10^{-20}	35	$\frac{\pi}{6}$

Fig. 3-15 reveals that increasing the porosity leads to the decrease of cohesive force obviously. The cohesive force can be neglected if particle size is quite big. The mean particle diameter used in THAI-AW3-LAB experiments are in the size range 0.7-2.5 μm. In most cases, the cohesive force is comparable to the buoyant weight. However, when the porosity $n = 0.9$, the cohesive force is less than the buoyant weight for the experimental particle size in THAI-AW3-LAB. Nevertheless, partial particles are still on vertical walls in the integral THAI-AW3 experiment. It is possible that the porosity is overestimated. The bulk density of silver powder is quite smaller than the silver material density. It is likely that the bulk density of deposited aerosols would be larger in reality. The larger bulk density is, the more compact the silver particles are. That leads to the smaller porosity n and larger cohesive force accordingly. Another reason is the diameter of the deposited aerosols on vertical walls could be smaller than the mean particle size, since the particle size has a log-normal distribution. The small particles (less than the average size) with high cohesion can be still on the wall with a high inclination angle.

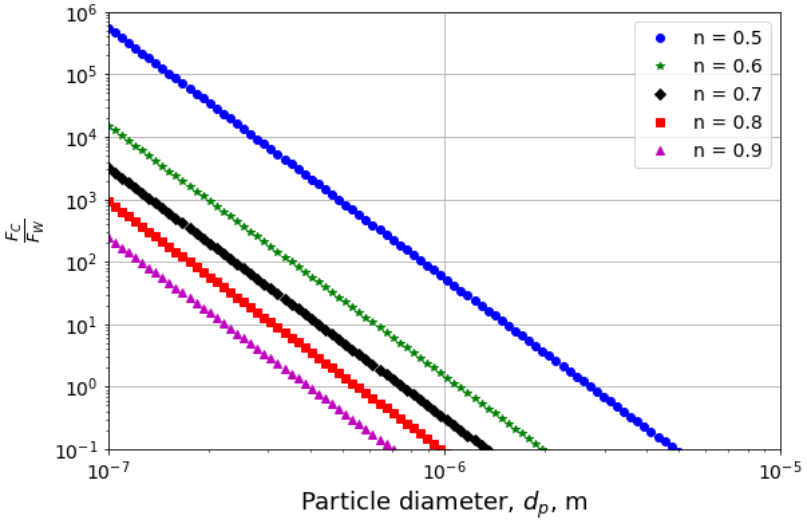

Fig. 3-15 Force ratio versus particle size with different porosities

The particle cohesion affects the aerosol wash-down threshold very much since the critical shear velocity is a function of particle cohesion. Fig. 3-16 shows the curves of the critical dimensionless shear stress τ_c^* and critical shear velocity

u_c^* versus particle porosity under the typical SA conditions and $d_p = 1$ μm, $\alpha = 30°$ specifically. Both τ_c^* and u_c^* decrease rapidly with particle porosity increasing, where the particle porosity is less than 0.6. The τ_c^* and u_c^* are kept almost flat while the particle porosity increases further (larger than 0.75). That is because the cohesive force decreases exponentially with the particle porosity increasing, as shown in Fig. 3-15. Consequently, the erosion rate k_e of aerosol wash-down on the water-covered wall with respect to different particle porosity, as shown in Fig. 3-17, reveals that there is no wash-down when $n \leq 0.53$ and the aerosol wash-down efficiency increases with the aerosol porosity increasing due to the corresponding decrease of τ_c^* and u_c^*.

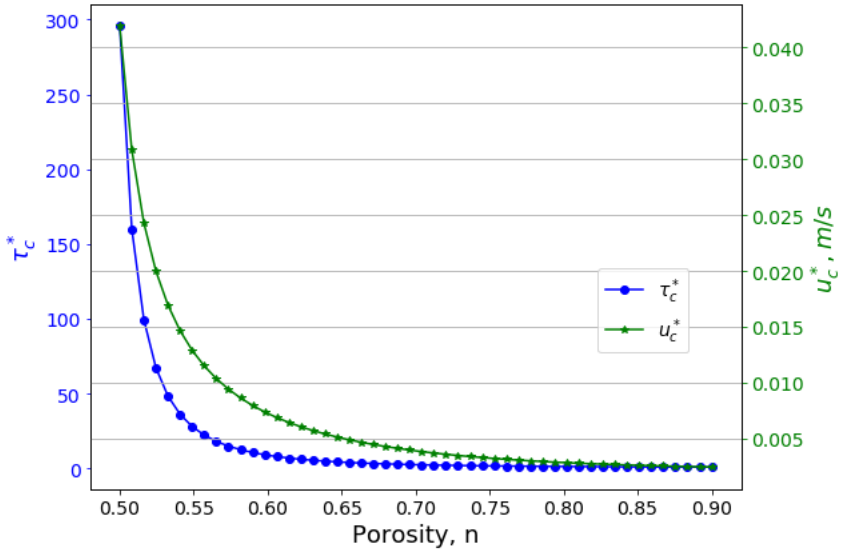

Fig. 3-16 Critical dimensionless shear stress and critical shear velocity versus particle porosity

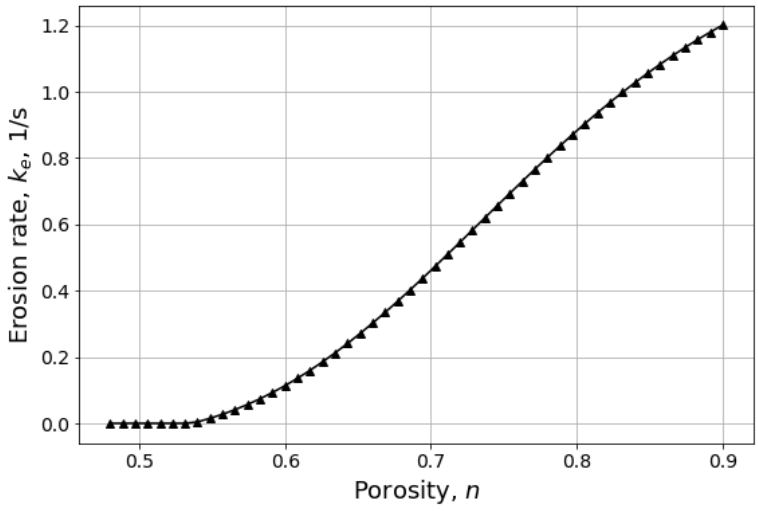

Fig. 3-17 Erosion rate versus particle porosity

4 MODEL VALIDATION

Model validation is defined as the processes intended to verify that the developed models, e.g. the condensate flow models, are performing as expected in line with the objectives, and identify the potential limitations.

The velocity model of droplet moving down on inclined surface at high Re, is validated against experiment, as well as the newly developed criterion of the transition from droplet to rivulet on the containment structure surface. The condensate coverage model is developed by considering the condensate flow patterns. The prediction by the proposed coverage model (including the empirical correlation) is highly relevant to be compared with the experimental data as well.

The extension of the existing aerosol wash-down model AULA by considering the effects of wall inclination and aerosol cohesion and its coupling with the coverage correlation, will also be validated by both the laboratory scaling experiment THAI-AW3-LAB and the integral experiment THAI-AW3.

The items of model validation are briefly summarized as follows:

- Droplet velocity model
- Criterion of the transition from droplet to rivulet
- Condensate coverage model (including correlation)
- Extended aerosol wash-down model

4.1 Droplet characteristics

In order to validate the improved velocity model of moving droplet, as well as to investigate the dynamic contact angle hysteresis of water droplet moving on a typical containment structure surface and the transition from droplet to rivulet, new fundamental experiments are carried out.

4.1.1 Experiment setup

A fundamental experiment study on water droplet motion is conducted. The velocity, shape and the dynamic contact angles of moving droplets are measured via the videos recorded during the tests. The experiment device so-called DRISE (Drop and Rivulet on Inclined Surface Experiment) is set up by stainless steel plate coated with InOrganic Zinc-rich paint (IOZ, a decontamination paint used in containment shell surface), with a fixed dimension (length 85 cm × width 18.3 cm × thickness 1 cm) but with three various slope angles (32.5°, 60.9°, 83.3°). The experiment schematic is shown in Fig. 4-1. In order to change the slope angle of the plate, the upper end is supported by a pedestal of adjustable height.

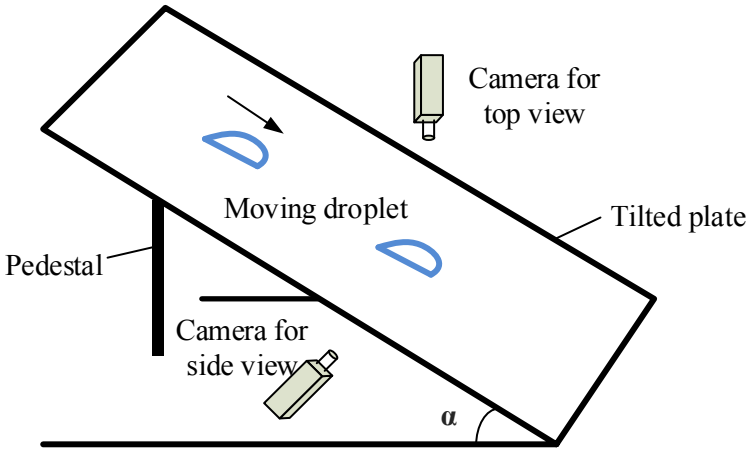

Fig. 4-1 Experimental schematic of droplet motion on tilted plate

Before the experiment, the IOZ coated steel plate is cleaned with water then dried to make it as homogeneous as possible. Water droplets are generated from a burette (Eppendorf Research plus) onto the inclined plate. The volume range of the burette is 0.1-200.0 μL (error is ± 0.05 μL). The size of droplet selected depends on the experimental requirement and the repeatability of the droplet generated stably. A digital high-speed camera (MEMRECAM, IMAGE TECHNOLOGY) is used to visualize the side view of the droplets in sync at 100-10000 fps with a LED light source, while another camera recorded the top view videos at 120/240 fps, as shown in Fig. 4-1. The quantity of frames determines the camera recording time (almost 6-60 seconds), because the

memory of the MEMRECAM camera is fixed at 8 Gigabytes. GXlink software connects the camera and the computer for the post-process of the videos. A ruler with minimum scale 0.5 mm is fixed on the area where the camera captures photos, which is an assistant to measure the velocity and the size of droplets. The properties, such as surface tension, viscosity and density are strongly dependent on the water temperature. In present experiments the water temperature is about 20-23℃.

- **Experiments Matrix**

An overview of the parameters and test conditions is given in Table 4-1. $Ca = \mu u/\sigma_{LG}$ is the droplet capillary number with u being the droplet velocity, μ being the dynamic viscosity, and σ_{LG} being the surface tension of the water in the air. The Reynolds number $Re = \rho ur/\mu$ where r is droplet wetting area radius. The fluid properties at mean room temperature 21.5℃: surface tension σ_{LG}, 0.073 N/m; dynamic viscosity μ, 0.966 * 10^{-3} Pa*s; density ρ, 997.8 kg/m^3.

Table 4-1 DRISE experiment campaign

V, μL	u, cm/s	$\theta_{d,A}$, °	$\theta_{d,R}$, °	Ca, 10^{-3}	Re	Data points
71.3-125.3	0.3-18	78-158	4-18	0.06-1.84	56-1700	8

- **Main Measurements**

The slope angle of the steel plate from the horizontal is measured by a digital angle-measuring device with error less than 0.1°. Water droplet volume can be obtained by the droplet generator burette. Water temperature (here is the mean temperature of water surface and the inclined solid surface) is measured by infrared temperature gun.

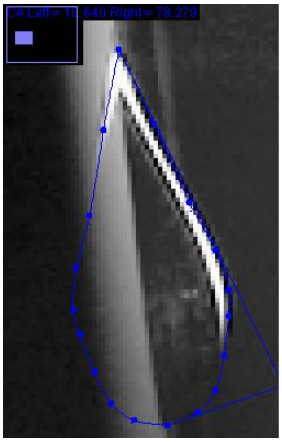

Fig. 4-2 Droplet contact angle measurement: static contact angles on surface with inclination of 83.3°

The indirect measurements, e.g., the droplet velocity, the static/dynamic advancing and receding contact angles, are measured by post-processing of video records. The droplet velocity (an average from several frames) is the ratio

of the droplet moving distance to the time passed between the selected frames. The static/dynamic contact angles of water droplets are measured between the tangents to the solid-liquid and the air-liquid interfaces in the zoomed side view images processed by an open source code ImageJ with a plugin DropAnalysis, as shown in Fig. 4-2. The contact angle reported here is the average value from several measurements at each velocity (including velocity = 0 for the static contact angle), with a measurement error about ±3° due to the user effect of ImageJ.

4.1.2 Droplet velocity model

In the present experiment, the non-uniformities in the paint layer on the steel surface results in heterogeneity, causing a contact angle hysteresis. Three tests have been done by increasing the droplet volume continuously to reach the threshold, beyond which droplets start moving with each specified inclination angle. The average static advancing and receding contact angles $\theta_{s,A}$ and $\theta_{s,R}$ of water droplets on the IOZ paint surface are measured at the onset of motion, which are about 71.8° and 18.4° respectively.

Meanwhile, one wall inclination signifies the boundary of droplet volume over surface, which can be expressed as the critical Bond number Bo_c. The comparison of critical Bond number between the DRISE data and the theoretical prediction is carried out in Table 4-2. The critical droplet volume of motion increases with inclination angle decreasing, which can be conceived intuitively. The predicted critical Bond number Bo_c is calculated by the model of ElSherbini and Jacobi (2006), as seen in section 2.2.2.1 Eq. (2-14). Calculations would be identical for water droplets on a specific homogeneous surface, due to the static contact angles that do not depend on the inclination. It seems clear that model of ElSherbini and Jacobi, is feasible to estimate the onset of motion of water droplets, despite large contact angle hysteresis (current case ~50°). The deviation between the calculations is because the adopted contact angles are different from test to test. The gap between the DRISE data and the prediction of the model of ElSherbini and Jacobi might be caused by the measurement error of contact angles.

Table 4-2 Comparison of critical Bond number

Inclination, α, °	Critical volume, V_c, μL	Critical Bond numbers, Bo_c	
		Exp.	Cal.
32.5	55.9	1.0	0.88
60.9	24.8	1.01	1.18
83.3	22.4	1.07	1.07

- **Shape of moving droplet**

When the droplet volume exceeds the onset volume on the surface with a specified inclination, the shape of the moving droplet could change with the droplet speed. The droplet contact area is no longer rounded but develops an ellipsoid at the rear with increase of droplet speed. The droplet shape is particularly easily discriminated by looking at the images recorded, as seen in Fig. 4-3. The evolution of water droplets moving on the surface with slope angle 83.3°, as shown in Fig. 4-4, indicates that the following three distinct shape regimes (oval or rounded, corner, cusp) can be identified during the evolution. A similar result is experimentally observed in references (Le Grand et al., 2005; Puthenveettil et al., 2013).

Fig. 4-3 Top view of the oval droplet with surface inclination of 32.5° (Re=84.8)

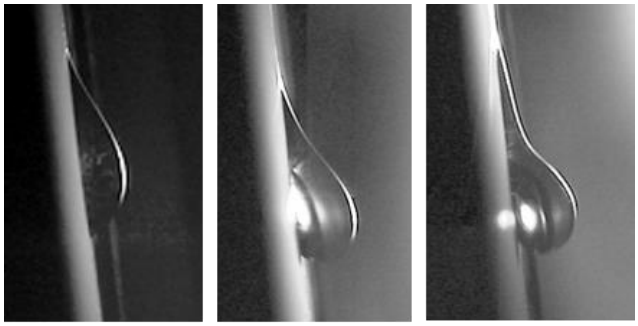

Fig. 4-4 Evolution of moving water droplet on surface with inclination of 83.3°

The Re number of the droplets in Fig. 4-4 are 65.7, 197.2 and 954.2 from left to right respectively. At different droplet velocity (obtained by changing the droplet volume while the surface inclination is fixed), the droplets adopt different shapes that are observed by recorded images. At low velocity, the droplet takes an oval shape. A corner develops at the rear with droplet velocity increasing further. The rear of the droplet is stretched by the effect of surface tension and viscosity, and then the corner shape goes to cusp. All these shapes transform quickly, in other words, these transitions take place in a short time. Finally, the

rivulet occurs and its length of the contact line increases rapidly when the droplet volume increases beyond a threshold value.

- **Dynamic contact angle model**

The droplet velocity model at low Re, takes the static contact angles into account for the surface tension, due to the assumed minor change of droplet shape. However, the geometry of the droplet changes dramatically when the droplet moves fast. Therefore, the dynamic contact angles should be considered in the droplet velocity model when droplet moves at high Re.

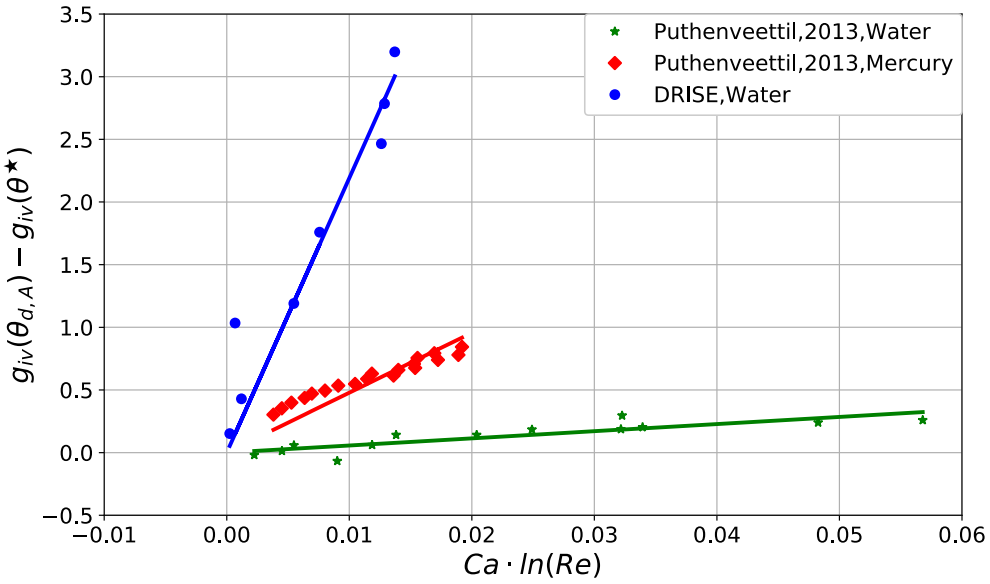

Fig. 4-5 Comparison of advancing contact angle with Cox, 1998 model

The dynamic advancing contact angle model (Cox, 1998) that considers the inertial fluid effect when droplets move at a high speed, namely, the dynamic contact angle model includes the Re number effect. Fig. 4-5 shows the comparison of the DRISE and Puthenveettil et al., 2013 experimental data with Cox (1998) model. The x-axis and y-axis represent the left and right sides of Eq. (2-28), respectively. According to Cox model, the advancing contact angles of DRISE can be fitted linearly with a pre-factor of 219, which is two orders of magnitude higher than the expected from Cox's suggestion of one. Furthermore, Puthenveettil's data of water droplets can also be fitted linearly with a pre-factor of 5.7; the data of mercury droplets need a pre-factor of 47.8. Puthenveettil's data looks closer to the predictions of Cox's model. Nevertheless, none of these three sets of data does coincide with the pre-factor of Cox's suggestion.

Therefore, in order to utilize a more common and generic empirical correlation instead of Cox model without a specific fitting factor for each case, a dynamic contact angle correlation is fitted by the present and Puthenveettil's experimental data:

$$\left(cos\,\theta_{d,R} - cos\,\theta_{d,A}\right) - \left(cos\,\theta_{s,R} - cos\,\theta_{s,A}\right) = 0.32We^{0.303}(1 - cos\,\theta_e)^{-0.747} \quad (4\text{-}1)$$

where the Weber number $We = Ca \cdot Re$. Actually, Ca and Re number are used to fit the empirical correlation as well, results show both exponents of these two dimensionless parameters are close. Thus, We number works to fit against the experimental data. The correlation structure is proposed in terms of $cos\,\theta_{d,R} - cos\,\theta_{d,A}$ since this term is required in the droplet velocity model rather than the dynamic contact angels definitely. The prediction results are assessed by the DRISE and Puthenveettil's data, as shown in Fig. 4-6. It seems that all the experimental data agree with the generic correlation Eq. (4-1). It makes sense to approximate the dynamic contact angle hysteresis, which is feasible to be substituted into the improved droplet velocity model Eq. (3-19).

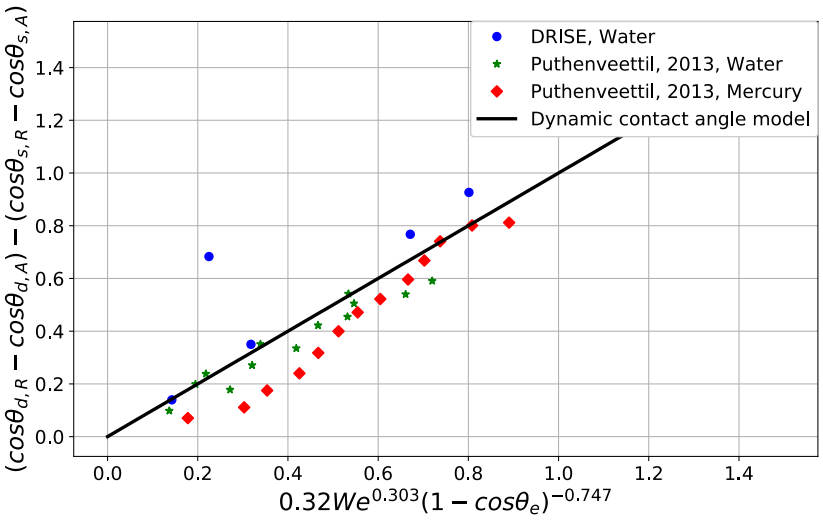

Fig. 4-6 Correlation of dynamic contact angle against experimental data

- **Droplet velocity comparison**

The dynamic contact angle hysteresis increases obviously with the droplet velocity. The new correlation of dynamic contact angle is adopted in the present model Eq. (3-19) to predict the droplet velocity. The surface tension as a resistance will therefore increase with droplet velocity apparently.

The equivalent Marangoni force is considered in the droplet force balance if there is a temperature gradient between the cold surface and bulk gas. Since there are no surface tension gradient in the current experiment and in Puthenveettil's experiment, the $\Delta\sigma = 0$ in the droplet velocity model.

The viscous force $F_{\tau,w}$ acts on the wedge part of droplet depends on the droplet size and the Re. The coefficient $c_1(\theta_e)$ of $F_{\tau,w}$ is derived by (Kim et al., 2002; Varagnolo, et al., 2013) based on the Stokes flow velocity field, which means $c_1(\theta_e)$ is only valid for small Re ($Re < 1$). In addition, the moving fast droplets usually have relatively larger droplet radius than the capillary length. Accordingly, the viscous force of the wedge part $F_{\tau,w}$ is neglected in the following comparison. However, the improved expression of F_τ (affected by Re number) is adopted in the present model Eq. (3-19) for droplet velocity assessment.

After substituting the improved expression of F_τ and the surface tension force F_σ (with dynamic contact angle model) into the force balance, the droplet velocity at high Re is obtained via the iteration of the implicit equation Eq. (3-19). The previous droplet velocity model Eq. (2-20) maintains static contact angles and the velocity gradient scaled to the ratio of the velocity and droplet height.

Fig. 4-7 shows the comparison between the model predictions and the experimental data. It indicates the present model (the solid lines) has better predictions than the previous model (the dashed lines) since the shift of contact angles from the static to dynamic and the improvement of viscous force with effect of Re are considered in the present model. Both the shift of contact angles and the Re effect increase the resistance of droplet motion. The boundary conditions of Puthenveettil's experiment for the comparison are presented in Table 4-3. The fluid properties are obtained at mean room temperature 25℃.

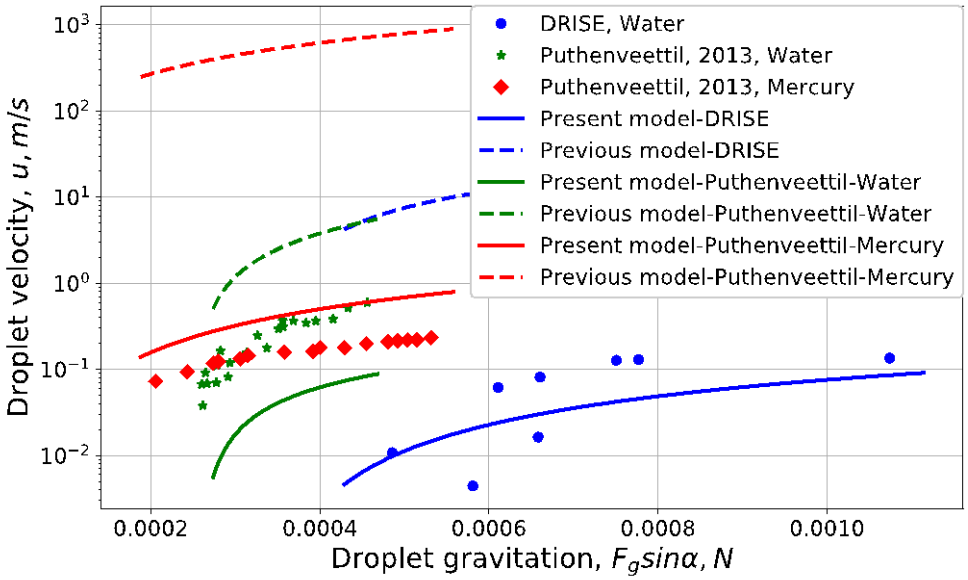

Fig. 4-7 Comparison of droplet velocity model against experimental data

Table 4-3 B.C. of Puthenveettil's experiment (Puthenveettil, et al, 2013)

	Mass, mg	u, cm/s	$\theta_{d,A}$, °	$\theta_{d,R}$, °	Ca, 10^{-3}	Re
Water	52.7	3.8-59	108.8-121.7	47.6-73.4	0.3-7.5	137-3142
Mercury	220	7.2-23	150.6-161.4	94.6-144.6	0.23-2.3	2049-20069

4.1.3 Transition criterion

A few data points are obtained to validate the criterion of the transition from water droplet to rivulet. The purpose of the transition criterion is to determine the droplet size that leads to the transition happening. When the surface tension

force at the interface between the droplet advancing and receding parts is less than the required action force on the interface, the structure will be stretched, which means the transition from droplet to rivulet starts. The transition droplet size V_t or r_t can be obtained by solving the criterion Eq. (3-24) via iteration and approximated by the proposed Bond number Bo_t Eq. (3-25) at the transition point.

Fig. 4-8 shows the comparison of water droplet radius at transition point between the predictions and experimental data. The experimental data are generally in accordance with the predictions of the transition criterion. The transition droplet size obtained by solving the criterion via iteration are closer than the proposed Bond number at the transition. The transition size of water droplet on glass (Puthenveettil's data, $\alpha = 90°$) is less than on the decontamination paint. The reasons are, on one hand, the inclination is larger than the other data points, and on the other hand, the resistance caused by surface tension on glass is less than on decontamination paint. Comparing the red point and the blue one, it reveals that the higher inclination results in smaller droplet transition size, which means the droplet on a more inclined surface reaches the transition point earlier.

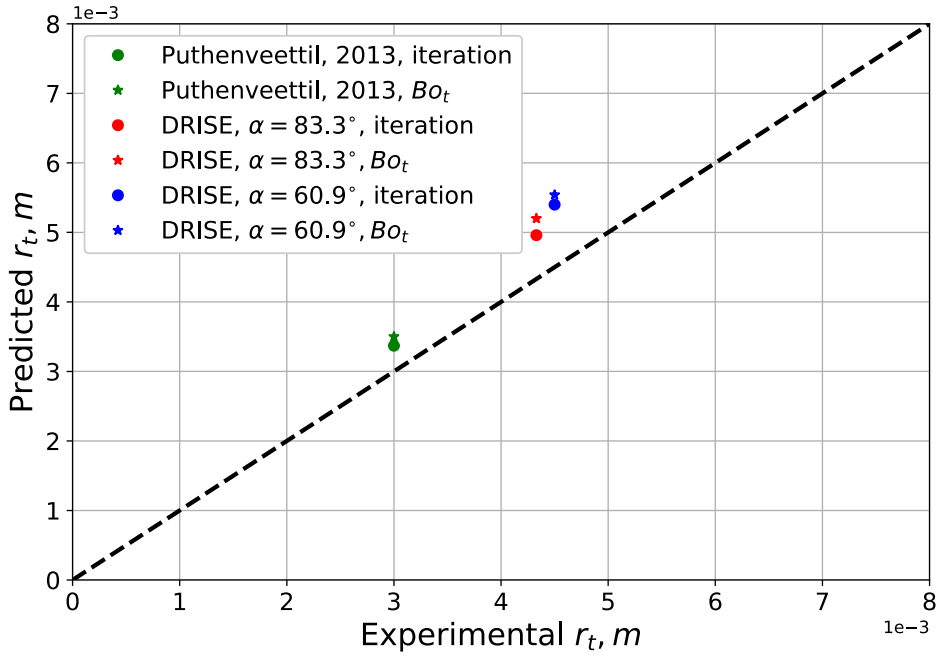

Fig. 4-8 Comparison of water droplet radius at transition point

4.2 Condensate coverage model

Four experiments including 89 experimental data points from the open literature are applied to validate the current condensate coverage model (Yu et al., 2012;

Ausner, 2007; Laufenberg et al., 2014a,b; Dupont, 2017). The information of these experimental data for validation is summarized in Table 4-4. Most of the data are expressed with Reynolds number, which is defined as $Re = 4\rho\dot{V}/\mu$. Actually not all contact angles are given by each individual experiment, but the surface materials are exactly given. In the experiment of Ausner (2007), the static contact angle measured varies between 60˚ and 70˚ with a measurement error 6-9˚. The average contact angle of 65˚ is adopted in the calculations. In THAI-AW3-LAB experiment, the equilibrium static contact angle of water on GEHOPON decontamination paint is about 60-65°.

Most of the experiments are conducted under the ambient temperature and pressure, except the LINX experiment, which is under the real containment condensation condition. It is remarkable that, for the experiments' condition without the real condensation on surfaces (WEBREC, Ausner and THAI-AW3-LAB experiments), rivulets form directly by water injection at the uppermost edge of test plates. These three experiments are adopted to validate the rivulet model and its coverage. The validation works are carried out one by one in the following sections.

Table 4-4 Experimental data for rivulet coverage validation

Experiment	Re	$\theta_{s,A}/\theta_{s,R}$	Inclination	Temperature	Data points
WEBREC	$10-500$	$71.8°/18.4°$	90°	Ambient	21
	$20-110$	$18°/10°$	90°	Ambient	15
Ausner,2007	$30-240$	$65°/-$	60°	Ambient	43
THAI-AW3-LAB	$261-285$	$\theta_e = 60-65°$	2°,10°,20°	Ambient	6
LINX	$18-62$	$65°/45°$	90°	67-113℃	4

4.2.1 Comparison with experiments

- **WEBREC experiment**

The facility WABREC (WAter Behavior in REctangle Channel) consists of a vertical stainless plate, which is 2 m wide and 5 m long. The surface of the plate is painted with organic/inorganic zinc coating. Rivulet forms on the vertical plate when the water overflows reserve tank. Water temperature is kept constant at 25℃ while the pressure is ambient. More information about WABREC experiment can be referred to (Yu et al., 2012).

WABREC rivulet experiment (without droplets) considers two paints, but only the contact angles of inorganic zinc coating are known. Therefore, the test results on inorganic zinc coating are taken to compare with the modelling approach prediction. Two sets of condensate coverage are measured at two

different surface conditions (the pre-wetted and dry surfaces) with various volume flow rates. The pre-wetted surface case means the rivulet forms on the pre-wetted plate when the water is injected on the uppermost edge of the test plate. On the contrary, the dry surface case means the rivulet generates on the dry surface of the test plate. These two surface conditions have different equilibrium contact angles. The equilibrium contact angle on the pre-wetted surface is smaller than on the dry surface. Since there are only rivulets generated in WEBREC experiment, all droplets are assumed to transfer to rivulets immediately after droplets generating on surface, which is set in the modelling approach (namely $V_t = V_0$).

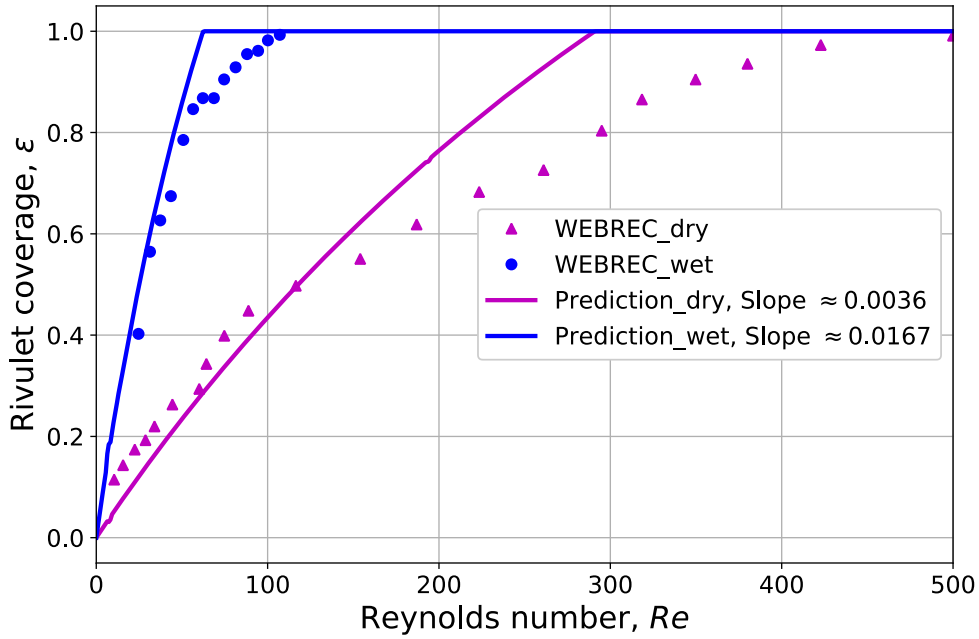

Fig. 4-9 Coverage compared with WEBREC experimental data

Fig. 4-9 shows the comparison between the modelling approach prediction and the WEBREC experimental data. The boundary conditions of the calculation are exactly the experiment conditions: the static contact angles $\theta_{s,A}/\theta_{s,R}$ are $71.8°/18.4°$ for dry surface and $18°/10°$ for pre-wetted surface; the inclination angle $\alpha = 90°$ for the vertical wall; the temperature and pressure are ambient; last it doesn't matter how much the condensation heat flux is (see section 3.4). The comparison results indicate a good agreement. The predicted relationship between the rivulet coverage and Re number is almost linear, because the average rivulet thickness and velocity do not increase much when volume flow rate increases. Looking at the condensate coverage definition:

$$\varepsilon = \frac{\dot{V}}{\bar{u}\cdot\bar{\delta}} = \frac{\mu}{4\rho\bar{u}\cdot\bar{\delta}}\cdot Re \tag{4-2}$$

It is clear that the slope of the curve is more or less $\mu/(4\rho\bar{u}\cdot\bar{\delta})$ if the rivulet

average thickness and velocity are fixed.

Another issue of interest is about the effect of contact angle. The calculation condition difference between pre-wetted and dry surface is only the contact angle, but the rivulet coverage results are quite different at the same Reynolds number, as shown in Fig. 4-9. The lower equilibrium contact angle (pre-wetted surface) is, the faster the rivulet coverage increases with the Re number since the equilibrium contact angle affects the rivulet thickness and velocity much (see the rivulet model section 2.2.3). Smaller equilibrium contact angle leads to smaller rivulet thickness and lower velocity.

- **Ausner's experiment**

The rivulet flow behavior is observed with a camera in Ausner's experiment (Ausner, 2007). The pictures are used to obtain the information on the wetting surface area. To obtain different inlet conditions the liquid can be fed onto the plate out of a tank either with an overflowing weir or through a feeding tube with several holes. Experiment investigates the rivulet coverage (without droplets) over Re number for water on a 60˚ inclined steel plate.

The steel plate used in the experiments is not treated before the measurements. Therefore, the plate has a rough surface. The static contact angle (it is mentioned in (Ausner, 2007)) measured varies between 60˚ and 70˚ with a measurement error 6-9˚. Here we think it is the static advancing contact angle since it is measured on a dry steel surface. The average advancing contact angle of 65˚ is used in the calculation. The receding contact angle is hypothetically taken as 12˚ to make the contact angle hysteresis the same as other steel surfaces. Moreover, there are only rivulets in Ausner's experiment, therefore, all droplets transfer to rivulets immediately after droplets generating as well as in the calculation of WEBREC case.

Fig. 4-10 presents the rivulet coverage plotted over the Re number compared with Ausner's experiment. It can be seen that the simulated rivulet coverage agrees well with the experimental data. The rivulets cover less area in prediction than in the experiment when the plate approaches to be fully covered. Furthermore, the experimental data themselves also have a large deviation at a specific identical Re number. This characteristic can be explained as the effect of the contact angle. The steel plate used is a non-treated surface, which is so heterogeneous that the contact angle would change in a large range.

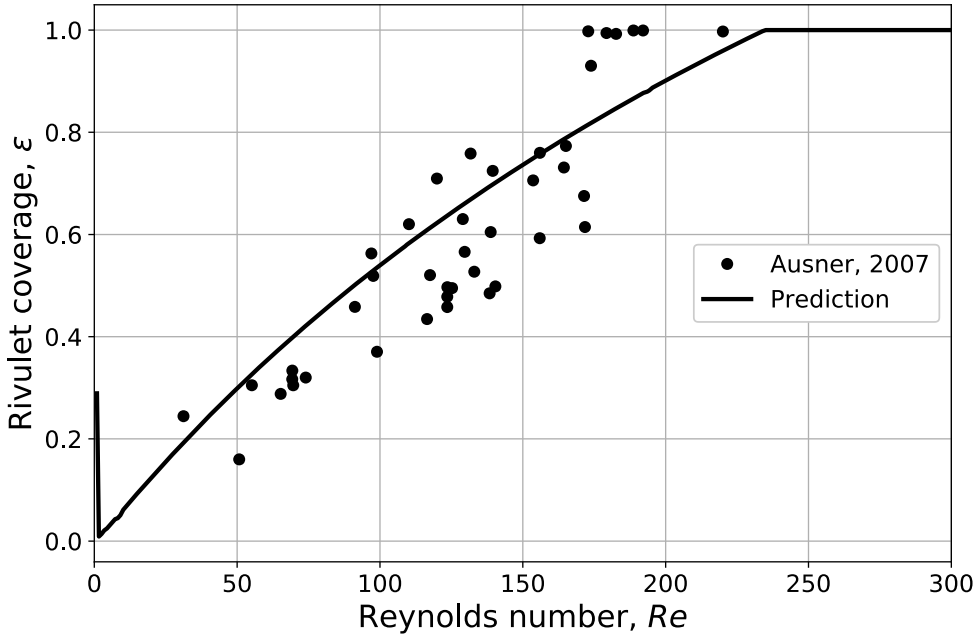

Fig. 4-10 Coverage plotted over the Re number against Ausner's experiment

- **THAI-AW3-LAB experiment**

THAI-AW3-LAB experiment is one of the aerosol wash-down experiments conducted by Becker Technologies (Laufenberg et al., 2014a,b). THAI-AW3-LAB is a laboratory scale experiment to investigate the aerosol wash-down behavior. Some tests (such as test 3, test 4 and test 12) can also be used to validate the rivulet behavior and its coverage. The experimental setup consists of trapezoidal inclined plates loaded with insoluble silver aerosol. The plates are made out of steel and have two surfaces types (stainless steel and decontamination paint). At the uppermost edge purified water is applied on the plate by a water distributor with a given mass flow rate. A tubular distributor (with 38 holes of 0.7 mm diameter along the uppermost edge) is used to generate a homogeneous water distribution. Pictures of the water flow are recorded during the tests. These images are used to identify the wetting area of the plates as well as the rivulet flow pattern. For further information, THAI-AW3-LAB laboratory experiments report (Laufenberg et al., 2014b) is recommended.

The inclinations of test 3, 12 and 4 are 2°, 10° and 20° respectively. These tests are conducted under ambient pressure and temperature. The mass flow rate is the same, 11 g/s. All test plates have the same structure size. The upper width of the trapezoidal plate is 0.475 m, and the lower width is 0.09 m, so the average Re is about 175. The surface of test 3 and 4 are stainless steel coating with GEHOPON paint, while the test 12 without paint. The water on GEHOPON paint has an equilibrium static contact angle 60-65° (the average 62.5° is adopted in the calculations). All droplets transfer to rivulets immediately after

droplets generating as well as in WEBREC and Ausner's cases.

Table 4-5 reveals the comparison of the rivulet average thickness and velocity. The average value at 130 sec of each THAI-AW3-LAB test is selected. However, for the test 12, we only have data at 900 sec from the experiment report (Laufenberg et al., 2014b). Both the experiment and calculation reveal that the average rivulet thickness decreases with the inclination increasing, on the contrary, the average rivulet velocity increases. The results are consistent with the rivulet thickness and velocity model, which are both in terms of inclination angle, roughly $\delta \propto sin\alpha^{-0.4}$ and $u \propto sin\alpha^{0.2}$ (see rivulet model section 2.2.3) if Re number, contact angle, and water properties keep constant.

Table 4-5 Rivulet parameters comparison with THAI-AW3-LAB

	Thickness, mm		Velocity, m/s	
	Exp.	Cal.	Exp.	Cal.
Test 3 - 2°	0.62	1.0	0.137	0.15
Test 12 - 10°	0.41	0.57	0.23	0.21
Test 4 - 20°	0.31	0.43	0.27	0.24

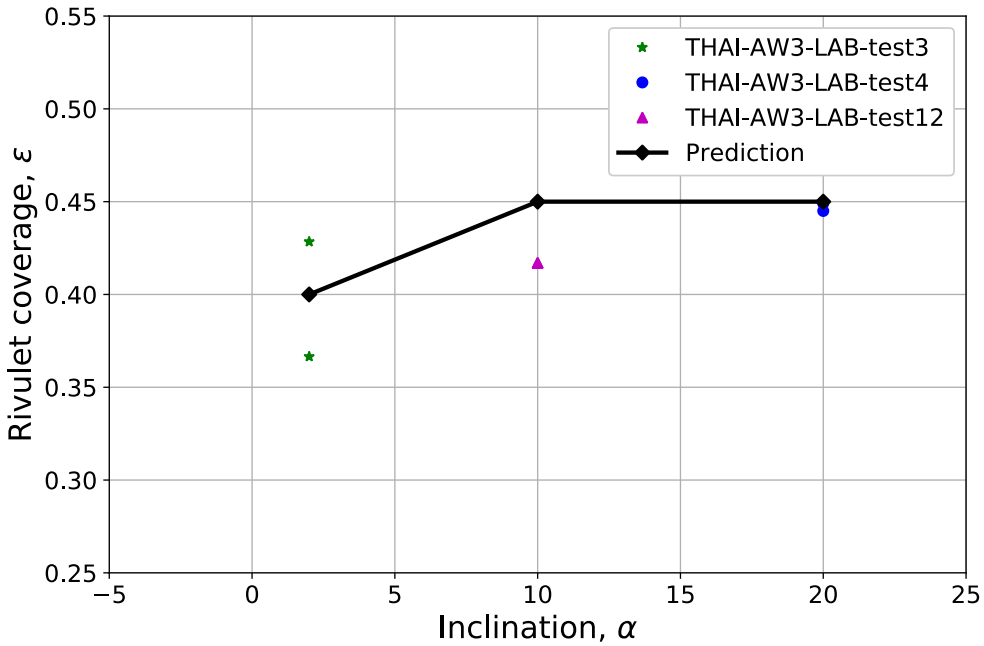

Fig. 4-11 Coverage versus inclination comparing with THAI-AW3-LAB

Accordingly, Fig. 4-11 shows the rivulet coverage comparison between calculations and THAI-AW3-LAB tests. The prediction by the modelling approach increases slightly in the beginning with inclination angle increasing. However, it seems that the inclination effect is not significant beyond a certain value. The result is also consistent with the coverage modelling approach prediction, roughly $\varepsilon \propto sin\alpha^{0.2}$, when Re, contact angle and water properties

keep constant. The experimental data show that the inclination angle does not affect the coverage very much, although the inclination angles are small. The discrepancy between the calculation and experiment might be caused by the deviation of the contact angle. The surface after the aerosol deposition cannot be homogeneous completely (Laufenberg et al., 2014a,b), so that the contact angles would differ from place to place.

- **LINX experiment**

The LINX containment condensation experiments are conducted by Paul Scherrer Institute (PSI) in Switzerland. The LINX facility consists of a single stainless steel vessel with 2 m diameter and 3.4 m height (10 m^3 in volume). A vertical cooling wall, 0.4 m wide and 2.1 m high consisting of 9 aluminum blocks, is installed in the center of the pressure vessel (Dupont, 2017). The blocks are covered by a single 0.7 mm thick aluminum sheet. The mass flow rate of cooling water is controlled independently and its inlet and outlet temperature are measured for each block, in order to calculate the average heat removal from the containment vessel.

The surface of the metal sheet has undergone a chemical etching treatment. The static advancing and receding contact angle of water on the plate are 65° and 45° respectively. The average temperature is 95 °C and the pressure is 1.1 bar. 4 tests (test 210, 215, 211, 216) of rivulets are conducted under condensation condition and without water injection at the upper plate (Dupont, 2017). The condensation mass flow rate per width at the picture captured area are 2.7, 2.9, 4.3 and 5.2 g/(m·s) respectively calculated by energy balance. Accordingly, the Reynolds numbers are 35.5, 38.6, 57 and 70 respectively.

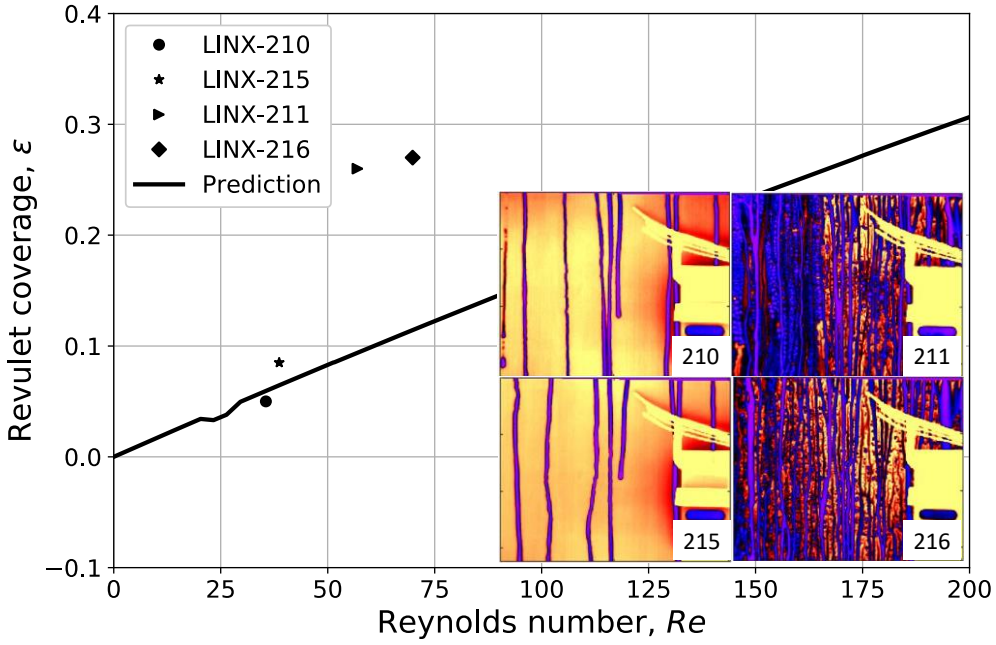

Fig. 4-12 Rivulets coverage prediction against LINX tests (Dupont, 2017)

Fig. 4-12 shows the comparison results of rivulet coverage for the given boundary condition of LINX. The four subfigures in bottom-right are the pictures of test 210, 215, 211,216 from the reference (Dupont, 2017). Color blue means the water-covered area. The area ratio is obtained by the software ImageJ process. Compared with the LINX experiment, the predictions of test 210 and 215 agree well with the experimental data, while there is a large deviation of test 211 and 216. Because test 211 and 216 contain many droplets covered on the surface (see the bottom-right subfigures in Fig. 4-12). Unfortunately, the moving droplets and the static ones cannot be distinguished in test 211 and 216. Otherwise, it is possible to compare the entire moving liquid wetting area with the present model directly.

4.2.2 Empirical correlation

In order to determine the prefactor $\frac{0.75}{c_\delta^3}$ in the proposed empirical correlation Eq. (3-34), the results of the modelling approach work are applied, e.g. the WEBREC comparison results in Fig. 4-9. Two cases with different surfaces are simulated: a pre-wetted surface and a dry one. The results reveal that the predicted relationship between the coverage and Reynolds number is almost linear, because the average rivulet thickness and velocity do not increase much when volume flow rate increases. It is consistent with the empirical correlation that the coverage is proportional to Re ($\varepsilon \propto Re$), if the rivulet average thickness and velocity are fixed hypothetically.

According to the slopes of the prediction curves in Fig. 4-9 (slope of per-wetted and dry surface are 0.0036 and 0.0167 respectively), now the prefactor of the condensate coverage empirical correlation can be evaluated $\frac{0.75}{c_\delta^3} \approx 0.26$, and accordingly the rivulet thickness prefactor $c_\delta = 1.424$. Therefore, after determining the prefactor, the empirical condensate coverage correlation can be expressed as:

$$\varepsilon = 0.26 \cdot Re^1 Ka^{-0.6}(1 - cos\theta_e)^{-0.6}(sin\alpha)^{0.2} \tag{4-3}$$

Fig. 4-13 shows the comparison between the coverage predicted by correlation with the prefactor 0.26 and the experimental data. The comparison results indicate generally a good agreement with around ±25% deviation. This deviation might be caused by the variation of the surface contact angle, e.g. the steel plate used in the experiment of (Ausner, 2007) is a non-treated surface. The roughness of the surface is so uneven that the contact angle varies in a large range.

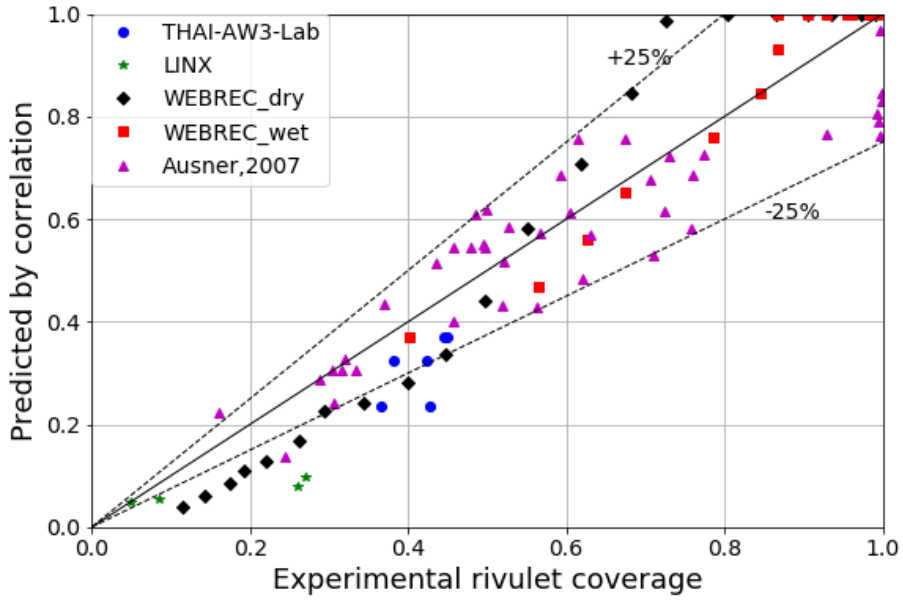

Fig. 4-13 Coverage comparison between correlation and experiments

4.3 Extended aerosol wash-down model

After coupling the **CON**densate cove**RAG**e model (**CONRAG**, which is the empirical correlation with prefactor provided by the results of modelling approach) with the aerosol wash-down model AULA corrected by the proposed factor of inclination and cohesion, this combined model is validated by the laboratory scaling experiment THAI-AW3-LAB. The modified COCOSYS (the version GRS delivered to KIT on 7 October 2019) coupled with CONRAG and AULA is validated by the integral experiment THAI-AW3.

4.3.1 THAI-AW3-LAB experiment

4.3.1.1 Test condition

The laboratory scale experiment THAI-AW3-LAB is developed and constructed in order to investigate the removal of insoluble silver aerosol deposited on inclined surfaces by rivulet flow (Laufenberg et al., 2014a,b; Gupta et al., 2015). The rivulet coverage of THAI-AW3-LAB has been discussed in section 4.2.1. Here the aerosol wash-down behavior is concentrated. The experimental setup is used to perform a series of aerosol wash-down tests, in which surface inclination, water mass flow rate, aerosol load as well as particle sizes are varied. Two different surfaces types (stainless steel and decontamination paint) of interest are representative for containment structures. A total of 15 tests are conducted. Each test consists of an initial dry aerosol-loading phase and the later wash-down phase. The experimental data exhibit a clear trend of a fast

aerosol wash-down in the beginning, which is followed by a slow removal transient. As discussed in the validation of modelling approach of coverage, test 3, 4 and 12 are taken to validate the aerosol wash-down behavior again. The setup consists of trapezoidal inclined plates loaded with insoluble silver aerosols. For further information, THAI-AW3-LAB laboratory experiments report (Laufenberg et al., 2014a,b) is recommended.

Table 4-6 Parameters of THAI-AW3-LAB

		Test 3	Test 4	Test 12
Aerosol surface load		26.4 g/m^2	27 g/m^2	10.2 g/m^2
Surface inclination		2°	20°	10°
Surface of plate		Decontamination paint on steel	Decontamination paint on steel	Steel
Mass flow rate		11 g/s	11 g/s	11 g/s
Particle diameter		1.5-2.5 μm	1.5-2.5 μm	0.7-1.2 μm
Effective particle density		1100-2000 kg/m^3	1100-2000 kg/m^3	1100-2000 kg/m^3
Coverage	At 130 sec	42.8%	44.5%	-
	At 900 sec	45.6%	44.9%	41.7%

THAI-AW3-LAB test 3, 4 and 12 with the surface inclination 2°, 20° and 10° respectively, are conducted under ambient conditions and the same water mass flow rate. The surface load and silver particle diameter of test 3 and 4 are similar, while those of the test 12 are smaller. The parameters of THAI-AW3-LAB are summarized in Table 4-6. In the experiments, the particles are collected in intervals of 10 sec for a total duration of 130 sec. The aerosol wash-down by rivulet is recorded in each 10 sec. The effective particle density is used in the aerosol wash-down calculations, because aerosol in containment is usually surrounded by water due to the condensation on aerosols. The effective particle density can be roughly determined in the range of the aerosol bulk density and the aerosol density with water fully filled the void space (which numerically is the aerosol bulk density plus the product of water density and aerosol porosity, namely, 1100 kg/m^3 + 0.9 * 1000 kg/m^3 = 2000 kg/m^3). The mean effective particle density 1550 kg/m^3 is adopted in the current simulation of THAI-AW3-LAB.

4.3.1.2 Aerosol wash-down mass

The comparisons of the aerosol wash-down mass against THAI-AW3-LAB experiments (test 3, 4 and 12) are shown in Fig. 4-14, Fig. 4-15 and Fig. 4-16 with the erosion constant ($k_{e,0}$ in Eq. (2-2)) 0.4, 0.005 and 0.03 respectively. The erosion constant has to be estimated and is different from case to case, which depends on the used properties of surface, aerosol, fluid, and the wash-down situation (Weber et al., 2015; Amend and Klein, 2018). All the computational conditions are described in Table 4-6, except the rivulet

coverages of 23.5%, 32.5% and 37.1% for test 3, 4 and 12 respectively that are calculated by the proposed correlation Eq. (4-3).

The comparison results of aerosol wash-down mass generally show good agreements with experimental data, but still have the deviations. E.g., in the later phase of wash-down (from 60 to 130 sec), the prediction of aerosol wash-down mass is lower than the experiment. The aerosol wash-down mass is somehow linear or constant in the later phase. An explanation is that the rivulet entrains the aerosol along the both edges of each rivulet. The rivulet entrainment is an additional source of the aerosol wash-down mass (Freitag et al., 2018). Nevertheless, in the early 60 sec, the deviations are also found. The possible reason is that the rivulet coverage estimation has already about ±25% deviation.

Table 4-7 shows the comparison of the total aerosol wash-down mass between model prediction and the THAI-AW3-LAB experimental data. The total aerosol mass load on each test plate can be calculated by the aerosol surface density (the aerosol surface load in Table 4-6) times the plate area. In experiments, the aerosol wash-down efficiency, namely the fraction of the total aerosol wash-down mass (at the end of 130 sec) to the total deposited mass is about 10%-15%, while in predictions, the efficiency varies from about 11% to 18%. The comparisons reveal that there are no significant differences between the calculation and measurement.

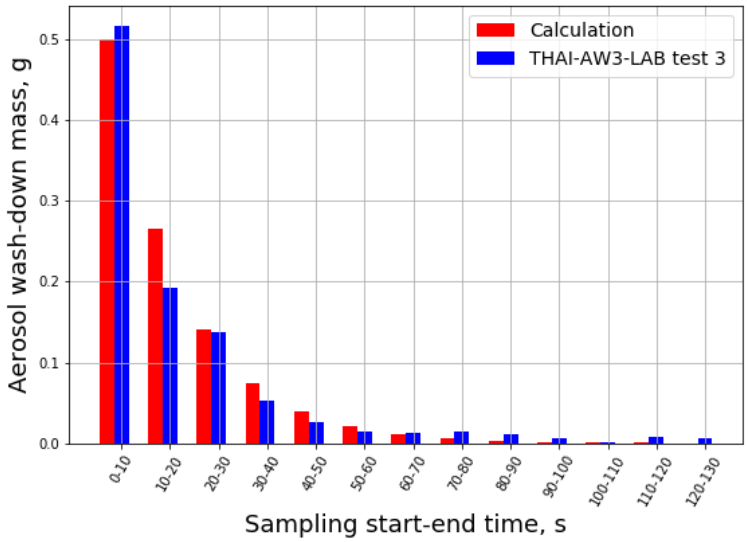

Fig. 4-14 Aerosol wash-down mass comparing with THAI-AW3-LAB test 3

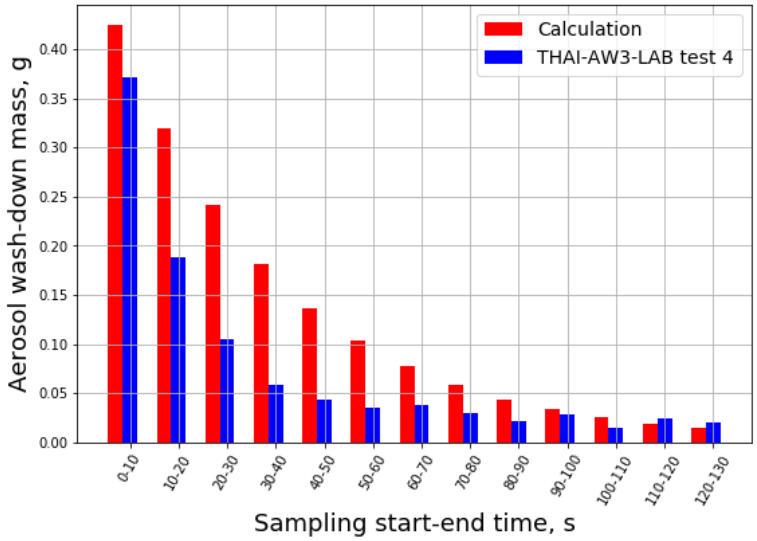

Fig. 4-15 Aerosol wash-down mass comparing with THAI-AW3-LAB test 4

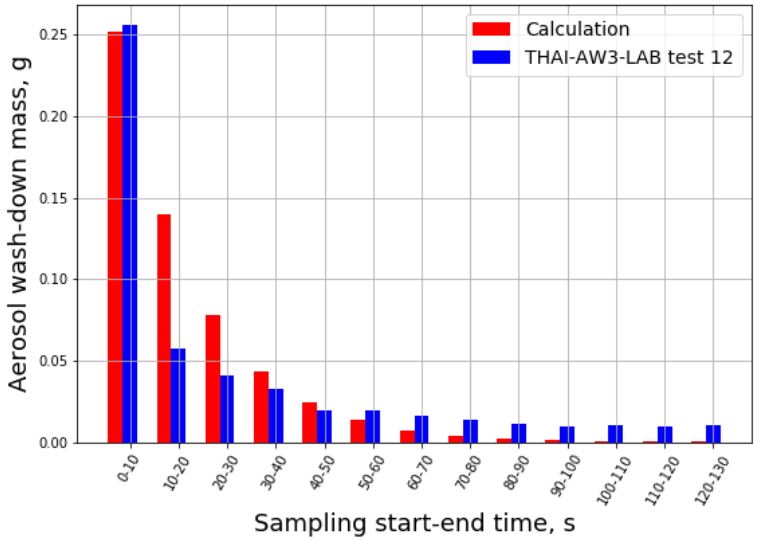

Fig. 4-16 Aerosol wash-down mass comparing with THAI-AW3-LAB test 12

Table 4-7 Total aerosol wash-down mass comparing with THAI-AW3-LAB

	Test 3		Test 4		Test 12	
	Exp.	Cal.	Exp.	Cal.	Exp.	Cal.
Total mass load, g	9.1		9.3		3.5	
Total mass wash-down, g	1.0	1.06	0.98	1.67	0.51	0.56
Efficiency	11.1%	11.6%	10.5%	17.9%	14.5%	16%

4.3.2 THAI-AW3 integral experiment

The THAI-AW3 integral experiment is one of the aerosol wash-down experiments carried out in THAI project. The THAI-AW3 experiment has been performed to investigate the aerosol wash-down behavior of insoluble aerosol silver on surfaces, which are the vertical surfaces, quasi-horizontal tray (plate with small inclination 2°) and a small puddle. The objects of the experiment are to identify the dominant parameters and transport mechanisms of the insoluble Ag aerosol deposited on walls and to determine the aerosol wash-down efficiency (Freitag et al., 2016).

4.3.2.1 THAI facility and test procedure

- **THAI facility**

THAI is a technical scale containment test facility designed and built to address fission products and thermal-hydraulic issues under DBA and SA conditions. The main component of the THAI facility is a cylindrical stainless steel vessel of 9.2 m height, 3.2 m diameter, and total volume of 60 m³ with exchangeable internals for multicompartment investigations (Gupta et al., 2015). THAI test vessel is installed with internal trays for aerosol wash-down on quasi-horizontal surfaces. The vessel is designed for a maximum overpressure of 14 bar at 180 °C. The cylindrical part of the THAI vessel is equipped with three independent heating/cooling systems over the height for the wall temperature conditioning by means of external thermal oil circuits. The sump water can be heated and recirculated at different flow rates. The vessel structures are made of stainless steel and completely enveloped by a 120 mm rock wool for thermal insulation. The inner wall is 22 mm thick. The 16.5 mm gap between the vessel walls is filled with thermal oil of the wall heating/cooling system. The outer wall is made of 6 mm thickness stainless steel. Vessel top and bottom are formed by dished heads (with wall thickness 30 mm), both of which are penetrated in the vessel by a top cylinder with diameter 1.54 m and a bottom cylinder with diameter 1.368 m respectively. The top cylinder is joined by a 120 mm thick top flange. The bottom cylinder is closed by a 16 mm thick dished head. More details of the THAI geometry can be found in reference (Freitag et al., 2016).

- **Test procedure and test conditions**

The test procedures of THAI-AW3 are established under well-controlled test conditions (Freitag et al., 2016). Time t = 0 h corresponds to the start time of steam injection. The procedures during the test, as described in Fig. 4-17, are introduced as below:

Phase 0 is the preconditioning with time duration 13.83 h (start at t = - 42.08 h) to have initial conditions for aerosol injection. The heating system (jackets) starts with a target wall temperature of 128 °C except the sump compartment, which is set to 110 °C.

Phase 1 is the aerosol injection and deposition phase with time duration 28.25 h. Three times of aerosol injections with the carrier gas 'air' are activated, so that the vessel pressure increases three times accordingly. The total mass of silver injected in the THAI vessel is 465.5 g. The mass-median-diameter (i.e. the average particle diameter by mass) is about 1.1 μm. Then the vessel atmosphere remains quiescent to allow the deposition of aerosols on the surfaces. There are 10 coupons removed at time t = - 6.37 h to quantify the Ag aerosol surface load. The aerosol surface load is between 32.7 g/m² and 36.3 g/m². The average surface load of these 10 coupons is about 35.1 g/m². Considering the total injected amount of 465.5 g silver aerosols, the average load on the vertical walls can be approximated 2.5 g/m^2. The vessel pressure is regulated by opening the pressure relief valve to reduce to about 1 bar. Air injection starts to establish the vessel pressure after closing the vessel.

Phase 2 is the aerosol wash-down with time duration 3.32 h. The time t = 0 h indicates the start of steam injection at the elevation of 2.4 m by a pipe with inner diameter 44 mm. The steam mass flow rate maintains almost constantly at about 17 g/s.

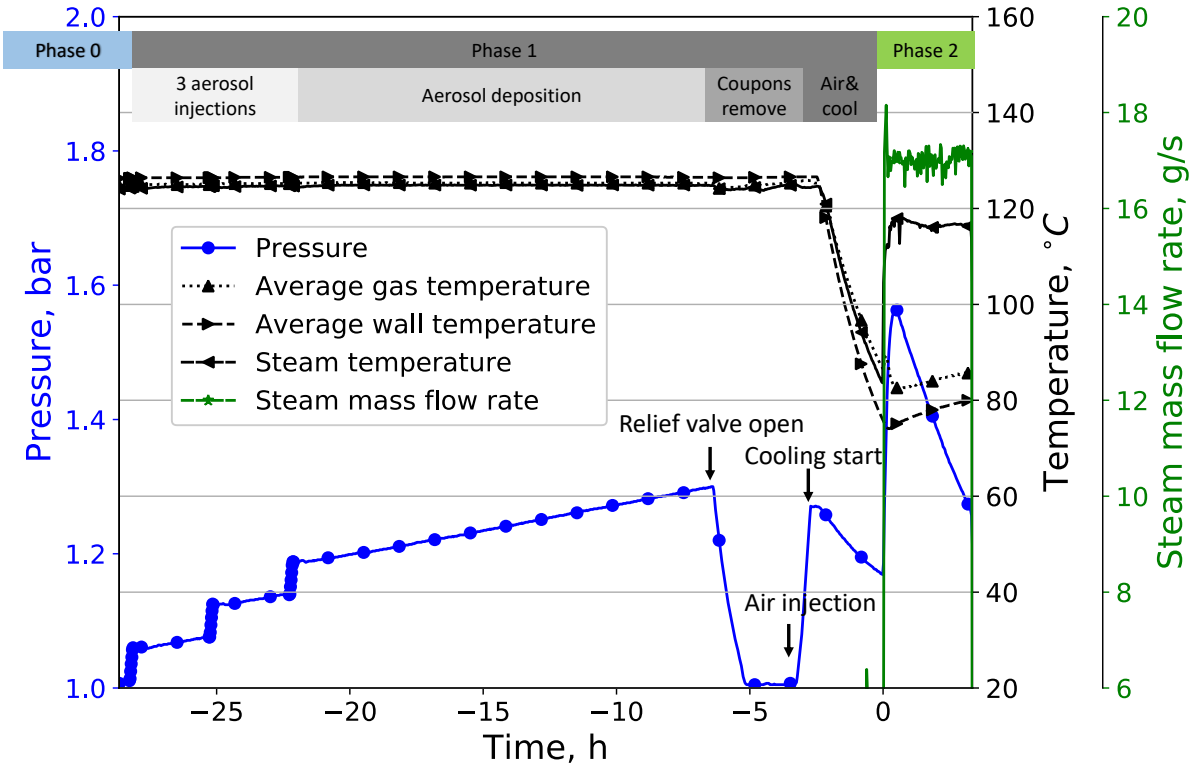

Fig. 4-17 Test procedures and test conditions of THAI-AW3

Actually, there is a phase 3 of THAI-AW3, namely the iodine/silver interaction in a water sump, but it is not the topic discussed in this paper. Here, we concentrate on the aerosol wash-down process, so that the phase 0 and 1 are the initial condition of our COCOSYS simulation. Some other parameters of aerosol wash-down model required in the simulation of THAI-AW3 are obtained

based on the knowledge of our previous validation with laboratory scale experiment THAI-AW3-LAB, e.g. the effective particle density is 1550 kg/m^3, the erosion constant $k_{e,0} = 0.03$ in Eq. (2-2), the combined correction factor $C_{i,c}$ for surface inclination and particle cohesion is unit one, etc. However, in current case the rivulet for aerosol wash-down occurs on pre-wetted surface is assumed (because steam condensation happens before aerosol wash-down) so that the equilibrium contact angle is recommended 14°, which is a measured value on pre-wetted surface coated decontamination paint.

4.3.2.2 COCOSYS model of THAI-AW3

In order to simulate the thermal-hydraulics in THAI facility, it is necessary to subdivide the vessel into a certain number of control volumes. In the current simulation, three levels are used for the upper, middle, and lower cooling jacket compartments individually. The plume shaped control volumes consist of the injection flow path. The side view of the nodalisation is presented in Fig. 4-18.

The quasi-horizontal tray installed in the vessel consists of 20 individual plates, in which 4 plates create a small puddle (39 mm depth, 26.9 liter volume), as shown in Fig. 4-19. Each plate is fan-shaped with an angle of 18° and inclined with a downward angle 2°. The surface area of each plate is 0.37 m^2. All quasi-horizontal plates are coated with artificially aged decontamination paint. Four plates have been bypassed by installing a condensate gutter, which collects condensate from the vertical wall directly. The remaining plates are flushed by the condensate, which flows directly from the vertical vessel walls to the plates. In order to allow the gas flow path also possible in the horizontal direction, nodalisation is subdivided into 4 sections circumferentially: the vertical wall section of 72°, the combined wall/plate section of 72°, the combined wall/puddle section of 72°, and the combined wall/remainder section of 144°, which in short are wall, plate, puddle, and remainder section respectively. The injection plume zone in the middle. The top view of the nodalisation is presented in Fig. 4-19.

The atmosphere junction type is the standard model to describe the atmospheric flow between two connected control volumes (zones). The junction can be a real flow path (like the plume zone to the lower head zone) or a virtual flow path, which results from subdividing of the vessel into several control volumes. For the simulation of the liquid flow from one zone to another, the drain junction model is available. Moreover, the flow path model is adopted to simulate the condensate flow from the upper to the lower structures. Finally, in the current nodalisation model of THAI-AW3, there are 28 zones, 45 atmosphere junctions, 5 drain junctions, and 30 heat structures.

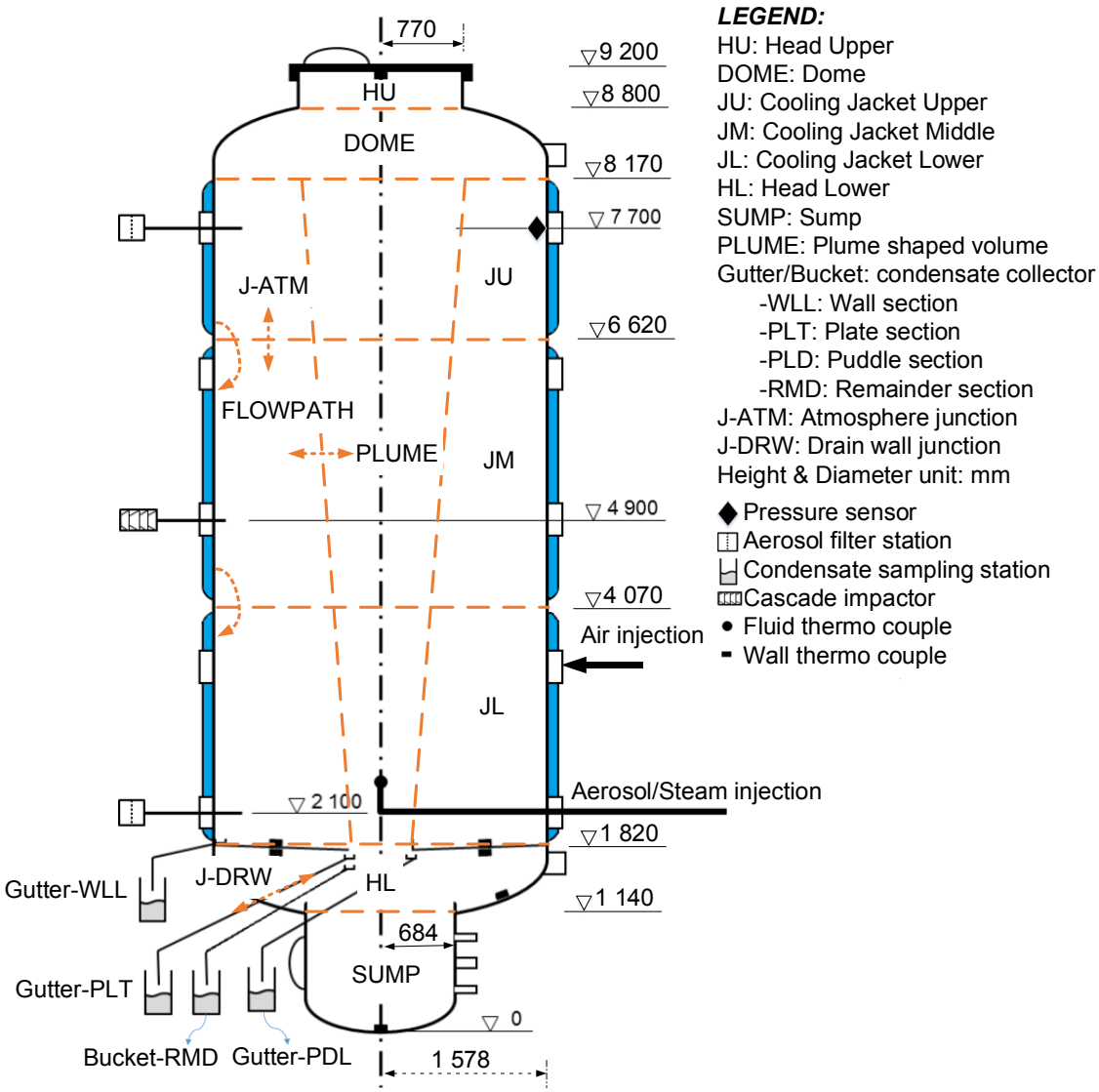

Fig. 4-18 Nodalisation and side view of THAI-AW3

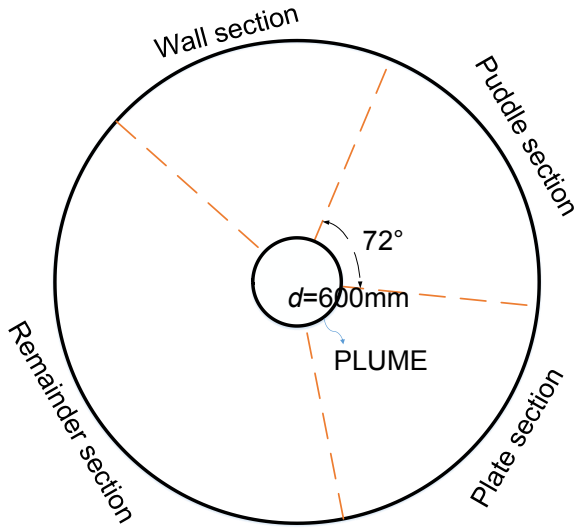

Fig. 4-19 Nodalisation and top view of THAI-AW3 at elevation 1.82 m

4.3.2.3 Results comparison

The preconditioning and aerosol injection/sedimentation (phase 0 and phase 1) are not included in the simulation, which starts at time t=0, as indicated in Fig. 4-17. The aerosol deposition loads provided by experiment are given in the input deck, so that the aerosol wash-down model is validated directly without including the simulation uncertainties of the aerosol injection/sedimentation process.

In accordance with the objectives of the aerosol wash-down test, the parameters such as pressure, temperature, aerosol concentration, and condensate flow rate are measured (Freitag et al., 2018). Fig. 4-20 shows the COCOSYS results of pressure and temperature compared against experimental data. The pressure measurement is located inside the vessel at level 7.7 m, as shown in Fig. 4-18. The pressure increases rapidly in the beginning of the test because of the steam injection and the little condensation on walls, but the trend changes in the later phase since the condensation balances the energy released by the steam in the vessel.

A set of thermocouples for measuring the temperatures of the atmosphere inside the THAI vessel over the height and circumference is installed (Freitag et al., 2018). Here, the average gas temperature is taken as the example for the comparison, as shown in Fig. 4-20. Both the trend and quantity agree with the experimental data well.

The condensate from each test section (plate, wall, puddle, and remainder, as shown in Fig. 4-19) are continuously drained into the corresponding gutters attached to each section. Fig. 4-21 shows the calculated results of the condensate mass flow rate agree well with the experimental data, but start a little ahead of experimental data and show slight oscillation, because a part of the condensate (~0.0792 kg) is reserved in each gutter that delays the condensate measurement. In the beginning, the difference of the condensation rate between the wall and plate sections is mainly due to the condensation on the flat plate (due to initial wall temperature less than the steam), but it is also influenced by the inhomogeneity of the power of the cooling system. It is the similar reason to explain the deviation of the condensation rate of the remainder section is not doubled to the plate section although the geometry is symmetric. The cooling power is different from section to section. The cooling system is an oil jacket around the containment vessel with cold oil inlet and heated oil outlet. The inhomogeneity could cause the wall heat flux differently.

Moreover, the fluctuation of steam injection, as shown in Fig. 4-17, leads to the fluctuation of the condensate flow rate. The condensate drained during the experiment from each test section is collected outside the vessel, which is measured manually every 45 seconds once the drainage flow begins. The measured condensate of the puddle section is much later than the other three test sections since the condensate is reserved in the puddle for a long time

(about 1.7 h) until the condensate overflows the weir of the puddle.

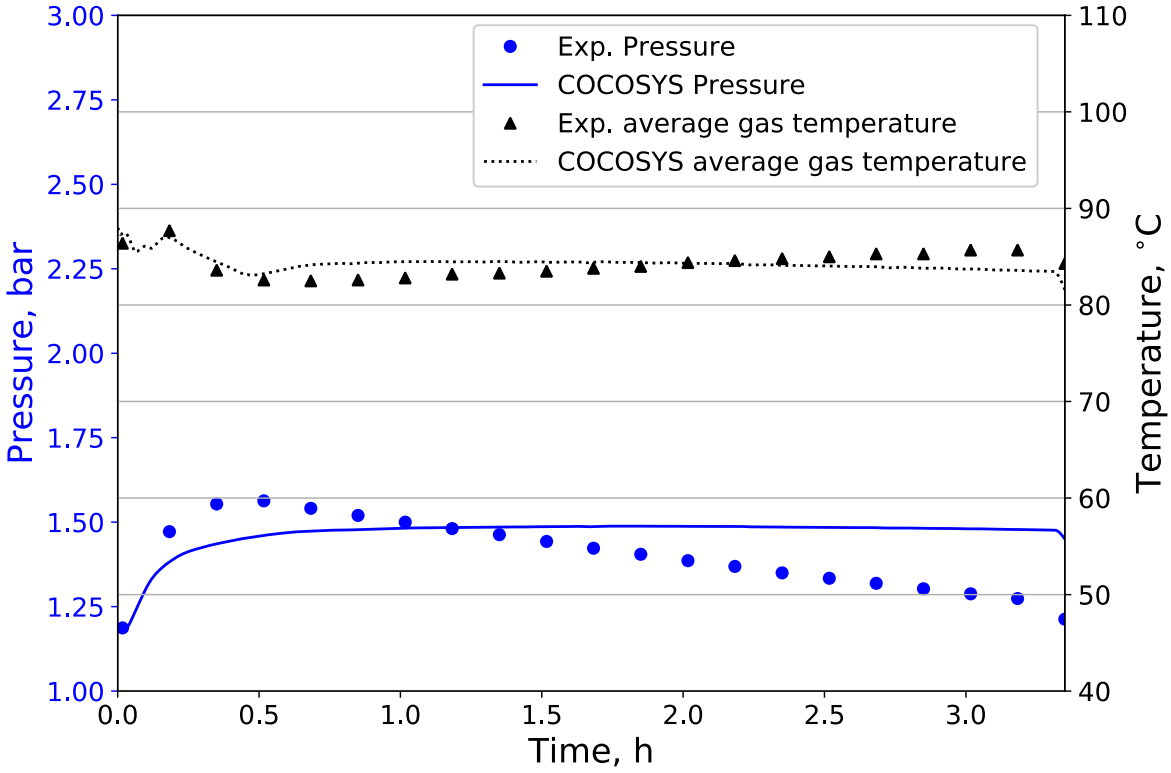

Fig. 4-20 Pressure and temperature comparison against THAI-AW3

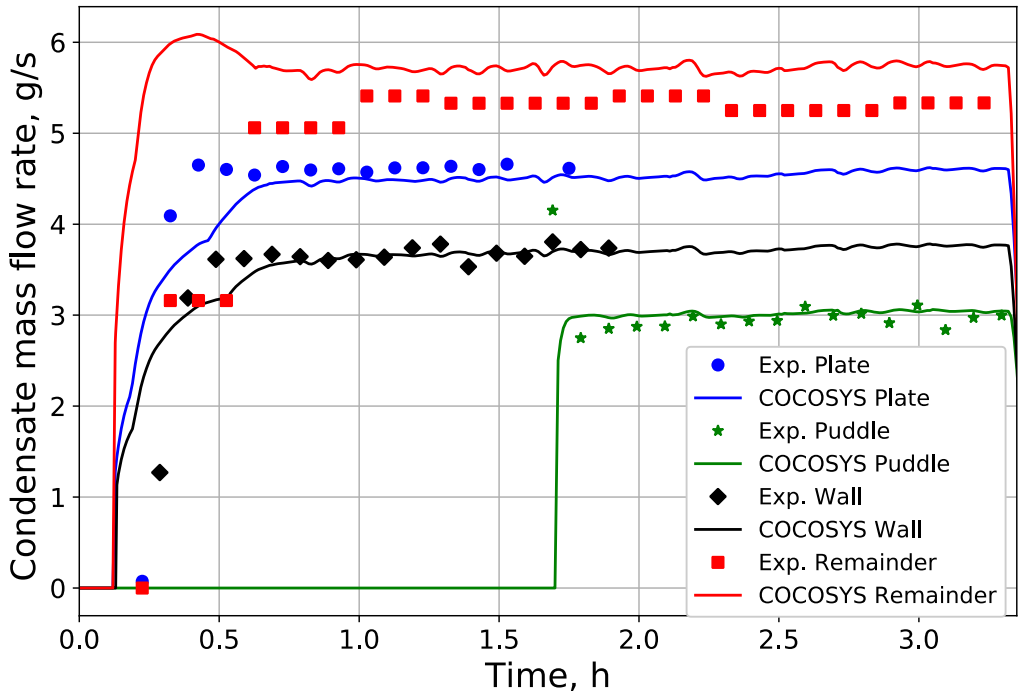

Fig. 4-21 Condensate mass flow rate comparison against THAI-AW3

Taking into account the results presented in Fig. 4-20 and Fig. 4-21, the pressure, temperature and condensate mass flow in THAI-AW3 experiment are predicted well by COCOSYS and there are no significant differences between the calculation results and the measurement data. This compliance means the thermal-hydraulic model of COCOSYS is acceptable for the further analysis on condensate coverage and aerosol wash-down process.

The cumulative aerosol wash-down masses of each section compared against THAI-AW3 experiment are shown in Fig. 4-22. In the early beginning 1 h, aerosols are washed rapidly for all these three sections (wall, plate and puddle; there is no wash-down experimental data of remainder section), then slowly in the later phase (after 1.5 h). The comparisons of aerosol wash-down generally show good agreements with experimental data, but still have deviations. The predictions of aerosol wash-down start a little earlier than the experiment since the rivulets occur before the measurement. The aerosol wash-down masses increase linearly in the later phase. The conclusion of comparison is similar to the THAI-AW3-LAB experiment, as discussed in section 4.3.1. The explanations are that the rivulet entrains the aerosol along rivulet edges (Freitag et al., 2018) and the deviation of rivulet coverage estimation is about ±25%. The wash-down from the puddle ground overestimated since the water reserved in the puddle may compact the aerosol for a while in reality before the water overflows the puddle weir, which leads to the increasing of the aerosol critical shear stress.

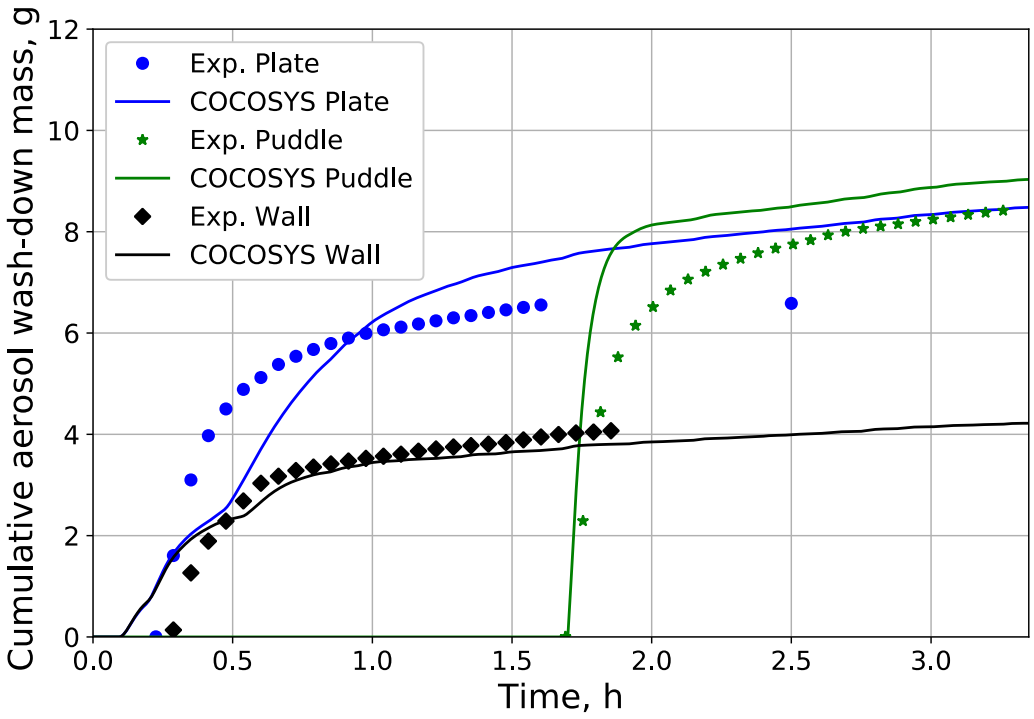

Fig. 4-22 Comparisons of aerosol wash-down mass of different test sections

Table 4-8 Aerosol wash-down mass comparison

	Wall section		Plate section		Puddle section	
	Exp.	Cal.	Exp.	Cal.	Exp.	Cal.
Total mass load, g	30.7(walls)		30.7(walls) + 52(tray)		30.7(walls) + 52(tray)	
Total mass wash-down, g	4.93	4.25	7.83	8.4	8.54	9.1
Efficiency	16%	13.8%	9.5%	10.1%	10.2%	11%

Table 4-8 shows the aerosol wash-down mass comparison between the COCOSYS calculation and the THAI-AW3 experiment. The aerosol wash-down efficiency is defined as the ratio of aerosol wash-down mass to the total initially deposited aerosol mass. The experimental aerosol wash-down efficiency is about 16%, 9.5% and 10.2% for the wall section, the plate section and the puddle section, respectively (Freitag et al., 2016). The total amount of aerosol collected in measurement is about 4.93 g for the wall section, in which 4.1 g aerosols are collected continuously for the first 1.5 h. The other aerosol removal is about 0.83 g during the later period. The corresponding vertical wall has 12.5 m^2 surface area with a total approximated load of 30.7 g; hence, approximately 16% of the silver aerosols have been removed during the whole wash-down phase. For the plate and puddle sections, the total mass load has to include the aerosol deposited on their corresponding trays (each section of 52 g). The aerosol wash-down efficiency calculated by COCOSYS is about 10%-14%, which is close to the experimental data.

In summary, the simulation results are generally in good agreement with the experimental data. The key-lessons learned from the validation exercise possibly used in application activities (e.g. Chapter 5), are: (1) The condensate coverage crucially influences the aerosol wash-down efficiency. Thus, a reliable model such as the newly developed model CONRAG is necessary to be implemented into the COCOSYS code, instead of a user-defined value. (2) The constants used in the aerosol wash-down model are defined here by experiment result, e.g., the aerosol effective density is 1550 kg/m^3 due to the steam condensed on the aerosol surface. The erosion constant is 0.03 1/s, which is, however, dependent on the aerosol particle properties. (3) The nodalisation and heat transfer model should be acceptable for the simulation of the containment thermal hydraulics.

5 APPLICATION TO GENERIC CONTAINMENT

The purpose of this chapter is to test and apply the aerosol wash-down model AULA coupled with the condensate coverage model CONRAG to a ‘Generic Containment’. It is to check out how the severe accident scenario affects the aerosol behavior, e.g. the aerosol injection, deposition, wash-down, distribution, etc. The focus here is put on the aerosol wash-down phenomenon.

Within the European SARNET2 project, a ‘Generic Containment’ nodalisation, based on a German pressurized water reactor, was defined in order to investigate the influence of the LP containment code on the calculation results of a nuclear power plant scale, which was applied for testing new models on plant scale. Based on the benchmark in SARNET2, the input deck of COCOSYS will be refined and modified for the simulation of the aerosol wash-down process. A small break loss-of-coolant accident with the loss of secondary heat sink and all active safety injection systems is planned to be simulated by using the specified source term as well as the hypothetical aerosol injection after the core degradation. The containment thermal-hydraulics and aerosol behavior (especially the aerosol wash-down process) over a full severe accident transient are investigated.

5.1 COCOSYS model of ‘Generic Containment’

5.1.1 Introduction of containment

The specification of the ‘Generic Containment’ is referred to a German four loop PWR Konvoi type with 1300 MWe (Bönigke et al., 1998). The containment system of the Konvoi consists of the containment and the reactor building surrounding it, as seen in Fig. 5-1 (Chin et al., 2014). The containment provides a barrier against the release of radioactive substances. It consists of a spherical steel vessel with a diameter of 56 m and a (nominal) wall thickness of 38 mm that is designed to withstand the pressures and temperatures that could occur during accidents. The reactor building consists of an inner steel shell (design pressure 8 bar, volume 70000 m^3), which contains the reactor system, as well as an outer concrete building, which houses the safeguard compartments (volume 42000 m^3) (Kelm et al., 2014). The lower spherical part rests on a concrete foundation, and apart from that, the containment is self-supported. The containment contains the entire reactor coolant system, which is under operating pressure, the spent fuel pool and parts of the directly connecting safety systems and reactor auxiliary systems. The containment is the third barrier for compliance with the protection objective of the limitation of activity release.

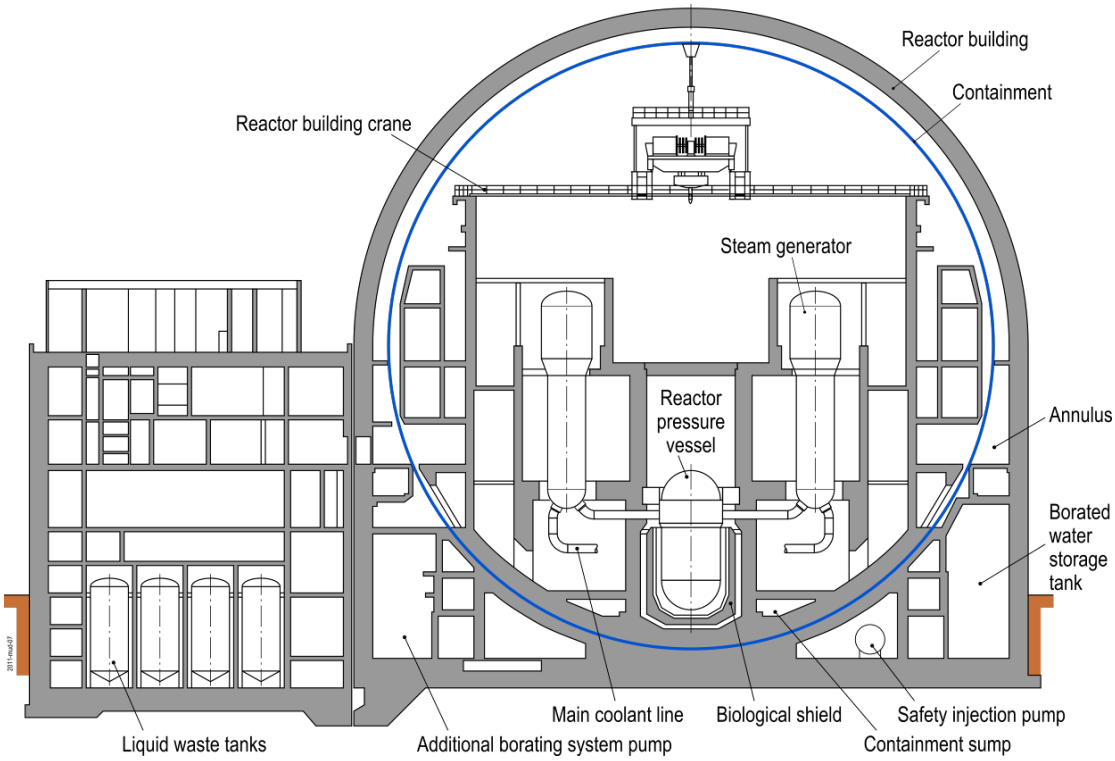

Fig. 5-1 German four loop PWR type Konvoi NPP (Chin et al., 2014)

The reactor system consists of four primary coolant loops with vertical U-tube steam generators. The reactor cooling systems (including steam generators, pumps, etc.) are located in equipment compartments separately, while the Emergency Core Cooling Systems (ECCS) are located in the reactor building annulus and reactor auxiliary building (Chin et al., 2014). The containment related systems are the hydrogen mixing system with thermal recombiners, the exhaust system, and the nuclear ventilation system. Four independent trains of safety systems exist (high-pressure and low-pressure injection system, accumulators). There is no containment spray system in this design. The reactor building, which consists of a hemispherical dome and a cylindrical base, surrounds the containment. The reactor building has a wall thickness of approximately 1.8 m and rests on a foundation. The area between the lower cylindrical part of the reactor building and the containment forms an annulus where parts of the reactor systems are located. In case of an accident, involving an increase in either pressure or temperature in the containment, the containment isolation and with some time delay the annulus isolation is triggered and the emergency sub-atmospheric pressure system in the annulus is started. This system has the task to retain the sub-atmospheric pressure in the reactor building annulus and to filter potential leakages from the containment vessel before discharge (Chin et al., 2014).

5.1.2 Nodalisation

Within the European SARNET2 project (Severe Accident Research NETwork of excellence), the ‘Generic Containment’ nodalisation was developed in order to investigate the influence of user effect, LP containment codes and modelling choice on the calculation results. It was used to compare and evaluate the analyses performed with different LP codes and models as a benchmark exercise. This ‘Generic Containment’ was applied for testing new models on plant scale (Kelm et al., 2014, for testing the hydrogen recombiner models) and performing the uncertainty and sensitivity analysis (Povilaitis et al., 2017).

The benchmark was composed of three exercise runs with increasing complexity: Run-0, Run-1 and Run-2. ‘Run-0’ concerned only the containment thermal-hydraulics of the in-vessel phase during a small break loss-of-coolant accident (SB-LOCA). The main objectives of Run-0 with the comparison of obtained results, were to develop the comparable input decks for different codes and to evaluate the modellings. While ‘Run-0’ was conducted as an initial preparatory step, the ‘Run-1’ (Kelm et al., 2013) is extended for severe accidents by including releases of H_2, CO and CO_2 in-vessel and ex-vessel. The subsequent ‘Run-2’ was additionally extended by adding a system of passive autocatalytic recombiners (PAR) in order to test different PAR modelling approaches (Kelm et al., 2014).

The original nodalisation of the benchmark was developed by

Forschungszentrum Jülich (FZJ) and RWTH Aachen University (RWTH) for the SARNET2 ‘Generic Containment’ activity (Kelm et al., 2014). However, here the containment dome is refined into several layers, specified the water flow path on containment shell structures, the structure inclination angle, and contact angle for the simulation of aerosol wash-down. Fig. 5-2 gives an overview of the control volumes and the connections between them.

The compartments of the reactor and auxiliary building have been grouped in 34 control volumes (zones) in the ‘Generic Containment’ nodalisation. In addition, the real structures and flow paths have been merged in order to reduce the model complexity. The four loops have been grouped. Therefore, there are two steam generator compartments R-SG12 and R-SG34 as well as the corresponding annular compartments behind the cylindrical shield R-ANN12 and R-ANN34, which are associated with the U-12 and U-34 as the safeguard compartments. There is a common sump zone R-SUMP within the safeguard building (U) U-SUMP. The reactor cavity R-CAVITY as well as the pipe duct room R-DUCT is represented by a single zone respectively. There is a connection from the containment to the safeguard building in order to consider the design leakage. Gas distributed in the two compartments of nuclear auxiliary building (AB) AB-UP1 & 2, can be vented by the exhaust chimney AB-CHIM to the surrounding environment ENVIRON.

COCOSYS analysis on THAI-AW3 experiment reveals the condensate coverage on the containment shell increases along the condensate flow streamwise on structures. Therefore, in order to investigate the condensate coverage distribution, the dome zone R-DOME is refined into ten layers (from bottom zone R-DOME01 to top zone R-DOME10), as shown in Fig. 5-2. These ten layers of dome are within the corresponding ten safeguard building zones (from bottom zone U-DOME01 to top zone U-DOME10). All zones are connected by using single atmospheric (gas) and drain (liquid) junctions. For simulating the water flow on the containment shell, the flow paths are defined in a specific way, such as the condensate flow from the upper structures to the lower structures in the neighboring zones.
In case of the overpressure in the component compartments, the rupture discs will open to enable atmospheric flow to the dome or the neighboring annular compartments. In order to reduce complexity, doors, rupture discs, and pressure relief flaps are merged and considered in a simple way by using rupture disc models (Kelm et al., 2014).

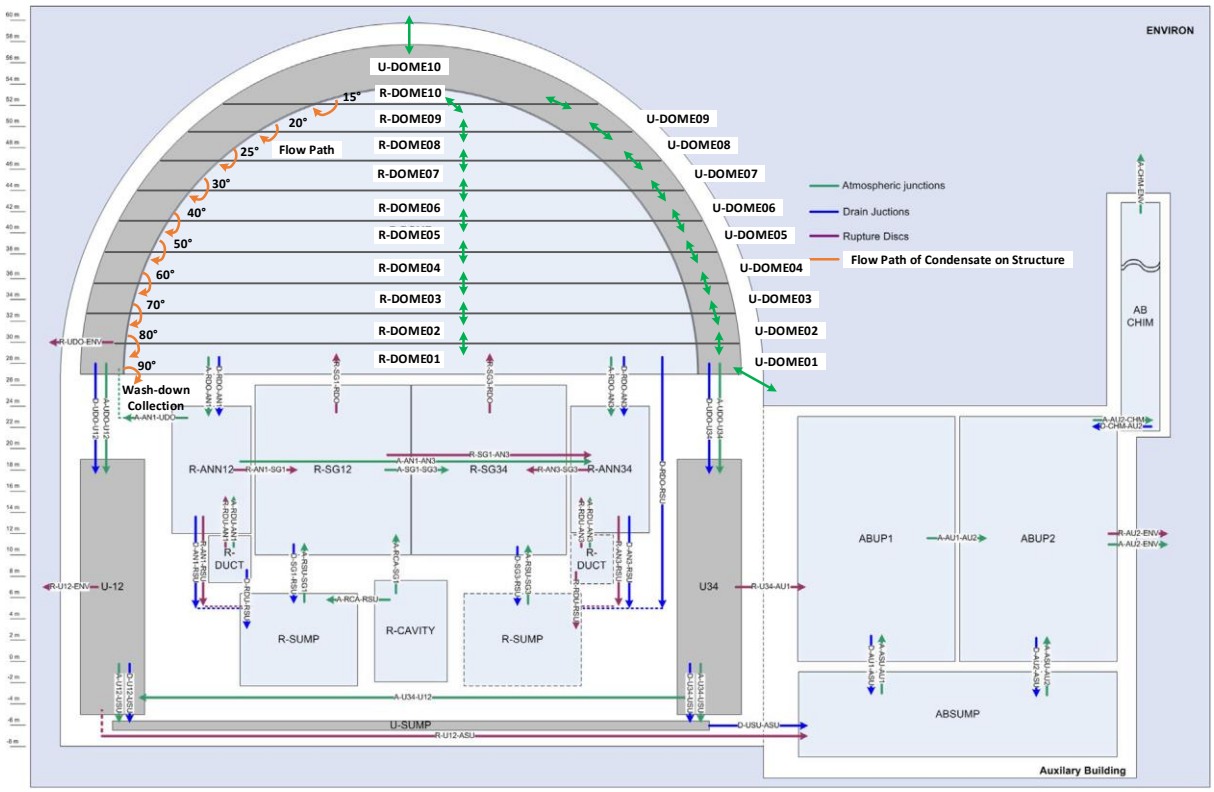

Fig. 5-2 ‘Generic Containment’ nodalisation refined on the basis of (Kelm et al., 2014)

The total heat capacity and the heat transfer area have been preserved. In order to have a common representation, especially of the total heat capacities, the properties of concrete and steel are defined (Kelm et al., 2014). Each zone below the dome contains vertical and horizontal both steel and concrete structures, which represent the overall heat exchange surface located in each zone. However, for the containment shell structures, the inclination angle increases step-by-step from top structure in zone R-DOME10 with 15° to bottom one in R-DOME01 with 90°. In order to keep consistent with the aerosol wash-down model, some heat structure parameters, such as the contact angle, characteristic length and height, condensation model, etc., have to be specified. Comparing with the benchmark Run-1, two additional atmosphere junctions are added to connect the zone U-DOME01 and U-DOME10 to the environment, so that the containment shell is specified as the containment long-term cooling system. All other structures are only considered as heat reservoirs. Both wall-gas-wall and wall-gas radiative heat exchanges (so called ‘WWR’ and ‘WGR’ in COCOSYS) are considered in the simulation. However, the view factors are default for the radiations, which are calculated automatically depending on the zone definition and the heat structure area.

5.1.3 Hypothetical accident scenario

A small break cross section of 50 cm^2 SB-LOCA with the loss of secondary heat

sink and all active safety injection systems are simulated by using the specified source term injections. The location of the pipe break is on the connecting line of the safety injection system, where the injection of one accumulator releases directly to the sump. The source terms representing the release from the primary circuit and later MCCI are defined in the sump zone and reactor cavity zone respectively. The releases of steam, liquid water, hydrogen during in-vessel phase and hydrogen, carbon monoxide and dioxide during ex-vessel phase are modelled by using the source terms in the form as pre-calculated tables. Energy source terms are also given and used to account for the fission product decay heat, heat losses (e.g. from the RPV), heat emission of the core melt, etc.

The events of the accident scenario are the same of the 'Generic Containment' benchmark Run-1, except the aerosol injection at 2040 sec. The simulated accident scenario is summarized in Table 5-1.

Table 5-1 Extended SB-LOCA accident scenario

Time, sec	Event
0	Break and blow-down happen
1800	Beginning of core heat-up and degradation
2040	Aerosol release
3000	Injection of hot leg accumulators
11200	Lower plenum core melt relocation
12280	RPV failure & melt relocation to the cavity
>12280	Molten Core-Concrete Interaction
46800	End of the simulated transient

At 1800 sec after the blow-down phase, the reactor core heat-up begins. Hydrogen and aerosol start to release in a subsequent few minutes due to the core degradation. At 3000 sec, the hot leg accumulators start water injection and lead to a reflooding of the damaged core. After vaporization of the water and pressure decrease in the primary circuit, the remaining water of the accumulators is injected at 8000 sec. With the core damage continuing, the core melt relocates to the lower plenum of the RPV at 11200 sec. At 12280 sec, the RPV fails and the core melt relocates to the reactor cavity. The SB-LOCA is extended to a full severe accident transient including H_2, CO and CO_2 release during ex-vessel phase.

The parameters required in aerosol wash-down model, such as the equilibrium contact angle, the effective particle density, and the erosion constant, etc., are

set as the same as in THAI-AW3 COCOSYS simulation. However, the aerosol surface load on each individual surface should not be initialized; instead, the aerosol injection has to be activated. The calculation of the aerosol surface density on walls is the contribution of the aerosol deposition model in COCOSYS.

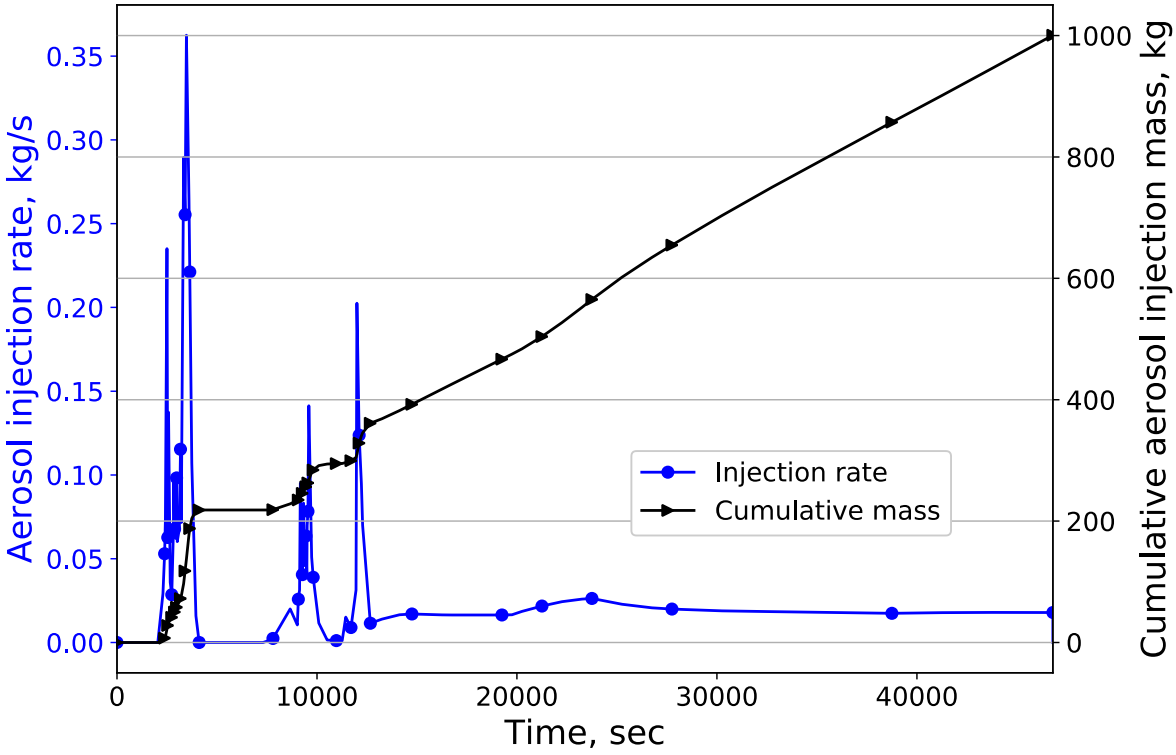

Fig. 5-3 Insoluble aerosol injection

The aerosol injects after the core degradation, which has a similar trend of hydrogen injection (Sangiorgi et al., 2015). The insoluble aerosol injection rate, kg/s, is valuated proportionally to the hydrogen injection rate with the total accumulated amount about 1000 kg insoluble aerosols of a German Konvoi containment (Weber, 2011), as shown in Fig. 5-3. During the in-vessel phase, about 345 kg of insoluble aerosols is released from core damage and relocation. Then during the ex-vessel phase, a continuous term is released from MCCI with a very stable aerosol injection rate. The cumulative aerosol injection mass increases quickly twice in the in-vessel phase due to the core degradation and core melt relocation respectively, and then increases linearly during the ex-vessel phase. The insoluble aerosol Ag is simulated currently, whose properties are the same as the Ag in THAI experiment simulation. The mass-median-diameter is about 1.1 μm with log-normal size distribution. The effective density is 1550 kg/m^3, the erosion constant $k_{e,0} = 0.03$ and the equilibrium contact angle is 14°.

Actually there are soluble aerosols injected during severe accidents, e.g. around 250 kg of German Konvoi containment (Weber, 2011). The soluble

aerosols, like CsI, are unneglectable from the perspective of the quantity of fission products. THAI-AW2 has been performed to investigate the wash-down behavior of soluble CsI and insoluble SnO_2 aerosol mixture. The experimental results concluded the wash-down efficiencies of the soluble and insoluble aerosols were independent from each other. The aerosol wash-down behavior was that the time range of aerosol wash-down was from minutes to hours and the completeness of aerosol wash-down was dependent on the water flow, the aerosol surface load, and the surface characteristics (Gupta et al., 2012). The soluble aerosols are quickly dissolved and transported with the condensate flow. The dissolution process can be simplified as an instantaneous (perhaps to be improved as time-dependent) and complete dissolution of wetted particles in COCOSYS. The wash-down of insoluble aerosols however remained far from being complete. The AULA model is developed for the wash-down of insoluble aerosols. In addition, the CONRAG is only coupled within the AULA so far. Therefore, the wash-down of soluble aerosols are not simulated in the current application.

In COCOSYS, the aerosol behavior is calculated separately in each zone by the model MAEROS, which can be combined with the MGA (Moving-Grid Method) condensation model considering the particle growth and shrinking rate. During the condensation interval, the thermal-hydraulic boundary conditions remain constant. They are only updated before the next interval. In the aerosol interval with MAEROS that follows, the ’wet’ aerosol is treated like a ’dry’ one. Agglomeration and deposition of the droplets are calculated as if they were solid particles (Klein-Heßling et al., 2015).

The decay heat of fission products is considered in a simple way by means of energy source terms in each zone. The combustion of burnable gas mixtures, PAR system, and containment spray system are not considered in the current run. The calculations are performed for a period of 46800 sec in order to investigate the containment thermal-hydraulics and aerosol wash-down process under a full severe accident transient.

5.2 **Thermal-hydraulic results**

Fig. 5-4 shows the containment pressure and temperature during the full severe accident scenario transient. The results predict three pressure peaks. The first two peaks are related to the blow-down and accumulator injections at those two moments. The quenching during core melt relocation to the RPV lower head causes the third pressure peak. The pressure evolution before RPV failure is comparable to the benchmark results, possibly due to the nodelization refinement and the modification of heat structure definition. After the RPV failure, although the fission product decay heat, steam and no-condensable gas are still released into the containment because of MCCI, the containment long-term

cooling system has already activated to cool the containment down, resulting the pressure less than the benchmark Run-1 (blue dashed line, no air from the environment flows through the gap of containment). The comparison generally proves that the implementation of the 'Generic Containment' is comparable to the one developed within SARNET2 activity and acceptable to continue the further studies. The average temperatures of gas in the dome and on the inner surface of the containment shell have similar trends of pressure, as also shown in Fig. 5-4. The important steam sinks are the condensation on walls and sumps in the beginning. From the green solid line in Fig. 5-4, it can be seen that there is a large amount of steam released in the containment during the blow-down phase. Therefore, the pressure (blue line) and temperatures (black lines) increase rapidly in the beginning. Comparing the steam mass flow rate in the containment, the trend observed is quite similar to the pressure, which shows the pressure level is corresponding to the steam mass flow.

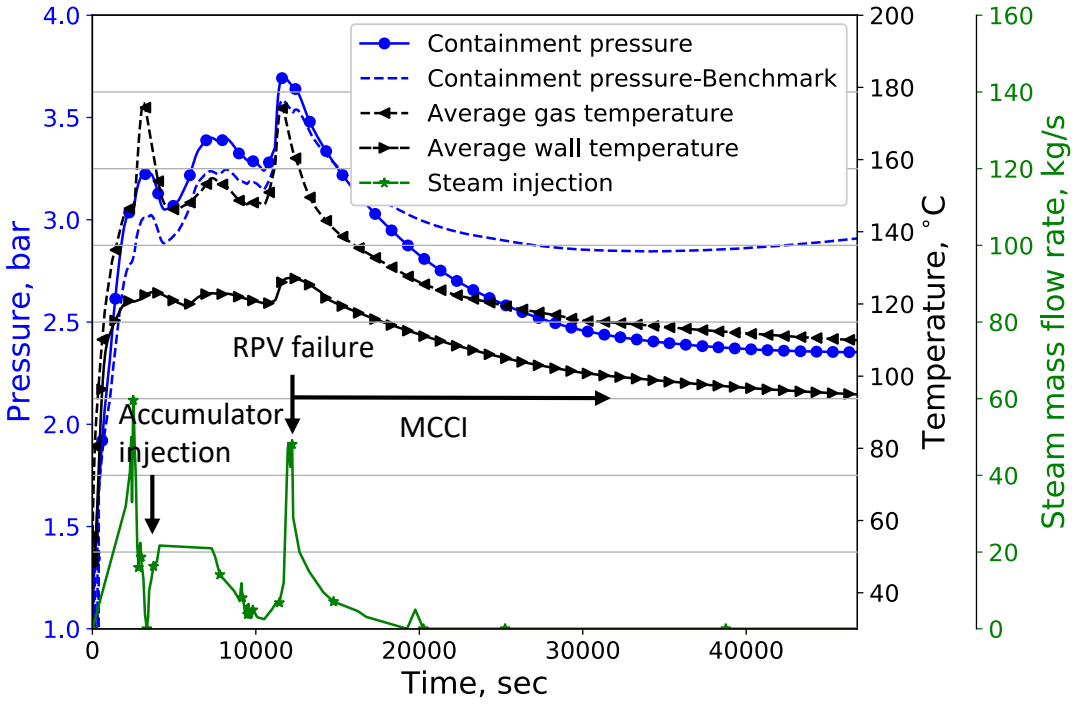

Fig. 5-4 Containment pressure and temperature evolutions

Fig. 5-5 shows the condensate mass flow rate per width on the containment shell. The structures over the elevation linking zones R-DOME01, 03, 05, 07 and 09 are taken as examples. During the blow-down phase, the condensate mass flow rate per width of each structure has a peak above 0.01 kg/(m·s), and then the value goes down to zero quickly since there is no steam release into containment at that moment. The mass flow rate per width recovers and gets several peaks later because of the steam injections again. After the RPV failure, the condensate mass flow rate per width increases gradually to a stable level. As discussed on the condensate of THAI-AW3 experiment before, the lower structure collects the condensate from the upper structures. Therefore, the

lowest structure linking zone R-DOME01 has the largest condensate mass flow rate.

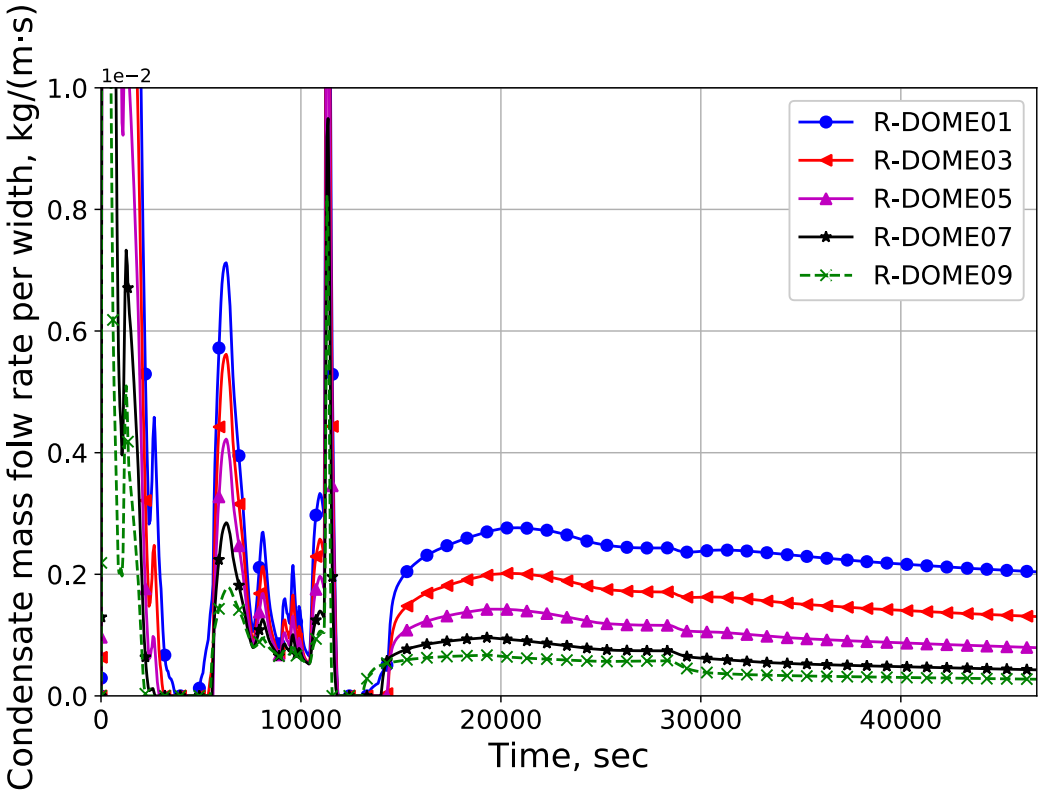

Fig. 5-5 Condensate mass flow rate per width on containment shell

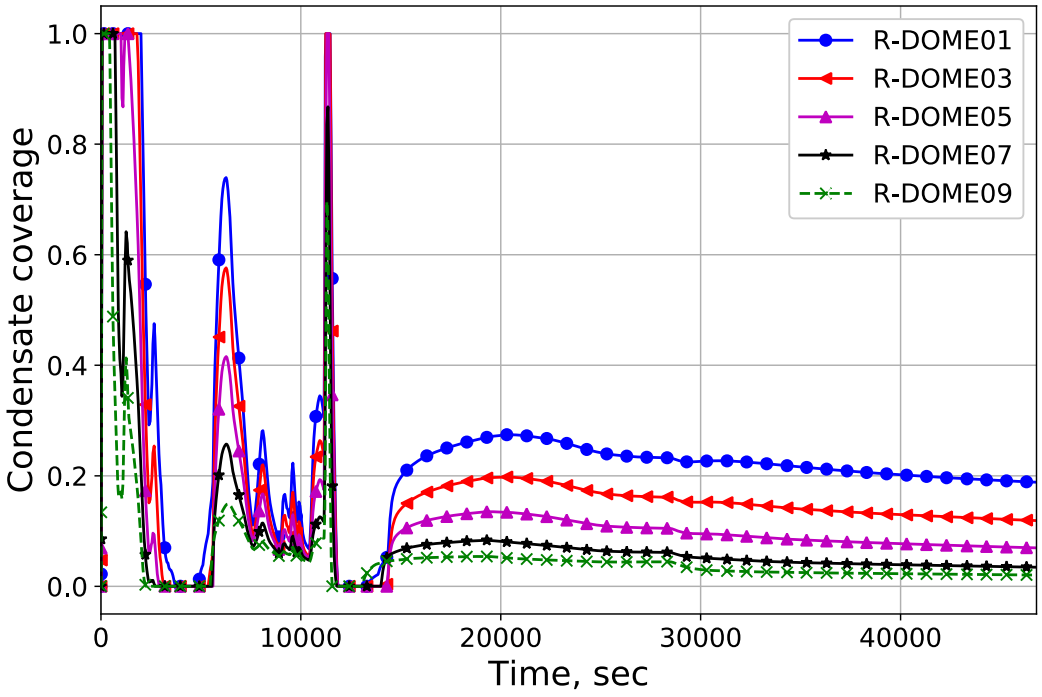

Fig. 5-6 Condensate coverage on the inner surface of containment shell

Consequently, in Fig. 5-6, the condensate coverage ε on the inner surface of the containment shell has an identical trend as the condensate mass flow rate per width. The results show condensate flow dominates the condensate coverage in the current run. Because the contact angles of the structures of containment shell are defined as the same, the Ka numbers of the condensate are similar since Ka is temperature dependent (see the temperature in Fig. 5-4), and the inclination angle does not change the coverage much once the angle larger than 30°. Therefore, according to the correlation of condensate coverage Eq. (4-3), Re number, in other words the condensate mass flow rate per width in current run, dominates the water coverage. Fig. 5-6 reveals additionally the coverage of most structures of the containment shell is not over 20% in the long-term phase. The surface is 100% covered by condensate if its mass flow rate per width is above 0.01 kg/(m·s).

5.3 Aerosol wash-down results

Fig. 5-7 presents the airborne aerosol concentration (only Ag here) in the containment atmosphere. There are three peaks of aerosol concentration in the containment atmosphere during its evolution, which are consistent exactly with the trend of aerosol injection, as seen in Fig. 5-3. During the ex-vessel phase, the concentration keeps stable as well as the aerosol injection rate stays constant. The aerosol injects in the zone R-SUMP, and then the aerosols are carried by the gas flows to the neighboring zones, e.g. the cavity, the pipe duct room, and two SG compartments. Some of the aerosols deposit on there, some of them are continuously taken by the gas flow to next surrounding rooms, and transported into the containment dome. During the ex-vessel phase, there are three aerosol concentration groups. The concentrations of sump and cavity are about 10^{-3}-10^{-4} kg/m^3. The concentration of the annular compartments under the dome is about 10^{-6} kg/m^3. The last group is the concentration in dome, SG and pipe duct compartments, in which the concentration is about below 10^{-6} kg/m^3. The aerosol concentration in dome is much less than in sump and cavity, since the dome is far away from the aerosol release location and the condensation effect on the containment shell enhances the deposition of the aerosol in the atmosphere.

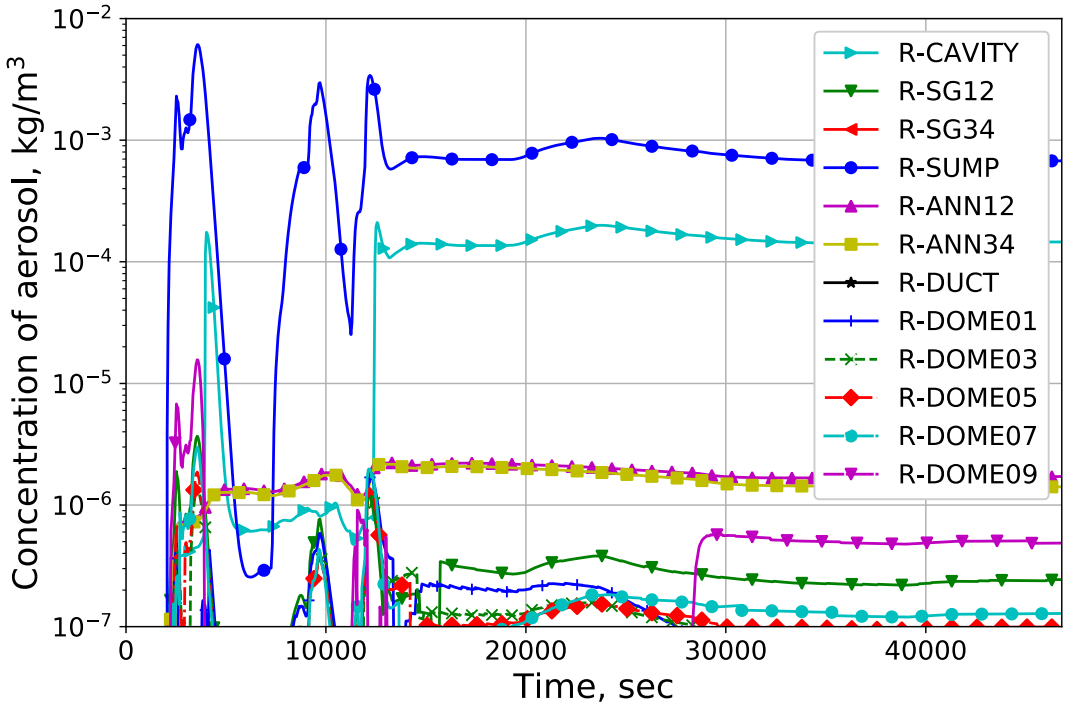

Fig. 5-7 Concentration evolution of airborne aerosol Ag inside containment

Fig. 5-8 reveals the aerosol wash-down rate (blue solid line) and the accumulated aerosol wash-down mass (black solid line) over the full severe accident transient. The aerosol wash-down activates after aerosol injection and the condensate covers the structure after the blow-down. The aerosol wash-down rate fluctuates until the accident goes into the ex-vessel phase, then it maintains at a low level about 0.003 kg/s. As a consequence, the cumulative aerosol wash-down mass increases fast before the RPV failure and then linearly in the later phase. There are about 173.65 kg aerosols on the containment shell washed down by the condensate flow. The black dashed line shows the quantity of the total deposited aerosol mass on the containment shell over time. The gap between aerosol mass deposited on the containment shell (black dashed line) and aerosol wash-down mass (black solid line) is moderate during the in-vessel phase, but becomes larger during the ex-vessel phase. The evolution of aerosol wash-down efficiency (the green solid line) goes up before the RPV failure, then goes down to nearly 30% at the end of the accident transient. That means it is close to 30% aerosols (mass) deposited on the containment shell are washed down to the condensate sump at the end. The trend of aerosol wash-down efficiency is strongly coupled with the condensate coverage. E.g. during the in-vessel phase, the efficiency increasing rapidly twice is corresponding with the two peaks of condensate coverage. The aerosol wash-down efficiency decreases during the ex-vessel phase since the average condensate coverage is less than before.

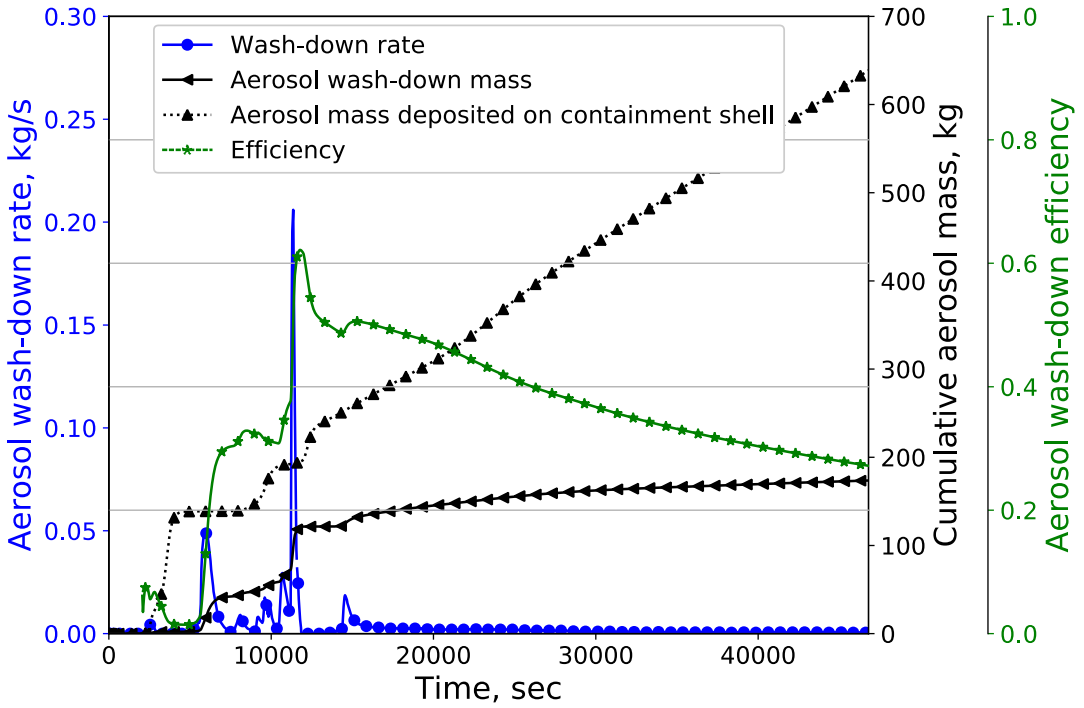

Fig. 5-8 Aerosol wash-down results

Fig. 5-9 presents the aerosol distribution inside containment over time. COCOSYS can offer the results of aerosol concentration, deposition, wash-down of each zone or structure. Here, the aerosol distributions are grouped into three parts: airborne aerosol mass (the aerosol in all zones atmosphere), aerosol mass remained on the containment shell, and others aerosol mass (mainly on structures and in sumps under the dome). Based on the aerosol concentration in zones are known, the evolution of the airborne aerosol mass suspending in the containment atmosphere over the whole accident scenario can be computed, which is about 4 kg at the end but has a peak value around 20 kg, as seen in the green line in Fig. 5-9. Compared to the total amount of aerosol injected into containment, 1000 kg, there is only 0.4% of aerosols suspending in the containment atmosphere. That is to say 99.6% of aerosols is deposited on walls and relocated in sumps due to the aerosol transport. The aerosol mass remained on the containment shell, as shown in the black solid line, equals the deposited mass on the containment shell minus the wash-down mass. The retention of aerosol on structures and in sumps under the containment dome including the aerosol wash-down mass, is about 531 kg at the end, as seen in the blue line. That means 53.1% of aerosols reserves under the containment dome, 46.5% remains on the containment shell inner surface, and 0.4% suspends in the containment atmosphere. The aerosol mass transported to the water sump via wash-down in comparison to the direct sedimentation of aerosols in the sump can be also approximated. E.g., at the end of the current case, the direct sedimentation of aerosols on the water sump is about 357.35 kg. Therefore, the ratio of the aerosol wash-down mass to the

direct sedimentation is about 0.486.

In a short, aerosol wash-down is one of the key factors to distribute the aerosols in nuclear containment. Actually, the aerosol distribution over time is dependent on the severe accident scenario. In the current run, the containment spray system is not designed for instance, since there is no spray system installed in this German PWR containment (but e.g. installed in other PWRs like French EPR). Experiments and simulations tell the water spray inside containment can remove the airborne aerosol in the atmosphere during severe accidents (Allelein, H. J., et al., 2009). The containment spray may reduce the aerosol amount deposited on the containment shell, which leads to the decrease of aerosol wash-down mass.

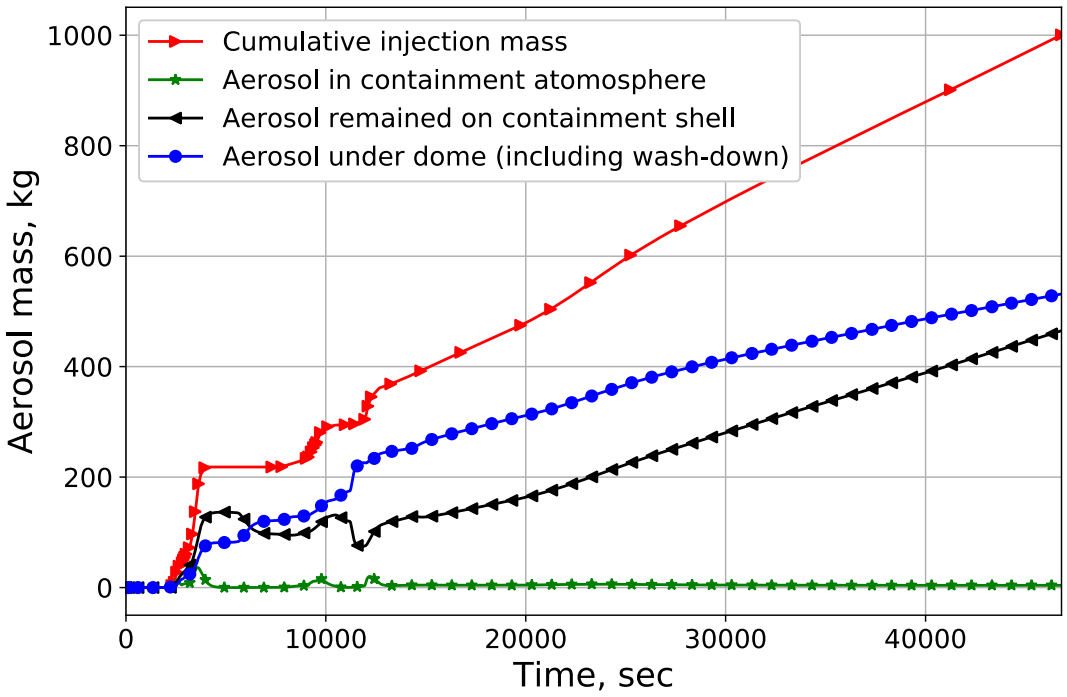

Fig. 5-9 Aerosol distribution over time

Fig. 5-10 presents the comparison of aerosol wash-down results calculated by the current modified COCOSYS and the previous COCOSYS version (without coupling CONRAG model). The condensate coverage ε in the previous COCOSYS is user-defined. Here the condensate coverage is set as 50% for each structure in the containment, which is taken as an example for the following discussion. In the calculation using previous COCOSYS, there are about 96.2 kg aerosols on the containment shell washed down by condensate flow, which is much less than the modified COCOSYS result of 173.65 kg. Not only for the ultimate results of aerosol wash-down but also for their evolutions, there are big gaps between these two calculations. The evolution of aerosol wash-down efficiency has similar comparison conclusions of aerosol wash-down mass.

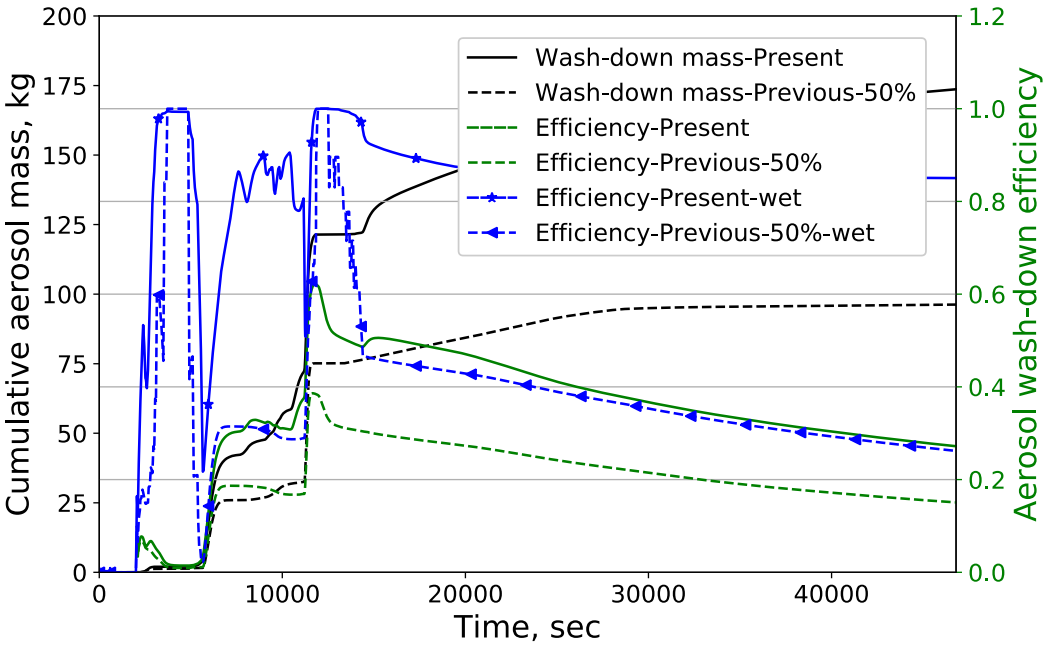

Fig. 5-10 Comparison of aerosol wash-down results

However, it is wondering that the higher condensate coverage 50% on the containment shell, compared with the calculation of the modified COCOSYS (see Fig. 5-6, less than 20% of most structures in most of the time), involves a lower aerosol wash-down efficiency. That is because it has to be considered if the condensate coverage is effective for the aerosol wash-down process. Two blue lines in Fig. 5-10 present the aerosol wash-down efficiencies on the wet parts of the surfaces (indicated with “wet” in legend of Fig. 5-10), which indicate a large deviation between them. It is one main objective of the CONRAG model shown in this containment analysis.

Fig. 5-11 shows the comparison of aerosol erosion rate of the structure in zone R-DOME01. The black dashed line of the coverage defined by 50%, has several higher periods of the erosion rate of aerosol wash-down during the in-vessel phase, since the coverage is more than 50% in the calculation of the modified COCOSYS, as shown in Fig. 5-6. The larger coverage leads to the smaller condensate velocity due to the mass conservation. With the similar reason, during the ex-vessel phase, the condensate volume flow rate drops a lot while the coverage keeps 50%, which leads to the condensate velocity is so smaller that its shear velocity is below the critical for aerosol wash-down. That results in the erosion rate during the ex-vessel phase is zero while it is positive in calculation of the modified COCOSYS (blue solid line). Therefore, it is hard to conclude a user-defined coverage is whether conservative or non-conservative. If the shear stress of condensate flow exceeds the critical, the smaller user-defined coverage deserves smaller wash-down mass.

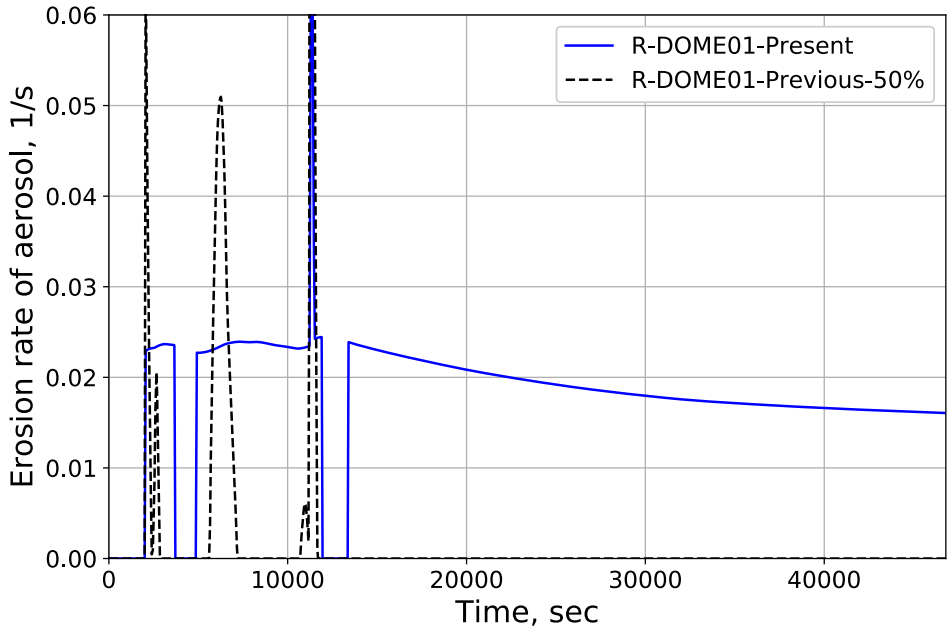

Fig. 5-11 Comparison of aerosol erosion rate

6 SUMMARY AND OUTLOOK

During severe accidents, fission products are generated due to core degradation and released into the containment with a large amount of steam. Aerosols are transferred on cold walls due to the steam condensation. The condensate flow washes down the aerosols from the walls and transports them into lower compartments or sumps. Therefore, the aerosol wash-down process affects the distribution of the fission products in the containment.

The condensate flow and its coverage are significant with respect to the aerosol wash-down efficiency. In the existing aerosol wash-down model AULA in the containment code COCOSYS, however, the condensate coverage is a user-defined value. In addition, an empirical correlation for the dimensionless critical shear stress of the resuspension of the aerosol particles is adopted in AULA. However, it is only valid for horizontal non-cohesive particle bed.

The overall goal of the current dissertation is the development of new models to describe the behavior of the condensate flow on the inclined surfaces in containment and the extension of the aerosol wash-down model with consideration of the wall inclination and the particle cohesion. The new models are validated by the experimental data and implemented in the program COCOSYS. The capacity of the modified COCOSYS code is evaluated by the simulation of the integral aerosol wash-down experiment THAI-AW3. Last but not least, the modified COCOSYS is applied to the 'Generic Containment' under the hypothetical severe accident scenario caused by SB-LOCA.

- **Conclusions**

A new modelling approach of describing the condensate flow and its coverage is proposed, which consists of a microscopic treatment and a macroscopic

treatment. Three condensate flow patterns are considered in the modelling approach, i.e. droplet, rivulet and film. The derived condensate coverage is in terms of the volume flow rate per width, contact angles, wall inclination and fluid properties. The developed condensate coverage model, as well as the proposed corresponding correlation, are validated with the existing experimental data. The comparison indicates that the prediction of rivulet coverage by the current model agrees well with the experimental data.

An expression of the equivalent Marangoni force is proposed, in order to consider its effect on the droplet velocity. The flow field inside the droplet and the dynamic contact angle are considered to evaluate the viscous force acting on the fast moving droplet. Moreover, a completely new criterion is proposed for the transition from droplet to rivulet, based on the assumption that when the surface tension force on the interface inside a droplet is less than the resultant force of gravitation, viscous force and surface tension force along the contact line, the droplet structure will stretch to rivulet.

The new experiment of water droplets moving on inclined surface coated with decontamination paint, DRISE, is performed with the Re number range 56< Re <1700. The model for the onset of the droplet motion predicts very well the DRISE data. At high Re number, the new developed models for the droplet velocity on the tilted surface and the criterion of the transition from droplet to rivulet are well validated with the data from the DRISE experiment and the experiment of Puthenveettil.

A correction factor considering the wall inclination and the aerosol cohesion is derived by the force balance analysis, in order to improve the prediction of the critical shear stress in AULA. The extended aerosol wash-down model with the effects of the inclination and the cohesion is validated by the THAI-AW3-LAB experiment. The comparison results show a significant improvement of the prediction accuracy and confirm the feasibility of the new model in the assessment of the erosion threshold.

The modified aerosol wash-down model AULA coupled with the condensate coverage model CONRAG is implemented in the containment code COCOSYS. The modified COCOSYS is validated against the integral THAI-AW3 experiment. The good prediction of the containment thermal-hydraulic parameters and the evolution of the condensate coverage indicates that the thermal-hydraulic models of COCOSYS are acceptable to analyze the aerosol wash-down process. The aerosols are washed down rapidly in the beginning, then slowly in the later phase. There are no significant differences in the aerosol wash-down efficiency between the calculation and the measurement.

The modified COCOSYS is further tested and applied to the ‘Generic Containment’ from the SARNET2 project. The original nodalisation is refined and modified, in order to be consistent with the aerosol wash-down model. The evolutions of thermal-hydraulic parameters and the aerosol distribution in the

‘Generic Containment’ during the pre-defined severe accident scenario are presented. The trend of the aerosol wash-down efficiency over the entire accident is strongly coupled with the condensate coverage. The comparison with the previous COCOSYS simulation reveals that the modification of COCOSYS, i.e. coupling with CONRAG, is necessary to investigate the aerosol wash-down process.

- **Outlook**

The present modelling approach does not consider the coalescence between droplets, droplets and rivulets, and rivulets. The coalescence between rivulets could not influence the wetting area much, so that it can be neglected but the droplets may reach the transition size fast if droplets merge with each other during their movement. In addition, if the size density distribution of moving droplets is known, the coalescence problem can be solved.

Condensate flow models influence on the heat transfer, e.g. the effect of condensate coverage on heat transfer coefficient. It is notable that the condensate coverage is in terms of condensate flow rate and temperature, which should be coupled within the conservation equations and can be solved by iteration. Furthermore, the current condensation and evaporation rivulet models are developed separately. The methodology of the harmonization and switch between these two models is of interest for some conditions, e.g. re-evaporation after condensation.

Bibliography

Allelein, H. J., Auvinen, A., Ball, J., Guntay, L., Herranz, L., Hidaka, A., Weber, G. (2009). State-of-the-art report on nuclear aerosols in reactor safety. OECD Technical Report, NEA/CSNI/R5, 5.

Allen, R.F. and Benson, P.R., 1975. Rolling drops on an inclined plane. Journal of Colloid and Interface Science, 50(2), pp. 250-253.

Amend, K. and Klein, M., 2017. Modeling and simulation of water flow on containment walls with inhomogeneous contact angle distribution. Atw. Internationale Zeitschrift für Kernenergie, 62(7), pp. 477-481.

Amend, K. and Klein, M., 2018. Development and validation of a CFD wash-off model for fission products on containment walls. Atw. Internationale Zeitschrift für Kernenergie, 63(8-9), pp. 469-473.

Ariathurai, R., MacArthur, R. C., & Krone, R. B. ,1977. Mathematical Model of Estuarial Sediment Transport. Final Report. University of California, Davis Department of Civil Engineering.

Arndt, S., Weber, G., 1998. FIPHOST - A Module to Calculate the Fission Product Transport in a LWR Containment. Gesellschaft für Anlagen- und Reaktorsicherheit (GRS), Germany.

Ausner, I., 2007. Experimentelle Untersuchungen mehrphasiger Filmströmungen. PhD Thesis. Technical Univesity Berlin.

Blake, T.D., 2006. The physics of moving wetting lines. Journal of colloid and interface science, 299(1), pp.1-13.

Bönigke, G., Ewig, F., Friedrichs, H.G., Heitsch, M., Huettermann, B., Jendrich, U., Meier, S., Scharfe, A., Sonnenkalb, M., Rohde, J., Tiltmann, M., 1998. Untersuchung von Maßnahmen des anlageninternen Notfall-schutzes zur Schadensbegrenzung in LWR, Report GRS-A-2601, Gesellschaft für Anlagen- und Reaktorsicherheit (GRS), Germany.

Bridgman, P. W. 1931. Dimensional Analysis (2nd edition), New Haven, CT: Yale University Press.

Brown, R.A., Orr Jr, F.M. and Scriven, L.E., 1980. Static drop on an inclined plate: analysis by the finite element method. Journal of Colloid and Interface Science, 73(1), pp. 76-87.

Buckingham, E., 1914. On physically similar systems; illustrations of the use of dimensional equations. Physical review, 4(4), pp. 345.

Chatelard P. and Reinke N., 2009. Overview of the integral code ASTEC V2. 0. Rev. 0., IRSN/GRS.

Chin, Y.S., Mathew, P.M., Glowa, G., Dickson, R., Liang, Z., Leitch, B., Barber, D., Vasic, A., Bentaib, A., Journeau, C., Malet, J., 2014. Containment Code Validation Matrix. OECD Technical Report, NEA/CSNI/R (2014) 3.

Cox, R.G., 1986. The dynamics of the spreading of liquids on a solid surface. Part 2. Surfactants. Journal of Fluid mechanics, 168, pp. 195-220.

Cox, R.G., 1998. Inertial and viscous effects on dynamic contact angles. Journal of Fluid Mechanics, 357, pp. 249-278.

De Gennes, P.G., 1985. Wetting: statics and dynamics. Reviews of modern physics, 57(3), pp. 827.

Dey, S. and Papanicolaou, A., 2008. Sediment threshold under stream flow: A state-of-the-art review. KSCE Journal of Civil Engineering, 12(1), pp. 45-60.

Doniec, A., 1988. Flow of a laminar liquid film down a vertical surface. Chemical engineering science, 43(4), pp. 847-854.

Doniec, A., 1991. Laminar flow of a liquid rivulet down a vertical solid surface. The Canadian Journal of Chemical Engineering, 69(1), pp. 198-202.

Dupont, J., 2017. Thin liquid film dynamics in a condensing and re-evaporating environment. PhD Thesis. Swiss Federal Institute of Technology in Zurich (ETH Zürich).

Dussan V., E.B., 1976. The moving contact line: The slip boundary condition. Journal of Fluid Mechanics, 77, pp. 665–684.

Dussan, E.B. V, 1985. On the ability of drops or bubbles to stick to non-horizontal surfaces of solids. Part 2. Small drops or bubbles having contact angles of arbitrary size. Journal of Fluid Mechanics, 151, pp. 1–20.

El-Genk, M.S., Saber, H.H., 2001. Minimum thickness of a flowing down liquid film on a vertical surface. International Journal of Heat and Mass Transfer, Vol. 44, pp. 2809–2825.

ElSherbini, A.I., Jacobi, A.M., 2006. Retention forces and contact angles for critical liquid drops on non-horizontal surfaces. Journal of colloid and interface science, 299, pp. 841–849.

Extrand, C.W. and Kumagai, Y., 1995. Liquid drops on an inclined plane: the relation between contact angles, drop shape, and retentive force. Journal of colloid and interface science, 170(2), pp. 515-521.

Freitag, M., Schmidt, E., Gupta,S., Laufenberg, B. von, Colombet, M., Kühnel, A., 2016, Wash-Down Behavior of Silver Aerosols Test AW-3 (Part 1).

Report No. 1501455-TR-AW-3 (Part 1), Becker Technologies, Frankfurt, Germany.

Freitag, M., Gupta, S., Beck, S., Sonnenkalb, M., 2018. Experimental and Analytical Investigations of Aerosol Processes: Wash-Out and Wash-Down. Nuclear Science Engineering, 193, pp. 198–210.

Furmidge, C.G.L., 1962. Studies at phase interfaces. I. The sliding of liquid drops on solid surfaces and a theory for spray retention. Journal of colloid science, 17(4), pp. 309-324.

Gallaire, F., Meliga, P., Laure, P., Baroud, C.N., 2014. Marangoni induced force on a drop in a Hele Shaw cell. Physics of Fluids, 26(6), pp. 062105.

Gauntt, R.O., Cash, J.E., Cole, R.K., Erickson, C.M., Humphries, L.L., Rodríguez, S.B. and Young, M.F., 2005. MELCOR Computer Code Manuals, Version 1.8. 6, Vol 1: Primer and Users' Guide. NUREG/CR-6119, Sandia National Laboratories, Albuquerque, NM, United States.

Gelbard, F., 1982. MAEROS user manual. [LMFBR] (No. NUREG/CR-1391; SAND-80-0822). Sandia National Laboratories, Albuquerque, NM, United States.

Guo, J., 2002. Hunter Rouse and Shields Diagram. In Advances in hydraulics and water engineering: Volumes I & II, pp. 1096-1098.

Gupta, S., Langer. G, 2009. Aerosol Wash-down Test (AW), OECD-NEA THAI Project, Report No. 1501326–AW-QLR, Becker Technologies, Frankfurt, Germany.

Gupta, S., Balewski, B., et al, 2012. Wash-down Behaviour of Soluble and Non-soluble Aerosols Test ID: AW-2. Report No. 1501361–TR-AW-2, Becker Technologies, Frankfurt, Germany.

Gupta, S., Funke, F., Langrock, G., Weber, G., von Laufenberg, B., Schmidt, E., Freitag, M. and Poss, G., 2015. THAI Experiments on Volatility, Distribution and Transport Behaviour of Iodine and Fission Products in the Containment. In Proceedings of the International OECD-NEA/NUGENIA-SARNET Workshop on the Progress in Iodine Behaviour for NPP Accident Analysis and Management, Marseille, France, pp. 1-4.

Hanniet-Girault, N. and Repetto, G., 1999. FPT-0 final report. In IP/99/423, IRSN, Saint Paul-lez-Durance, France.

Hartley, D.E. and Murgatroyd, W., 1964. Criteria for the break-up of thin liquid layers flowing isothermally over solid surfaces. International Journal of Heat and Mass Transfer, 7(9), pp.1003-1015.

Herranz, L.E., Anderson, M.H. and Corradini, M.L., 1998. A diffusion layer model for steam condensation within the AP600 containment. Nuclear Engineering and Design, 183(1-2), pp. 133-150.

Hillebrand, G., 2008. Transportverhalten kohäsiver Sedimente in turbulenten Strömungen: Untersuchungen im offenen Kreisgerinne. PhD Thesis, Universität Fridericiana zu Karlsruhe (TH).

Hobler, T., 1964. Minimum surface wetting (in Polish). Chemia Stosowana. B, 2, pp. 145-159.

Hoehne, M., Weber, G., 2010. Interpretation of the OECD THAI CsI Aerosol Wash-down Test AW by COCOSYS analyses. OECD THAI project final seminar, Paris, France.

Huang, X., Cheng, X., 2015. Modification and application of water film model in COCOSYS for PWR's passive containment cooling. Nuclear Engineering and Design, 280, pp. 251–261.

IAEA, 2006. IAEA Safety glossary, terminology used in nuclear, radiation, radioactive waste and transport safety, version 2.0, IAEA, Vienna, Austria.

Jacquemain, D., Bourdon, S., de Braemaeker, A., and M. Barrachin, 2000. Final report FPT-1. IRSN, Saint-Paul-lez-Durance, France.

Jiang, Z. and Yan, W., 1996. Experimental Studies on Surface Wave Characteristics of Free-Falling Liquid Films.Heat Transfer Science and Technology, Proceedings of the 4th International Symposium on Heat Transfer, Edited by Wang B., Higher Education Press, Beijing, pp. 200-205.

Karapantsios, T. D., Paras, S. V., Karabelas, A. J., 1989. Statistical characteristics of free falling films at high Reynolds numbers. International journal of multiphase flow, 15(1), pp. 1-21.

Kelm, S., Broxtermann, P., Krajewski, S., Allelein, H.-J., Preusser, G., Sangiorgi, M.,et al., 2014. Generic Containment a detailed comparison of containment simulations performed on plant scale. Annals of nuclear energy, 74, pp. 165–172.

Kim, H.Y., Lee, H.J., Kang, B.H., 2002. Sliding of liquid drops down an inclined solid surface. Journal of colloid science, 247, pp. 372–380.

Klein-Heßling, W., Arndt, S., Weber, G., Nowack, H., Spengler, C., Schwarz, S., Pelzer, M., Eckel, J., 2015. COCOSYS v2.4 User's Manual. Gesellschaft für Anlagen- und Reaktorsicherheit (GRS), Germany.

Laufenberg, B. Von, Colombet, M., Freitag, M., 2014 a. Wash-down Tests of Silver Aerosol from Stainless Steel and Painted Surfaces. 10th International Topical Meeting on Nuclear Reactor Thermal-Hydraulics (NUTHOS-10), Okinawa, Japan, pp. 14-18.

Laufenberg, B. Von, Colombet, M., Freitag, M., 2014 b. Wash-Down of Insoluble Aerosols: Results of the Laboratory Tests Related to THAI AW-3 Test. Report No. 1501455-TR-AW-3-LAB, Becker Technologies, Frankfurt, Germany.

Le Grand, N., Daerr, A. and Limat, L., 2005. Shape and motion of drops sliding down an inclined plane. Journal of Fluid Mechanics, 541, pp. 293-315.

Mannetje, D., Ghosh, S., Lagraauw, R., Otten, S., Pit, A., Berendsen, C., Zeegers, J., van den Ende, D. and Mugele, F., 2014. Trapping of drops by wetting defects. Nature communications, 5(1), pp. 1-7.

Meric, R.A., and Erbil, H.Y., 1998. Evaporation of Sessile Drops on Solid Surfaces: Pseudospherical Cap Geometry. Langmuir, 14, pp. 1915–1920.

Moran K, Inumaru J, Kawaji M., 2002. Instantaneous hydrodynamics of a laminar wavy liquid film. International Journal of Multiphase Flow, 28(5), pp. 731-755.

Nusselt, W., 1916. Die Oberflächenkondensation des Wasserdampfes, VDI-Zeitschriften. 60 (27), pp. 541–546

Owczarski, P.C. and Burk, K.W., 1991. SPARC-90: A code for calculating fission product capture in suppression pools. No. NUREG/CR-5765; PNL-7723. Nuclear Regulatory Commission, Washington, DC, United States. Division of Regulatory Applications, Pacific Northwest Laboratory, Richland, WA, United States.

Phadnis, A., Rykaczewski, K., 2017. The effect of Marangoni convection on heat transfer during dropwise condensation on hydrophobic and omniphobic surfaces. International Journal of Heat and Mass Transfer, 115, pp. 148–158.

Podgorski, T., Flesselles, J.M., Limat, L., Kim, H.Y., Lee, H.J., Kang, B.H., 2001. Sliding of liquid drops down an inclined solid surface. Journal of colloid science, 247, pp. 372–380.

Povilaitis, M., Kelm, S. and Urbonavičius, E., 2017. The Generic Containment SB-LOCA accident simulation: Comparison of the parameter uncertainties and user-effect. Annals of Nuclear Energy, 106, pp. 1-10.

Puthenveettil, B.A., Senthilkumar, V.K., Hopfinger, E.J., 2013. Motion of drops on inclined surfaces in the inertial regime. Journal of Fluid Mechanics, 726, pp. 26–61.

Sakai, M., Song, J.H., Yoshida, N., Suzuki, S., Kameshima, Y. and Nakajima, A., 2006. Direct observation of internal fluidity in a water droplet during sliding on hydrophobic surfaces. Langmuir, 22(11), pp. 4906-4909.

Sangiorgi, M., Grah, A. and Ammirabile, L., 2015. Circuit and Containment Aspects of PHÉBUS Experiment FPT-2. JRC Technical Reports, Publications Office of the European Union.

Shields, A., 1936. Anwendung der Aehnlichkeitsmechanik und der Turbulenzforschung auf die Geschiebebewegung. PhD Thesis, Technical University Berlin.

Sikarwar, B.S., Muralidhar, K. and Khandekar, S., 2010. Flow and Heat Transfer in a Pendant Liquid Drop Sliding on an Inclined Plane. 9th International ISHMT–ASME Heat and Mass Transfer Conference, Mumbai, India. pp. 1322-1329.

Song, F., 2008. Water droplet movements on methyl-terminated organosilane modified silicon wafer surfaces, PhD Thesis, University of Akron.

Suzuki, S., Nakajima, A., Sakai, M., Sakurada, Y., Yoshida, N., Hashimoto, A., Kameshima, Y. and Okada, K., 2008. Slipping and rolling ratio of sliding acceleration for a water droplet sliding on fluoroalkylsilane coatings of different roughness. Chemistry letters, 37(1), pp. 58-59.

Takahama, H., Kato, S., 1980. Longitudinal flow characteristics of vertically falling liquid films without concurrent gas flow. International Journal of Multiphase Flow, 1980, 6(3), pp. 203-215.

Ternat, F., Boyer, P., Anselmet, F. and Amielh, M., 2008. Erosion threshold of saturated natural cohesive sediments: Modeling and experiments. Water resources research, 44(11), https://doi.org/10.1029/2007WR006537.

Thampi, S.P., Adhikari, R. and Govindarajan, R., 2013. Do liquid drops roll or slide on inclined surfaces?. Langmuir, 29(10), pp. 3339-3346.

Van Dorsselaere J P, Seropian C, Chatelard P, et al. The ASTEC integral code for severe accident simulation. Nuclear Technology, 2009, 165(3), pp. 293-307.

Varagnolo, S., Ferraro, D., Fantinel, P., Pierno, M., Mistura, G., Amati, G., Biferale, L. and Sbragaglia, M., 2013. Stick-slip sliding of water drops on chemically heterogeneous surfaces. Physical review letters, 111(6), pp. 066101.

Voinov, O.V., 1976. Hydrodynamics of wetting. Fluid dynamics, 11(5), pp. 714-721.

Von der Hardt, P. and Tattegrain, A., 1992. The Phebus fission product project. Journal of nuclear materials, 188, pp.115-130.

Wadgaonkar, I.P., Sundararajan, T. and Das, S.K., 2015. Criterion for sliding/rolling characterization during droplet motion over superhydrophobic surfaces. arXiv preprint arXiv:1511.08563.

Weber, G., 2011. Ein neues Abwaschmodell für unlösliche Aerosole (AULA), GRS-TN-WEG-01/2011. Gesellschaft für Anlagen- und Reaktorsicherheit (GRS), Germany.

Weber, G., Funke, F., Gupta, S., 2015. Iodine and Silver Wash-Down Modelling in Cocosys-Aim By Use of Thai Results. OECD-NEA/NUGENIA-SARNET Workshop on the Progress in Iodine Behaviour for NPP Accident Analysis and Management, Marseille, France, pp. 2-1

Wenzel, R.N., 1936. Resistance of solid surfaces to wetting by water. Industrial & Engineering Chemistry, 28(8), pp. 988-994.

Williams, K.M.D., Tills, J., Griffith, R.O., Gido, R.G., Tadios, E.L., Davis, F.J., Martinez, G.M. and Washington, K.E., 1997. Code manual for CONTAIN 2.0: a computer code for nuclear reactor containment analysis. Sandia National Laboratories, NUREG/CR-6533, SAND97-1735, Albuquerque, NM, United States.

Won, B.J., Lee, W., Song, S., 2017. Estimation of the thermocapillary force and its applications to precise droplet control on a microfluidic chip. Scientific Report, 7 (1), pp. 3062.

Yu, Y.Q., Wei, S.J., Yang, Y.H., Cheng, X., 2012. Experimental study of water film falling and spreading on a large vertical plate. Progress Nuclear Energy, 54, pp. 22–28.

Yu, Y. Q., Cheng, X., 2014. Three-dimensional simulation on behavior of water film flow with and without shear stress on water–air interface. International Journal of Heat and Mass Transfer, 79, pp. 561-572.

Yu, Y., 2012. Experimental and Numerical Study on Film Flow Behavior on Large Scale Flat Plate, PhD thesis, Shanghai Jiao Tong University.